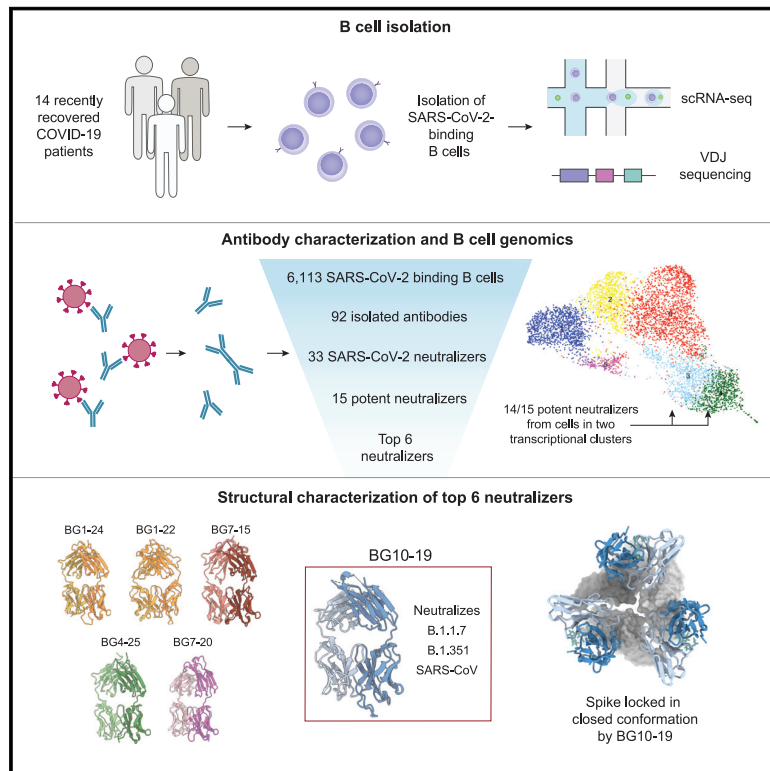Since January 2020 Elsevier has created a COVID-19 resource centre with free information in English and Mandarin on the novel coronavirus COVID-19. The COVID-19 resource centre is hosted on Elsevier Connect, the company's public news and information website.

B cell genomics behind cross-neutralization of SARS-CoV-2 variants and SARS-CoV

Graphical abstract

Highlights

- SARS-CoV-2-specific B cell repertoire includes transcriptionally distinct B cells

- 14 out of 15 potent neutralizers are from two clusters, memory and activated B cells

- BG10-19 locks the spike trimer in a closed conformation to potently neutralize SARS-CoV-2

- Several potent antibodies, including BG10-19, neutralize SARS-CoV-2 variants of concern

Authors

Johannes F. Scheid,
Christopher O. Barnes, Basak Eraslan, ...,
Deborah Hung, Pamela J. Bjorkman,
Ramnik J. Xavier

Correspondence

bjorkman@caltech.edu (P.J.B.),
xavier@molbio.mgh.harvard.edu (R.J.X.)

In brief

B cell genomics reveals transcriptionally distinct populations that modulate antibody responses to SARS-CoV-2, with the identification of a monoclonal antibody that locks the virus spike trimer to neutralize recent variants, SARS and heterologous RBDs.

Cell

CellPress

Article

B cell genomics behind cross-neutralization of SARS-CoV-2 variants and SARS-CoV

Johannes F. Scheid,[1,2,3,12] Christopher O. Barnes,[4,12] Basak Eraslan,[1,12] Andrew Hudak,[1] Jennifer R. Keeffe,[4] Lisa A. Cosimi,[5] Eric M. Brown,[1,3] Frauke Muecksch,[6] Yiska Weisblum,[6] Shuting Zhang,[1] Toni Delorey,[1,7] Ann E. Woolley,[5] Fadi Ghantous,[8] Sung-Moo Park,[1] Devan Phillips,[1,7] Betsabeh Tusi,[1] Kathryn E. Huey-Tubman,[4] Alexander A. Cohen,[4] Priyanthi N.P. Gnanapragasam,[4] Kara Rzasa,[1] Theodora Hatziioanno,[6] Michael A. Durney,[1] Xiebin Gu,[1] Takuya Tada,[9] Nathaniel R. Landau,[9] Anthony P. West, Jr.,[4] Orit Rozenblatt-Rosen,[1,7,13] Michael S. Seaman,[8] Lindsey R. Baden,[5] Daniel B. Graham,[1,3] Jacques Deguine,[1] Paul D. Bieniasz,[6,10] Aviv Regev,[7,10,13] Deborah Hung,[1,3,11] Pamela J. Bjorkman,[4,*] and Ramnik J. Xavier[1,2,3,7,11,14,*]

[1]Broad Institute of the Massachusetts Institute of Technology and Harvard University, Cambridge, MA 02142, USA
[2]Division of Gastroenterology, Massachusetts General Hospital and Harvard Medical School, Boston, MA 02114, USA
[3]Center for Computational and Integrative Biology, Massachusetts General Hospital and Harvard Medical School, Boston, MA 02114, USA
[4]Division of Biology and Biological Engineering, California Institute of Technology, Pasadena, CA 91125, USA
[5]Division of Infectious Diseases, Brigham and Women's Hospital, Harvard Medical School, Boston, MA 02115, USA
[6]Laboratory of Molecular Virology, The Rockefeller University, New York, NY 10065, USA
[7]Klarman Cell Observatory, Broad Institute of MIT and Harvard, Cambridge, MA 02142, USA
[8]Center for Virology and Vaccine Research, Beth Israel Deaconess Medical Center, Harvard Medical School, Boston, MA, 02215, USA
[9]Department of Microbiology, NYU Grossman School of Medicine, New York, NY 10016, USA
[10]Howard Hughes Medical Institute, Chevy Chase, MD, USA
[11]Department of Molecular Biology, Massachusetts General Hospital and Harvard Medical School, Boston, MA 02114, USA
[12]These authors contributed equally
[13]Present address: Genentech, 1 DNA Way, South San Francisco, CA 94080, USA
[14]Lead contact
*Correspondence: bjorkman@caltech.edu (P.J.B.), xavier@molbio.mgh.harvard.edu (R.J.X.)
https://doi.org/10.1016/j.cell.2021.04.032

SUMMARY

Monoclonal antibodies (mAbs) are a focus in vaccine and therapeutic design to counteract severe acute respiratory syndrome coronavirus 2 (SARS-CoV-2) and its variants. Here, we combined B cell sorting with single-cell VDJ and RNA sequencing (RNA-seq) and mAb structures to characterize B cell responses against SARS-CoV-2. We show that the SARS-CoV-2-specific B cell repertoire consists of transcriptionally distinct B cell populations with cells producing potently neutralizing antibodies (nAbs) localized in two clusters that resemble memory and activated B cells. Cryo-electron microscopy structures of selected nAbs from these two clusters complexed with SARS-CoV-2 spike trimers show recognition of various receptor-binding domain (RBD) epitopes. One of these mAbs, BG10-19, locks the spike trimer in a closed conformation to potently neutralize SARS-CoV-2, the recently arising mutants B.1.1.7 and B.1.351, and SARS-CoV and cross-reacts with heterologous RBDs. Together, our results characterize transcriptional differences among SARS-CoV-2-specific B cells and uncover cross-neutralizing Ab targets that will inform immunogen and therapeutic design against coronaviruses.

INTRODUCTION

Severe acute respiratory syndrome coronavirus 2 (SARS-CoV-2) is the third zoonotic betacoronavirus to cause a human outbreak after SARS-CoV and Middle East respiratory syndrome coronavirus (MERS-CoV) (de Wit et al., 2016). After the SARS-CoV and MERS-CoV outbreaks, limited numbers of neutralizing monoclonal antibodies (mAbs) were isolated using phage display library techniques (Prabakaran et al., 2006; Sui et al., 2004) and Epstein-Barr virus transformed B cells (Corti et al., 2015; Traggiai et al., 2004). Since then, high-throughput single-cell RNA

sequencing (scRNA-seq) of B cells has allowed simultaneous characterization of their clonal landscape and associated transcriptional profiles (Neu et al., 2019). When combined with functional testing and structural characterization of selected mAbs, this integrated approach should allow us to learn more about transcriptional pathways involved in the generation of efficient antiviral antibody (Ab) responses and the roles of different B cell subpopulations (Horns et al., 2020; Mathew et al., 2020; Neu et al., 2019; Waickman et al., 2020; Sokal et al., 2021).

Recent efforts to develop therapeutic mAbs against SARS-CoV-2 were aided by structures that have revealed how the

SARS-CoV-2 spike binds to its angiotensin-converting enzyme 2 (ACE2) receptor (Yan et al., 2020), specificities of polyclonal Ab responses in coronavirus disease 2019 (COVID-19) convalescent individuals (Barnes et al., 2020b), and commonalities among receptor-binding domain (RBD)-binding mAbs (Barnes et al., 2020a; Tortorici., 2020; Yuan et al., 2020). Collectively, these structures guide choices of mAb pairs for treatment cocktails, while informing structure-based engineering experiments to improve mAb potencies and/or resistance to viral mutations. Furthermore, recent mapping of neutralizing SARS-CoV-2 mAbs that target conserved spike epitopes (Lv et al., 2020; Piccoli et al., 2020) has the potential to guide structure-based immunogen design to elicit cross-reactive mAbs against zoonotic coronaviruses with spillover potential.

Here, we use scRNA-seq to investigate SARS-CoV-2 spike-specific B cell responses in 14 subjects who had recovered from COVID-19. We matched the VDJ sequence and transcriptional profiles with functional studies from 92 mAbs and identified two transcriptional clusters (TCs) from which the majority of neutralizing Abs (nAbs) were isolated. We structurally characterized six of the most potently nAbs derived from B cells in these two TCs, including BG10-19 that reaches between adjacent RBDs on a single spike trimer, locking it in a conformation that cannot bind ACE2 in a manner distinct from previously described mAbs (Barnes et al., 2020a; Tortorici et al, 2020). BG10-19 potently neutralized SARS-CoV-2, the United Kingdom (UK) variant B.1.1.7 (Davies et al., 2021), and the South African variant B.1.351 (Tegally et al., 2020) as well as the heterologous SARS-CoV pseudotyped viruses. Furthermore, characterization of mAbs belonging to the *VH3-53/VH3-66*-encoded class (Barnes et al., 2020b; Wu et al., 2020a; Yuan et al., 2020) showed common binding modes for mAbs with short (<14 amino acids) and long (>15 amino acids) heavy chain complementarity-determining region 3 (CDRH3) loops, providing new insights into this recurring class of SARS-CoV-2 nAbs.

RESULTS

A cohort of recently recovered COVID-19 patients shows serum-neutralizing activity

To understand the development of B cell responses after SARS-CoV-2 infection, we enrolled 14 subjects who had recently recovered from COVID-19. Subjects were diagnosed in March 2020, none required hospitalization, and the time between diagnosis and enrollment ranged between 31 and 61 days (Table S1). 12 of 14 subjects were diagnosed with COVID-19 using PCR-based testing. The remaining two subjects were diagnosed based on serum reactivity to RBD in ELISA, clinical symptoms, and history of recent exposure (Table S1).

To evaluate serum neutralizing activity, we used a pseudotyped virus with SARS-CoV-2 spike (S) protein (Robbiani et al., 2020; Schmidt et al., 2020) (STAR Methods). We detected serum neutralization in 11 of 14 (79%) subjects (Figure S1A; Table S1). ID_{50} titers ranged from 51 to 655, and no correlation was seen between serum neutralization and time since diagnosis, age, or gender of the subjects (Figures S1B–S1D; Table S1).

SARS-CoV-2 binding B cell repertoires are enriched for class 1 nAbs

To characterize the B cell response against the SARS-CoV-2 spike, we sorted a total of 6,113 B cells from 14 subjects that bound to the SARS-CoV-2 S or RBD (Wrapp et al., 2020) using fluorescence-activated cell sorting (FACS) (Figures 1A and 1B). The frequency of SARS-CoV-2 S- or RBD-binding B cells ranged from 0.05%–0.3% of CD19$^+$ B cells (Figures 1A and 1B). We profiled sorted cells by 5′ directed scRNA-seq for both mRNA and paired VDJ profiling, recovering matched single-cell VDJ and transcriptome profiles in 129–649 cells for SARS-CoV-2 S and 47–487 cells for RBD per donor (Figure 1C). We identified clonally related B cells in each donor by accounting for V and J gene similarities and sequence similarity between the CDRH3 amino acid sequences (Nouri and Kleinstein, 2018). Expanded B cell clones with at least 2 clonally related cells accounted for 7%–45% of sorted B cells in the 14 subjects (Figure 1D).

We tested if our B cell repertoires include cells that underwent somatic hypermutation and class switch recombination, two steps in the generation of high affinity mAbs (Victora and Nussenzweig, 2012). We found that the fractions of immunoglobulin (Ig)G$^+$, IgM/IgD$^+$, and IgA$^+$ B cells varied substantially among subjects (9%–48%, 48%–87%, and 3%–12%, respectively) (Figure S1E). When we investigated clonal expansion within each Ig isotype, we found that in 8 of 14 subjects, IgM$^+$ clones were statistically significantly more expanded than either IgA$^+$ clones or IgG$^+$ clones or both (Figure S1F). Inferring levels of heavy chain somatic mutations (from RNA) (STAR Methods), the total number of mutations was lower in SARS-CoV-2 S- and RBD-binding B cells than in historic memory B cell (MBC) controls (Rubelt et al., 2012) (Figure S1G) with IgM$^+$ and IgD$^+$ cells showing significantly lower levels compared to IgG$^+$ and IgA$^+$ B cells (Figure S1H). Lower levels of somatic mutations were especially observed in IgM$^+$ B cells with low clonal expansion because 9 of 14 subjects showed a statistically significant positive correlation between clone size and number of mutations in their IgM$^+$ repertoire (Figure S1I).

We next tested if our sorted B cells were enriched for Ig genes *VH3-53* and *VH3-66* with short CDRH3 regions, features that are preferentially found among class 1 nAbs (Barnes et al., 2020b; Wu et al., 2020a; Yuan et al., 2020). 13 of the 14 recovered donors showed a higher fraction of combined *VH3-53/VH3-66* in B cell repertoires against SARS-CoV-2 S, RBD, or both compared to historic MBC controls (Rubelt et al., 2012). This difference was statistically significant in 10 of 14 (71%, false discovery rate [FDR] <0.1, two-proportions Z test) subjects (Figure 1E) and remained significant in 10 of 14 (71%, FDR <0.1, two-proportions Z test) subjects when considering only mAbs with CDRH3 regions shorter than 14 amino acids. Among other Ab features, CDRH3 length and hydrophobicity were slightly increased and CDRH3 charge was decreased compared to historic controls, and these differences existed for both S- and RBD-binding B cells (Figures S1J–S1L) and across Ig isotypes (Figures S1M–S1O). Thus, the B cell repertoire that binds to SARS-CoV-2 S and SARS-CoV-2 RBD in recovered individuals is enriched for heavy chain genes that are associated with class 1 nAbs.
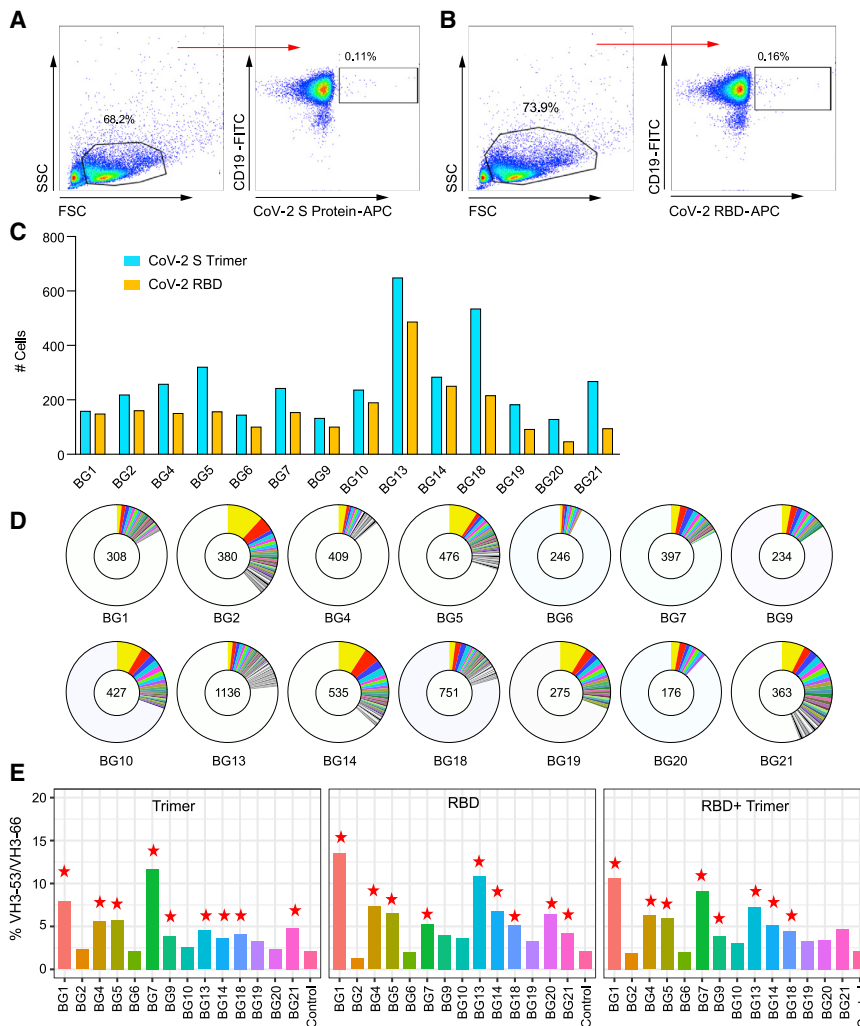
Figure 1. SARS-CoV-2 binding B cell populations in 14 recovered subjects

(A and B) Representative FACS plots with the gating strategy for sorting of SARS-CoV-2 S (A) and RBD binding (B) B cells. Pre-enriched CD20+ cells were gated on live cells based on their appearance in side scatter (SSC) and forward scatter (FSC). Of these, CD19-FITC and SARS-CoV-2 S-APC or SARS-CoV-2 RBD-APC double-positive cells were selected for sorting and sequencing.

(C) Bar diagram showing the number of cells for which transcriptional profile and matching VDJ sequences were obtained in each subject against SARS-CoV-2 S (turquoise) and SARS-CoV-2 RBD (yellow).

(D) Pie charts showing the total number of B cells sorted from each subject in the center of each pie and expanded B cell clones represented by differently colored pie slices. The white areas in each pie chart represent singlets.

(E) Bar diagram showing the fraction (in %) of *VH3-53* or *VH3-66* genes among SARS-CoV-2 S binders (left), RBD binders (center) and both combined (right) in each donor. Red stars indicate fractions with statistically significant difference (p value < 0.005) to historic control MBCs (Rubelt et al., 2012).

See also Figure S1 and Table S1.

opment (Wardemann et al., 2003) but can be generated during affinity maturation (Tiller et al., 2007). Ab responses to HIV-1 envelope trimer, for example, display high levels of polyreactivity, which was suggested to be a means to increase Ab avidity (Mouquet et al., 2010) and binding to divergent HIV-1 envelope strains (Prigent et al., 2018). At the same time, polyreactivity negatively affects half-life and clinical utility of mAbs (Horwitz et al., 2013; Shingai et al., 2014).

To assess polyreactivity, we tested all 92 isolated mAbs for binding to single-stranded DNA (ssDNA), double-stranded DNA (dsDNA), insulin, bacterial lipopolysaccharide (LPS), and streptavidin-APC by ELISA (Wardemann et al., 2003). We included streptavidin-APC as an antigen to assess any potential off-target binding of B cells to the staining reagent used in FACS (STAR Methods). 11 of 92 (12%) mAbs and 6 of 56 (11%) intermediate or strong binders to SARS-CoV-2 S or RBD showed reactivity against two or more of the four polyreactivity antigens in ELISA (Figure S2E; Table S3), significantly less than polyreactivity frequencies detected in healthy MBCs (22.7%) (Tiller et al., 2007) or HIV-specific B cells (75%) (Mouquet et al., 2010). In addition, none of our mAbs were found to be reactive in a polyreactivity ELISA assay against baculovirous lysate (Hötzel et al., 2012) (Table S3; STAR Methods). We conclude that most mAbs isolated from SARS-CoV-2 S-and RBD-binding B cells are not polyreactive when expressed as IgG1.

SARS-CoV-2 spike binding mAbs are directed against RBD and targets outside of the RBD

To functionally evaluate selected mAbs, we chose 4 of the 14 subjects with the highest serum neutralization titers (Figure S1A; Table S1) and produced a total of 92 mAbs from these donors (Table S2). The selection of mAbs included 72 representatives from most of the expanded B cell clones in these subjects and 20 singlets (Figures S2A–S2D). All of the selected mAbs were expressed as IgG1s in order to allow for direct comparison of binding and neutralization and were initially evaluated for binding by ELISA. 56 of 92 mAbs (61%) showed strong or intermediate binding to either SARS-CoV-2 S, RBD, or both in ELISA (Figure 2A; Table S3). 42 of 56 strong or intermediate binders (75%) bound to both SARS-CoV-2 S and RBD, 9 of 56 (16%) only bound to SARS-CoV-2 S, and 5 of 56 (9%) only to RBD (Figure 2A; Table S3).
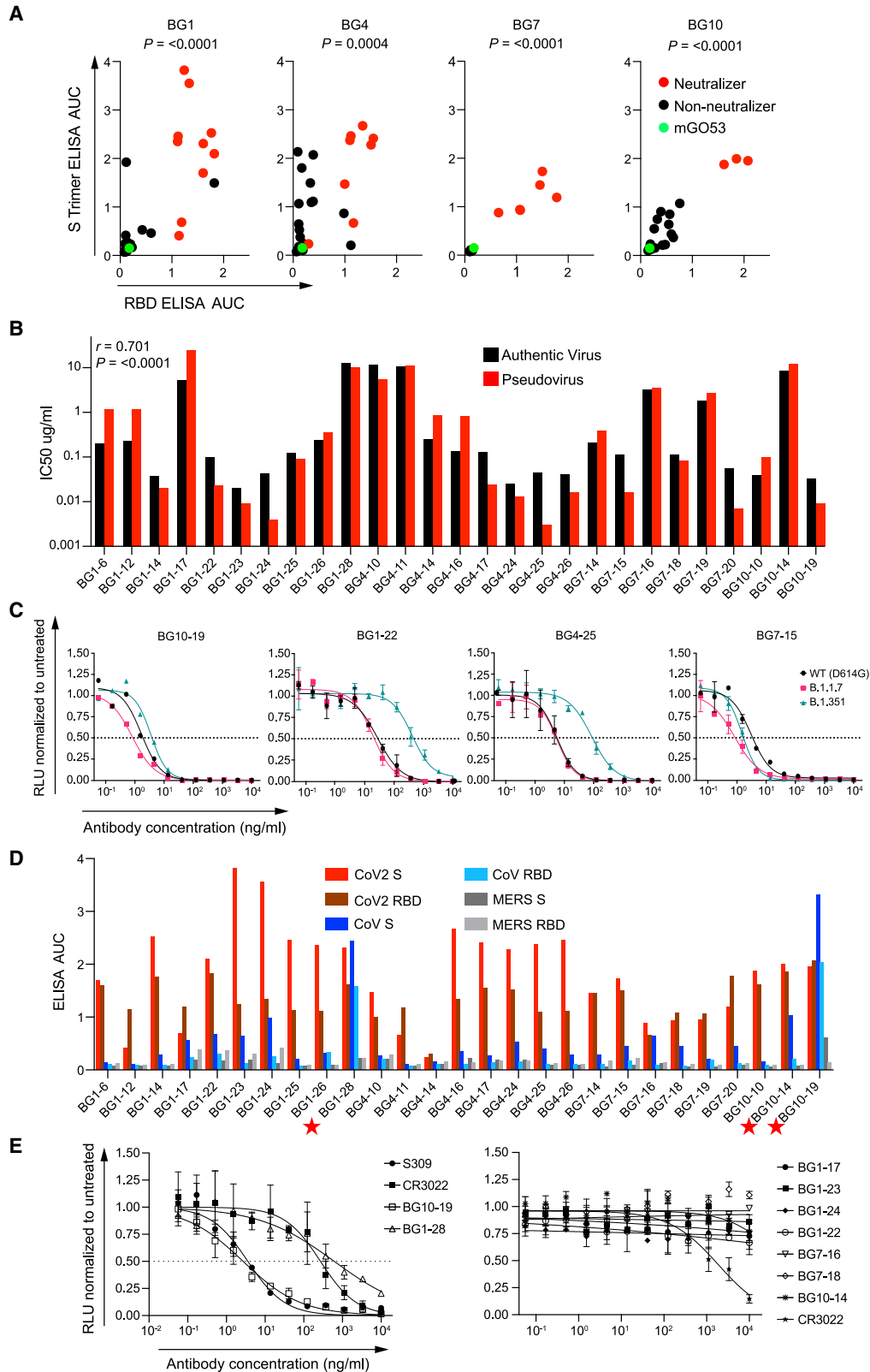
mAbs isolated from SARS-CoV-2 S- and RBD-binding B cells are typically non-polyreactive

Polyreactivity, non-specific binding to unrelated antigens, is a feature of Abs that is selected against throughout B cell devel-

(legend on next page)

nAbs against SARS-CoV-2 mostly arise from IgG⁺ B cells and target the RBD

We next screened all 92 mAbs for neutralizing activity in a pseudotyped virus neutralization assay (Robbiani et al., 2020; Schmidt et al., 2020) (above and STAR Methods). 27 of 92 mAbs (29%) showed neutralizing activity when tested up to a concentration of at least 25 μg/mL, and nAbs were identified from all 4 selected subjects (Figure S2F; Tables S2 and S3). IC$_{50}$ values ranged from 3 ng/mL to 25 μg/mL with a median of 99 ng/mL (Figure S2F; Table S2). Neutralizers showed at least intermediate binding in ELISA to both SARS-CoV-2 S trimer and RBD, with the exception of BG4-14, a weak neutralizer with binding by ELISA only to RBD (Tables S2 and S3).

Neutralizing activity was detected for 21 of 42 mAbs (50%) selected from IgG⁺ cells compared with 4 of 35 (11%) from IgM⁺/D⁺ cells and 2 of 15 (13%) from IgA⁺ cells ($\chi^2 = 15.9$, p value 0.0004) (Tables S2 and S3). When we tested the 27 neutralizers in a neutralization assay against authentic SARS-CoV-2, we found the results between both SARS-CoV-2 neutralization assays to be comparable (correlation coefficient [r] for comparison between IC$_{50}$ values 0.701, p value <0.0001) (Figure 2B; Table S2). We conclude that nAbs targeting the RBD of SARS-CoV-2 were present in all four selected subjects mostly arise from IgG⁺ B cells and are active against both pseudotyped and authentic SARS-CoV-2.

Select mAbs retain potent neutralizing activity against circulating variants B.1.1.7 and B.1.351

Several circulating variants of SARS-CoV-2, including B.1.1.7 and B.1.351 (Davies et al., 2021; Tegally et al., 2020) show decreased sensitivity to some SARS-CoV-2 mAbs, polyclonal sera from recovered COVID-19 donors (Wibmer et al., 2021) and sera from SARS-CoV-2 mRNA vaccinees (Liu et al., 2021; Wang et al., 2021; Wu et al., 2021). We produced pseudotyped SARS-CoV-2 viruses carrying the reported spike mutations in found these variants (STAR Methods) and tested our most potent mAbs (BG10-19, BG1-22, BG4-25, and BG7-15) in pseudovirus neutralization assays (Figures 2C and S2H). All four mAbs neutralized B.1.1.7 with similar potency as wild-type (WT) (D614G) and both BG10-19 and BG7-15 retained neutralization potency against B.1.351, whereas both BG1-22 and BG4-25 showed a 15-fold increase in IC$_{50}$ values against this variant (Figures 2C and S2G). We conclude that BG10-19 and BG7-15 retain potent neutralizing activity against SARS-CoV-2 variants B.1.1.7 and B.1.351, likely by recognizing an epitope outside of variant RBD mutations.

BG10-19 potently neutralizes both SARS-CoV-2 and SARS-CoV

mAbs that target conserved epitopes among different betacoronaviruses are subject of intense investigation given their potential utility in future coronavirus outbreaks. A small set of mAbs that were isolated from SARS-CoV-infected individuals have been shown to cross-react with SARS-CoV-2 (Pinto et al., 2020) and vice versa (Robbiani et al., 2020).

To evaluate potential cross-reactivity of our mAbs to other coronaviruses, we tested all 92 mAbs for binding to SARS-CoV and MERS-CoV spike (S) protein and RBD in ELISA (Figure 2D; Table S3). Two SARS-CoV-2 non-neutralizing mAbs showed strong cross binding to MERS (BG4-23 and BG1-13), one of which (BG4-23) also showed strong cross binding to SARS-CoV (Table S3). Three SARS-CoV-2 neutralizers (BG1-28, BG10-14, and BG10-19) showed strong cross-binding to SARS-CoV (Table S3). Of these, only BG10-19 neutralized SARS-CoV potently in a pseudovirus neutralization assay with an IC$_{50}$ value of 3 ng/mL compared with 20 ng/mL for S309, a cross neutralizing mAb isolated from a SARS-CoV patient (Figure 2E) (Pinto et al., 2020). BG10-19 also neutralized SARS-CoV-2 more potently than S309 with an IC$_{50}$ of 9 ng/mL compared to 79 ng/mL (Table S2) (Pinto et al., 2020). BG1-28 and BG10-14 did not neutralize SARS-CoV and neither did a selection of SARS-CoV-2 neutralizers that showed intermediate cross binding to SARS-CoV in ELISA (Figure 2E; Table S3).

IgA dimerization increases neutralization of SARS-CoV-2

Secreted IgA and IgM can, if expressed with a J chain, multimerize and therefore increase overall avidity depending on the density and accessibility of the antigen binding sites (Klein and Bjorkman, 2010). Consistent with this, some IgA dimers of SARS-CoV-2 nAbs show increased neutralizing potency (Wang et al., 2020).

To test the effect of dimerization on neutralizing activity in our mAbs, we expressed 13 of the 15 mAbs that were derived from IgA⁺ B cells (Tables S2 and S3) as IgA monomers and dimers (Figures S2H and S2I) and tested them in a pseudotyped SARS-CoV-

---

Figure 2. mAb neutralization, cross-binding, and cross-neutralization

(A) Dot plots showing ELISA binding of all expressed mAbs against SARS-CoV-2 S (y axis) and RBD (x axis) (Table S3) expressed as area under the curve (AUC) for subjects BG1, BG4, BG7, and BG10, respectively. Red dots represent neutralizers and black dots non-neutralizers when expressed as IgG1 and tested in a SARS-CoV-2 pseudovirus assay (Tables S2 and S3). Green dots represent negative control mAb mGO53 (Wardemann et al., 2003). Two tailed p values were generated by calculating Spearman correlation coefficient. High binding is defined as AUC >1, intermediate binding as AUC 0.25–1, and low binding as AUC <0.25.

(B) Bar diagram showing the IC$_{50}$ values in μg/mL (y axis) against SARS-CoV-2 pseudovirus in red and authentic SARS-CoV-2 virus in black for indicated mAbs (Table S2). Pearson correlation coefficient (r) and p value were calculated comparing results from both assays.

(C) Normalized relative luminescence values in cell lysates after infection with SARS-CoV-2 pseudoviruses harboring WT-D614G (black), B.1.1.7 (hot pink), or B.1.351 (green) sequences in the presence of indicated mAbs. Data points represent the mean of two experiments, with error bars representing the SD.

(D) Bar diagram showing the ELISA AUC for SARS-CoV-2 nAbs (Table S2) against SARS-CoV-2 S (red), SARS-CoV-2 RBD (brown), SARS-CoV S (dark blue), SARS-CoV RBD (light blue), MERS-CoV S (dark gray), and MERS-CoV RBD (light gray) (Table S3). Three mAbs showing strong cross reactivity against SARS-CoV are indicated with red stars.

(E) Pseudovirus neutralization assay comparing BG1-28, BG10-19, and S309 (left panel) or several SARS-CoV reactive mAbs (Table S3) and CR3022 (right panel) against SARS-CoV. Data points for neutralization assays represent the average of duplicates, with error bars representing the SD.

See also Figure S2.
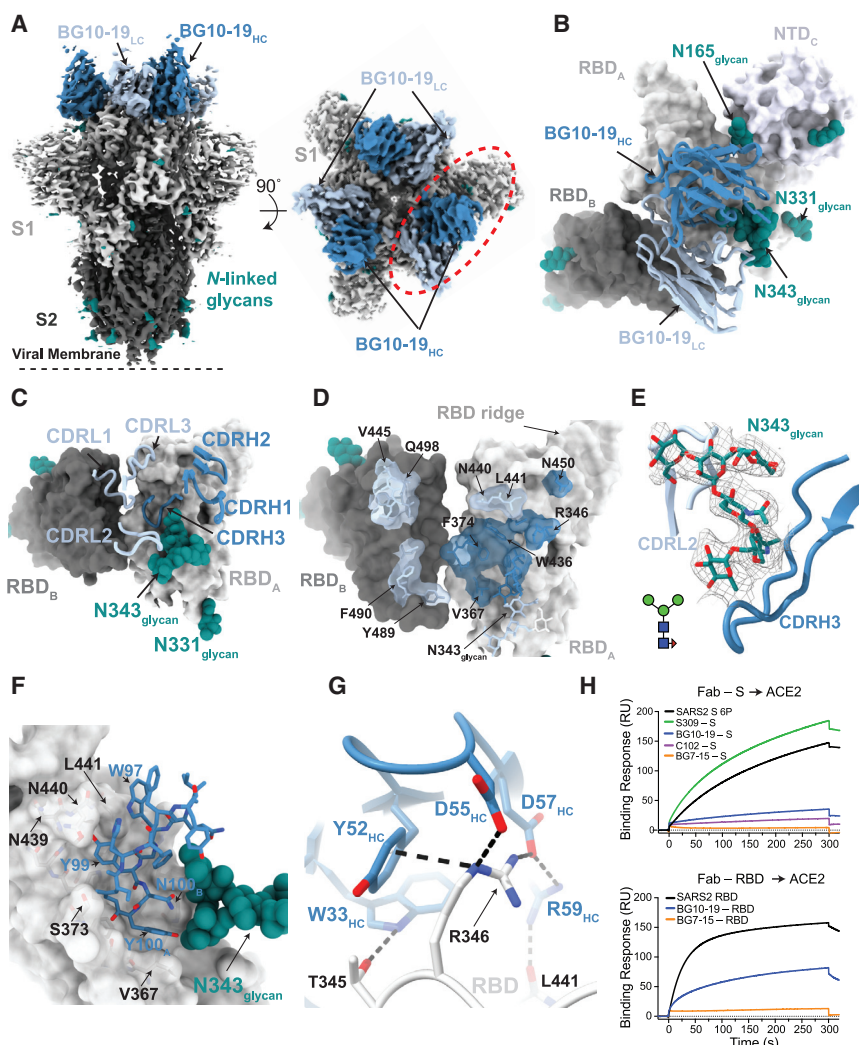
Figure 3. Cryo-EM structure of the BG10-19-S complex illustrates a distinct binding mode

(A) 3.3Å cryo-EM density for the BG10-19-S trimer complex. Side view (left panel) illustrates orientation with respect to the viral membrane (dashed line). Red circle (right panel) highlights quaternary epitope of BG10-19.

(B) Close-up view of quaternary epitope highlighted in (A) of BG10-19 (blue) involving bridging interactions that span neighboring protomers.

(C) BG10-19 CDR loops (cartoon) mapped on the RBD surface.

(D) Surface representation of BG10-19 quaternary epitope colored for BG10-19 heavy chain (blue) and light chain (light blue) interactions.

(E) Cryo-EM density map contoured at 5 σ around the $N343_{RBD}$-glycan (sticks), which interfaces with the BG10-19 CDRH3 (blue) and CDRL2 (light blue) loops. Inset: schematic of $N343_{RBD}$-glycan (blue square, *N*-acetylglucosamine; green circle, mannose; red triangle, fucose).

(F) BG10-19 CDRH3 (sticks) buries into a concave pocket formed by core RBD residues near the N343-glycan (spheres).

(G) BG10-19 CDRH2 (blue) interactions with RBD residue R346 (gray). Potential cation-pi and hydrogen bond interactions are illustrated by dashed black lines.

(H) SPR experiments to assess ACE2 binding to SARS-CoV-2 S trimer or RBD alone (black curves) and when complexed with Fabs (colored curves). See also Figure S3 and Table S5.

gle-particle cryo-electron microscopy (cryo-EM) structure of a complex between SARS-CoV-2 S trimer (Hsieh et al., 2020) and the BG10-19 Fab (Figures 3 and S3; Table S5).

The BG10-19 S structure revealed S trimers adopting a closed conformation bound to three BG10-19 Fabs (Figures 3A and S3A–S3D). BG10-19 recognizes a quaternary epitope comprising interactions that bridge two neighboring RBDs and the $N165_{NTD}$-glycan on the adjacent NTD (Figure 3B). Specifically, BG10-19 uses five of its six complementarity-determining region (CDR) loops to interact with a proteoglycan epitope focused atop the RBD α1 (residues 338–347) and α2 (residues 364–374) helices, with additional contacts with residues 436–450 (Figures 3C–3E). The $N343_{RBD}$-glycan (modeled as a complex-type pentasaccharide) interfaces with both CDRH3 and CDRL2 loops, including contacts with the core fucose moiety in a manner similar to the cross-reactive mAb S309 (Figure 3E) (Pinto et al., 2020). The CDRH2 and CDRH3 loops mediate the majority of RBD contacts (~760 Å² of ~1,090 Å² total paratope buried surface area [BSA]), establishing extensive polar and van der Waals interactions with RBD residues (Figures 3F and 3G). Collectively, interactions mediated by CDRH1-3 and CDRL2 loops establish the primary epitope recognized by BG10-19, which does not overlap with the ACE2 receptor-binding motif (RBM) (Figure S3E) and accounts

2 neutralization assay. Both mAbs that showed neutralizing activity against SARS-CoV-2 as IgG1 (BG1-23 and BG1-26) showed similar neutralization potency when expressed as IgA monomers. In dimeric form, BG1-23 and BG1-26 neutralizing activity increased with molar neutralization ratios (MNRs) (Klein and Bjorkman, 2010) of 6 and 8, respectively, suggesting an added avidity effect (Figures S2J and S2K). 6 of the mAbs that had not shown any neutralizing activity as IgG1 neutralized SARS-CoV-2 either only as dimeric IgA (BG10-5) or both as IgA monomer and dimer (Figures S2J and S2K). MNRs >2 were observed for weakly neutralizing IgA dimer BG1-27 (MNR = 3) and potently neutralizing IgA dimer BG10-8 (MNR = 10.86), suggesting that in these cases dimerization leads to increased overall avidity of the Ab (Figures S2J and S2K). We conclude that the neutralizing activity of some SARS-CoV-2 mAbs can be increased through expression as monomeric or dimeric IgA.
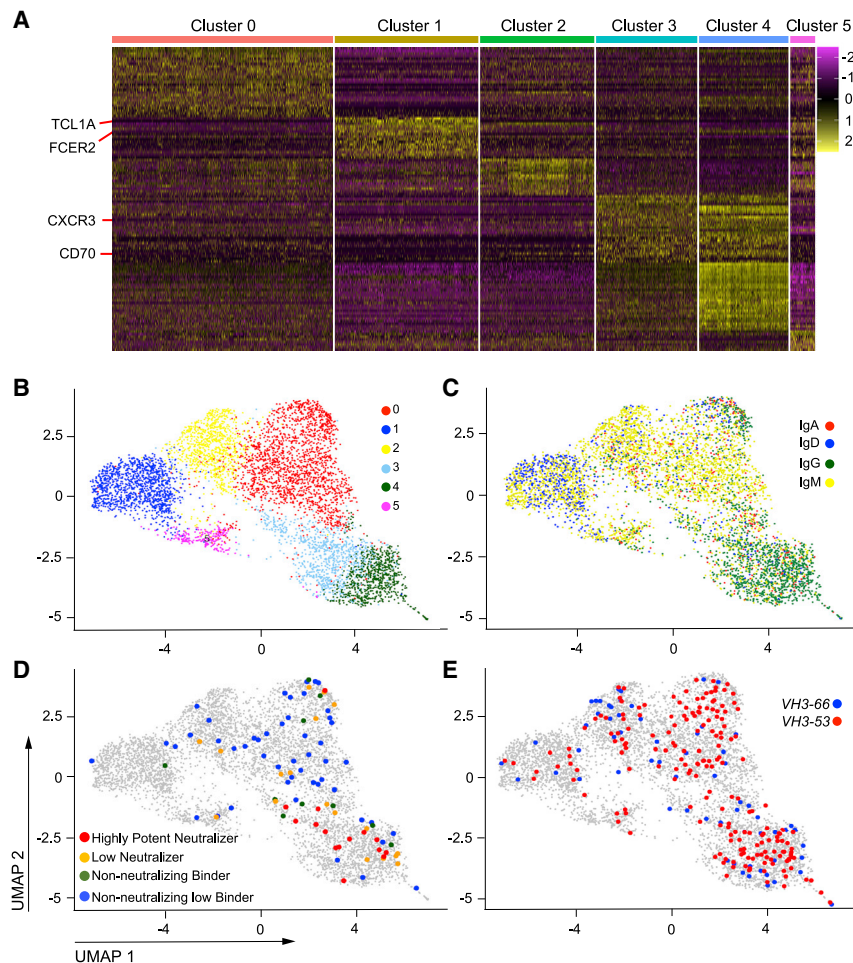
Structure of a BG10-19-SARS-CoV-2 S trimer complex

To understand the mechanism of BG10-19-mediated neutralization of SARS-CoV-2 and SARS-CoV, we determined a 3.3Å sin-

A

Figure 4. B cell transcriptome analysis

(A) Heatmap displaying the relative expression levels of the top 15 marker genes of the 6 clusters (rows) across cells (columns) (*Z* score normalization, row normalized). Marker genes that are known to be differentially expressed in particular B cell developmental stages are indicated (Table S4 for a full list of marker genes).

(B) Uniform manifold approximation and projection (UMAP) plot displaying the cells defined by their single-cell transcriptome measurements. The cells are colored based on their cluster assignments by the Louvain clustering algorithm.

(C) Same UMAP plot as in (B) but with cells colored based on their Ig isotypes: IGHD in blue, IGHM in yellow, IGHA in red, and IGHG in green.

(D) Same UMAP plot as in (B) but cells colored based on mAb binding and neutralization: highly potent SARS-CoV-2 neutralizers (IC$_{50}$ <0.1 μg/mL) in pseudovirus neutralization assay as either IgG1 or IgA monomer) in red, low neutralizers (IC$_{50}$ ≥0.1 μg/mL) in yellow, non-neutralizing high binders in green, and non-neutralizing low binders in blue (Figure S2J; Tables S2 and S3).

(E) Same UMAP plot as in (B) but cells with Ab CDRH3 shorter than 14 amino acids and *VH3-53* or *VH3-66* are shown in red and blue, respectively. See also Figures S4 and S5, Table S4, and Data S1.

for 87% of epitope BSA on the S trimer (~925 Å^2 of peptide BSA and ~220 Å^2 glycan BSA).

However, unlike the binding mode of S309, BG10-19 adopts a pose that positions the light chain CDRL1 loop and FWR3 atop a neighboring "down" RBD, which contributes an additional ~150 Å^2 BSA to the total quaternary epitope (Figures 3A–3D). This binding orientation is distinct from previously described nAbs that utilize interactions of long CDRH3s to mediate bridging interactions to stabilize the S trimer in a closed state (Barnes et al., 2020a; Tortorici et al, 2020). Interestingly, BG10-19 interactions with the neighboring RBD also prevent sampling of the "up" RBD conformation (Figure S3C). Indeed, SARS-CoV-2 S trimer binding to immobilized sACE2-CH3 (Tada et al., 2020) was blocked in the presence of BG10-19 Fab, while a RBD-BG10-19 complex was capable of binding sACE2 in SPR experiments (Figure 3H). These data suggest that BG10-19 utilizes a neutralization mechanism that inhibits exposure of the ACE2 RBM, by locking the S trimer into a closed conformation.

Sequence conservation at the BG10-19 epitope explains the potent cross-neutralizing activity against SARS-CoV (Figure 2E), in that 23 of 29 residues are strictly or conservatively substituted between SARS-CoV-2 and SARS-CoV RBDs (Figure S3F). Given the conserved nature of the BG10-19 epitope, we characterized

the potential of BG10-19 to cross-react with zoonotic sarbecoviruses. Bat coronavirus strains WIV1-CoV and SCH014-CoV are clade 1 sarbecoviruses and ACE2-tropic (Li et al., 2003). When we assessed BG10-19 cross-reactivity to these viruses, we observed binding to WIV1-CoV RBD at the same levels as SARS-CoV-2 and SARS-CoV but no neutralizing activity (Figures S3G–S3J). The lack of neutralizing activity against WIV1-CoV was surprising, given its 95% amino acid sequence identity with SARS-CoV (Cohen et al., 2021; Pinto et al., 2020). Overall, our findings suggest that the SARS-CoV-2 trimer-specific Ab response includes rare mAbs such as BG10-19 with highly potent cross-neutralizing activity against SARS-CoV.

SARS-CoV-2 S- and RBD-binding B cell repertoires include different B cell populations

As mentioned above, our scRNA-seq approach pairs VDJ sequences and expression profiles of B cell populations sorted from 14 convalescent subjects, and can therefore provide insights into the expression states of SARS-CoV2-specific B cells. These B cells were selected based on expression of CD20, CD19, and SARS-CoV-2 S or RBD binding alone without selection for other surface markers (STAR Methods and above). We profiled 6,113 sorted B cells, revealing 6 distinct transcriptional cell clusters (TCs) (Figures 4A and 4B) that had representation from all donors, although with enrichment of some donors in specific clusters (Figure S4A and see below). These clusters were neither dependent on binding to SARS-CoV-2 S or RBD

(Figure S4B) nor on cell-cycle phase (Figure S4C). CD44 and CXCR4 were expressed in cells from all TCs, consistent with their frequent expression among mature B cells (Figure S4D) (Kremmidiotis and Zola, 1995; Nagasawa et al., 1996; Nie et al., 2004). CD38 expression levels were low throughout all clusters, in keeping with our selection of B cells expressing surface Ig binding to SARS-CoV-2 S or RBD (Ellebedy et al., 2016) (Figure S4D). The cell clusters were distinguished by increased expression of specific marker genes (Figure 4A), such as genes associated with different B cell populations, including naive and MBCs, consistent with isotype, mutation status, and clonal expansion features of these cells. Specifically, the TC1 marker genes *FCER2* (CD23) and *TCL1A* are known to be highly expressed in mature naive B cells (Figure 4A; Table S4) (Horns et al., 2020), consistent with an enrichment in TC1 of IgD$^+$ and IgM$^+$ B cells (36% and 63% of cells, respectively) (Figure S4E) with low levels of inferred somatic mutations (Figure S4F) and minimal clonal expansion (Figures S4G and S4H). In TC3 and TC4, CD27 and CD80, both expressed in MBCs (Moroney et al., 2020; Zuccarino-Catania et al., 2014), were highly expressed (Figure S5A), and the majority of cells in these clusters were IgG1$^+$ (53% and 73% of cells, respectively) (Figure S4E), somatically mutated (Figure S4F) and more clonally expanded than cells in TC1 (Figures S4G and S4H). Cells in TC3 and TC4 also highly expressed CXCR3, a chemokine receptor found on some class switched B cells that is believed to facilitate migration to sites of inflammation (Moroney et al., 2020; Muehlinghaus et al., 2005) and CD70, which is upregulated on stimulated B cells where its interaction with CD27 on effector T cells plays an important role in antiviral T cell responses (Izawa et al., 2017; van Gisbergen et al., 2011) (Figures 4A and S5A).

In the weeks following vaccination or infection with influenza or infection with Ebola, antigen-specific B cells can present as Ab secreting cells, MBCs or "activated B cells" (ABCs), which wane after several weeks and show relatively higher expression levels of CD52, TLR10, CD19, and CD20 (Ellebedy et al., 2016). To test if either TC3 or TC4 include ABCs, we examined the distribution of expression levels in each cell cluster of CD52, TLR10, CD19, and CD20 and 10 other genes that are expressed at higher levels in ABCs compared to MBCs (Figure S5A) (Ellebedy et al., 2016). All 14 genes were significantly higher expressed (one-tailed t test, FDR <0.01) in TC4 than in TC3 (Figure S5A). Thus, SARS-CoV-2 S- and RBD-binding B cell repertoires in recently recovered subjects include ABCs (TC4) and MBCs (TC3) that are both mostly IgG1$^+$ and show expansion of B cell clones and somatic hypermutation. We also detected IgD$^+$ and IgM$^+$ mature naive B cells (TC1) with low levels of somatic hypermutation, minimal clonal expansion, and high expression of CD23 and TCLA1.

MBCs and ABCs generate binding and neutralizing Abs
To relate mAbs with high levels of binding to or neutralization of SARS-CoV-2 to B cells in certain TCs, we identified the clusters from which the 92 mAbs we produced and tested were derived. Because we selected mAbs for testing based on representation of expanded clones (72/92) or randomly selected singlets that were mostly IgG$^+$ or IgA$^+$ (20/92), all TCs are not equally represented among the 92 mAbs (Table S3). Nevertheless, 20 of 33

(60%) neutralizers, 14 of 15 (94%) potent neutralizers (monomeric IC$_{50}$ ≤0.1 μg/mL), and 5 of 10 (50%) non-neutralizing high binders were derived from cells in TC3 and TC4, whereas 36 of 49 (73%) of the non-neutralizing low binders belonged to TC0 and TC2 (Figures 4D and S2J; Tables S2 and S3). The majority of neutralizers from TC3 and TC4 were derived from singlets or small clones and did not have clonal members in other TCs among the cells we sampled (Figure S5B; Table S3; Data S1). We further tested our clusters for enrichment in class 1 nAbs (*VH3-53/VH3-66* antibodies with short CDRH3 regions [Barnes et al., 2020a] and see above). *VH3-53/VH3-66* Abs were overall significantly enriched in TC3 and TC4 compared to TC1, TC2, and TC5 (two-tailed t test, p ≤ 0.0001) (Figures 4E and S5C), and 8 of 8 evaluated *VH3-53/VH3-66* nAbs with short CDRH3 regions were derived from B cells that belonged to either TC3 or TC4 (Tables S2 and S3). We conclude that the cells from which we isolated strongly binding and neutralizing mAbs against SARS-CoV-2 frequently had transcriptional profiles consistent with MBCs and ABCs.

Frequency of SARS-CoV-2 S- and RBD-binding ABCs and MBCs correlates with serum neutralizing activity
While MBCs and antibody-secreting plasma cells are two separate B cell compartments (Leyendeckers et al., 1999), they can originate from the same germinal center reaction, (Victora and Nussenzweig, 2012) and antibodies against HIV-1 envelope derived from MBCs have been detected in serum from matched patients (Scheid et al., 2009). Whether the frequency of MBCs among SARS-CoV-2 S- and RBD-binding B cells correlates with plasma neutralizing activity in recently recovered subjects is not known. To test this, we measured if the frequency of cells from any TC correlated with serum neutralization in the 14 study subjects and found that the frequency of only TC3 and TC4 cells correlated positively with serum neutralization (Pearson's r = 0.64 and 0.66, p = 0.013 and 0.011, respectively) (Figure S5D), and this correlation was not significantly affected by correcting for time since COVID-19 diagnosis (Pearson's r = 0.69 and 0.76, p = 0.017 and 0.007, respectively). We conclude that expansion of both SARS-CoV-2 binding MBCs and ABCs correlate with serum neutralization titers against SARS-CoV-2 in convalescent COVID-19 patients.

VH3-53/VH3-66 Abs with long CDRH3s can adapt class 1 nAb structural poses
Given the enrichment of *VH3-53/VH3-66*-encoded Abs in TC3 and TC4, we selected two mAbs that were coded by cells in these clusters with distinct CDRH3 lengths for structural characterization. We solved a 3.0 Å crystal structure of Fabs from BG4-25 (*VH3-53*-encoded with 12 aa CDRH3) and the SARS-CoV mAb CR3022 (Tian et al., 2020) in complex with SARS-CoV-2 RBD (Figure S6A; Table S6). Consistent with the binding mode of class 1 nAbs (Barnes et al., 2020b; Yuan et al., 2020), BG4-25 recognizes an RBD epitope that overlaps with >90% of residues in the ACE2 RBM (Figure S6B), which is only fully accessible with "up" RBD conformations. Two V-gene encoded regions in class 1 nAbs prominently contribute to epitope recognition—the ^{31}SNY^{33} CDRH1 and ^{53}SGGS^{56} CDRH2 sequence motifs, which take part in extensive hydrogen bond interactions at the RBD interface
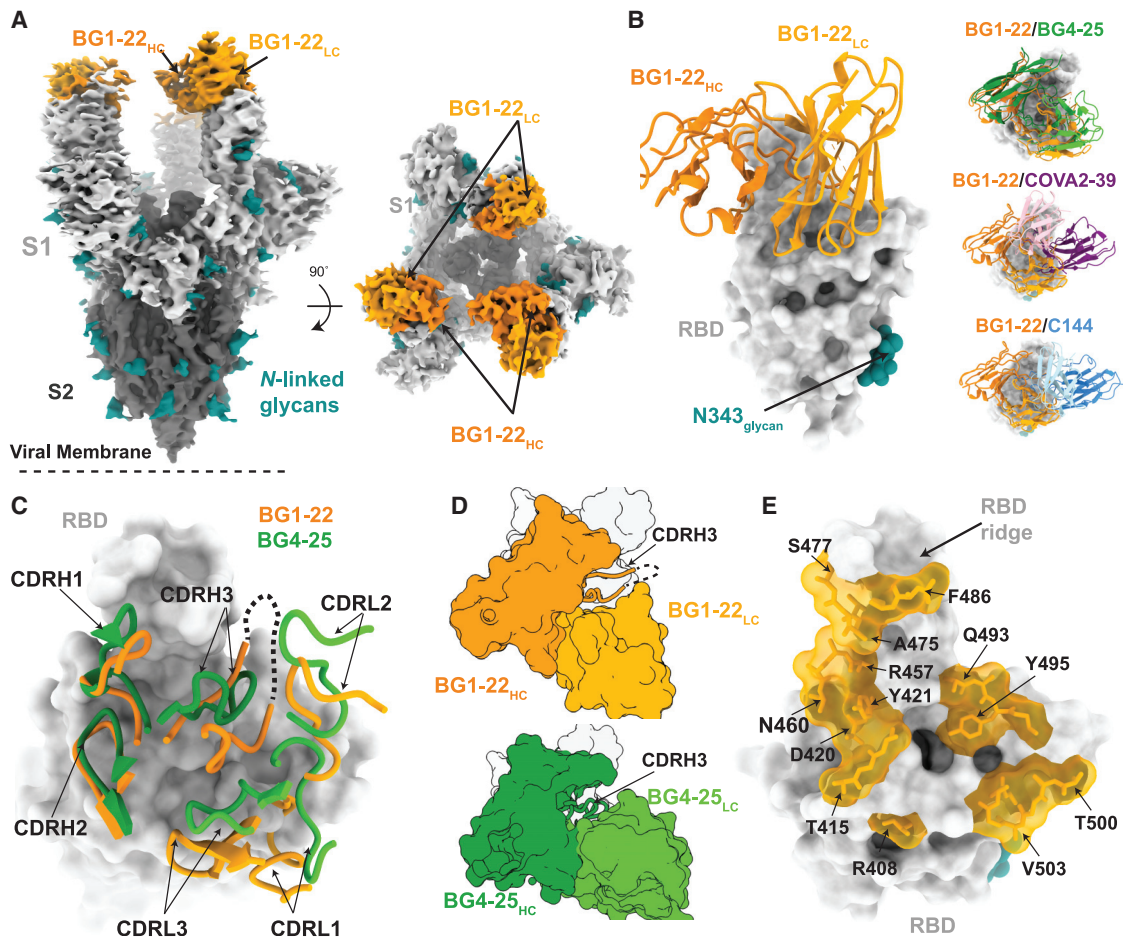
Figure 5. Cryo-EM structure of BG1-22-S trimer provides insight into the *VH3-53/VH3-6-*/long CDRH3 Ab binding mode
(A) Cryo-EM density for the BG1-22-S trimer complex.
(B) Left panel: close-up view of BG1-22 (orange) recognition of RBD epitope (gray surface). Right panels: overlay of VH3-53 mAbs BG4-25 (green), COVA2-39 (purple, PDB: 7JMP), and C144 (blue, PDB: 7K90) with BG1-22 (orange).
(C) BG1-22 (orange) and BG4-25 (green) CDR loops mapped on the RBD (gray surface). Disordered residues in the BG1-22 CDRH3 are denoted by a black dashed line.
(D) Flattened surface representation of BG1-22 (orange) and BG4-25 (green) with CDRH3 loops shown to highlight the displaced CDRH3 of BG1-22.
(E) Surface representation of the BG1-22 RBD epitope (orange). Underlying residues are shown as sticks.
See also Figure S6 and Tables S5 and S6.

(Tan et al., 2021; Wu et al., 2020b; Yuan et al., 2020). Analysis of inferred somatic mutations in 93 *VH3-53/VH3-66* mAbs coded in our collection of SARS-CoV-2 binding B cells with CDRH3 less than 14 amino acids (IMGT definition) (Lefranc et al., 2015) revealed frequent inferred mutations in these motifs, including S31R and S56T in the Ab heavy chain, which are observed in BG4-25 (Figures S6C–S6E). *VH3-53/VH3-66-* encoded Abs from SARS-CoV-2 binding B cells with short CDRH3s were also enriched for inferred mutations Y58F, F27L, and T28I, which have been shown to increase neutralization potency and affinity class 1 Abs (Hurlburt et al., 2020). Despite lacking these specific mutations, BG4-25 shows exceptional neutralizing activity, which is potentially explained by the F27I and S31R CDRH1 loop mutations that provide increased van der Waals interactions along the mAb-RBD interface (Figure S6D and S6E).

In addition to the recurrent class 1 nAbs defined by *VH3-53/ VH3-66-*encoded gene segments and short CDRH3s (e.g., BG4-25), a subset of *VH3-53/VH3-66-*encoded nAbs have been described with CDRH3 lengths >15 amino acids that would seemingly be incompatible with the binding mode of class 1 nAbs. A 3.7 Å cryo-EM structure of BG1-22 (*VH3-*53-encoded with 21 aa CDRH3) (Table S2) Fab complexed with stabilized S trimers revealed binding to "up" RBD conformations (Figures 5A and S6F–S6H). Local refinement to improve the cryo-EM density at the interface (Figure S6H) revealed a binding orientation of BG1-22 that was consistent with class 1 nAb binding modes (Figure 5B), which contrasts with previously characterized *VH3-53/VH3-66-*long CDRH3 antibodies (Barnes et al., 2020a; Wu et al., 2020a). To accommodate this binding mode, the 21-residue long CDRH3 of BG1-22 flips outward toward RBD residue Q493 resulting in a slight rotation of the Ab light chain relative
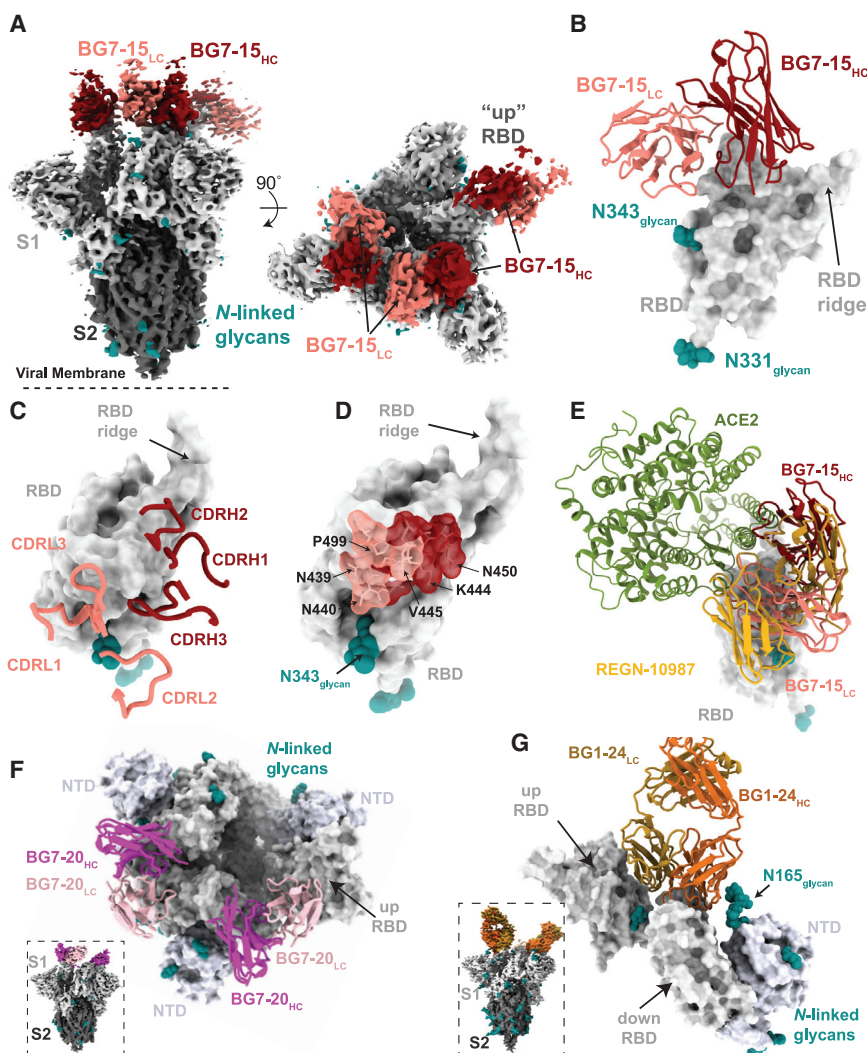
Figure 6. Cryo-EM structures of BG7-15, BG7-20, and BG1-24-S trimer complexes

(A) Cryo-EM density for the BG7-15-S trimer complex.

(B) BG7-15 (HC, red; LC, salmon) targeting of its RBD (gray surface) epitope. Glycans are depicted as teal spheres. Color coding will be the same throughout the remaining panels.

(C) BG7-15 CDR loops mapped on the RBD.

(D) Surface representation of BG7-15 epitope.

(E) Overlay of BG7-15 (red), REGN-10987 (gold, PDB: 6XDG), and hACE2 (green, PDB: 6M0J) on the RBD (gray surface).

(F) Top down view of BG7-20 (HC, magenta; LC, pink) bound to S trimer. Inset: cryo-EM density of BG7-20-S trimer complex.

(G) Close-up view of BG1-24 (HC, orange; LC, wheat) bound to RBD. Interactions with the adjacent up RBD and N165$_{NTD}$-glycan are shown. Inset: cryo-EM density of BG1-24-S trimer complex.

See also Figure S7 and Table S5.

Taken together, these results provide further insight into class 1 nAbs and suggest that longer CDRH3s, although infrequent, are not a restriction to V-gene mediated interactions at the RBD interface of this Ab class.

Structural characterization of nAbs with distinct epitope recognition and mutational escape patterns

To further understand the specificity of RBD-targeting, we determined cryo-EM structures of Fab-S complexes for three additional nAbs: BG7-15 (*VH1-18*-encoded, 11 aa CDRH3, IC$_{80}$ = 92 ng/mL), BG7-20 (*VH1-8*-encoded, 20 aa CDRH3, IC$_{80}$ = 23 ng/mL), and BG1-24 (*VH1-69*-encoded, 16 aa CDRH3, IC$_{80}$ = 7 ng/mL), to resolutions of 3.7, 4.0, and 3.9 Å, respectively (Figures 6 and S7; Table S5). In all cases, Fabs were bound to either up or down RBD conformations, demonstrating recognition of Ab epitopes in either state. Analysis of the BG7-15-S structure revealed an Ab epitope focused on RBD residues 439–451, mainly mediated by contacts with CDRH3 and CDRL3 loops (Figure 6B–6D). Overlay of BG7-15 and REGN-10987 (Hansen et al., 2020) showed a shared Ab footprint that binds outside the ACE2 RBM but would sterically hinder ACE2 receptor binding to RBD (Figures 3H and 6E) while allowing binding of class 1 nAbs (e.g., BG4-25, C102, and REGN-10933).

Cryo-EM structures of BG7-20 and BG1-24 S complexes revealed RBD-targeting similar to nAbs that belong to the class 2 binding mode (Barnes et al., 2020a). This class of SARS-CoV-2 nAbs recognizes up and down RBD conformations, overlaps with the ACE2 RBM, has secondary interactions with neighboring "up" RBDs, and has the potential for intra-protomer avidity effects. Consistent with class 2 nAbs, BG7-20 and BG1-24

to the canonical class 1 RBD-binding nAbs (Figures 5C–5E). The displaced CDRH3 conformation makes few sidechain interactions with the RBD, such that 6 residues of the CDRH3 loop are disordered (Figures 5C and 5D).

Although unliganded Fab structures often exhibit a disordered CDRH3 (e.g., 1RZI and 1RZF), it is unusual for an Ab bound to an antigen to exhibit a disordered CDRH3. From an examination of 731 Ab-antigen structures with resolutions of 3.5 Å or better in the Structural Antibody Database (SABDab) (Dunbar et al., 2014), we found only 6 with missing residue numbers between heavy chain residues 95 to 107, implying a disordered CDRH3 (PDBs 3LH2, 4JDT, 7JWB, 5ANM, 4M8Q, and 3LHP). None of these complexes involved conventional Ab-antigen pairs; instead, they were germline forms of Abs, the epitope was presented in a scaffold, or only the VH domain was involved in binding. This suggests that the orientation adopted by BG1-22 is not one that promotes CDRH3-mediated interactions with the antigen, as is classically observed in Ab-antigen structures, but instead simply accommodates the longer CDRH3 length by displacing much of the loop to outside the Ab-antigen interface.

show a similar epitope focused along the RBD ridge that overlaps with residues involved in ACE2 binding and includes contacts with E484, F486, and Q493. The binding pose of BG1-24 promotes stabilization of the $N165_{NTD}$ glycan, adding to the observation that class 2 nAbs can involve interprotomer glycan contacts (Cao et al., 2020). Interestingly, the N-glycan interaction is mediated by a hydrophobic Met-Phe sequence at the tip of CDRH2, a common feature of VH1-69 Abs (Chen et al., 2019). This feature has been attributed to facilitating broad neutralization by Abs against influenza and hepatitis C (Guthmiller et al., 2020; Chen et al., 2019) and likely explains BG1-24's polyreactivity (Figure S2E; Table S3).

With the use of mAbs as therapeutic options for SARS-CoV-2 infection, understanding possible RBD mutations selected under mAb pressure and the frequency of SARS-CoV-2 isolates harboring RBD mutations that confer immune escape is critical. Although deep mutational scanning and in vitro selection experiments have facilitated the choice of therapeutic mAb cocktails, these experiments have also illustrated that in some cases single-point mutations are sufficient for viral escape (Greaney et al., 2021; Weisblum et al., 2020). Indeed, the SARS-CoV-2 spike variant N439K could limit the use of REGN-10987 as a therapy in SARS-CoV-2 infection by conferring escape (Barnes et al., 2020b), and the variant B.1.351 is resistant to its partner antibody REGN-10933 (Tada et al., 2021).

To assess the effects of RBD substitutions, we assayed ELISA binding and SARS-CoV-2 pseudovirus neutralization for 6 mAbs reported in this study against a panel of RBD substitutions (Figures 7A–7H). Decreased binding and neutralization potency was observed for most mAbs when RBD substitutions occurred within the Ab epitope and were consistent with RBD mutations known to decrease binding of mAbs in the same class (Figures 7B–7H) (Barnes et al., 2020a; Greaney et al., 2021). Notable exceptions included BG7-15, which showed neutralizing activity against the RBD N439K mutant that confers escape against REGN-10987, and BG4-25, which neutralized the class 1 escape variant A475V (Figures 7E and 7F). In general, decreased binding affinity correlated with RBD mutations that conferred viral escape in pseudotyped viral neutralization assays and were consistent with the observation that RBD mutations that affect antibodies from one class do not affect mAbs in a different RBD-targeting class (Figures 7C–7H). Given that several nAbs were non-competitive, we assessed nAb cocktails for synergistic neutralization effects (IC_{50eff} >1) against SARS-CoV-2 pseudovirus using a previously described synergistic model (West et al., 2010). Results suggest that only the BG10-19 + BG4-25 nAb combination demonstrated synergistic neutralizing activity (Figure 7I), consistent with published results for similarly classed nAb pairs (Hansen et al., 2020).

Finally, given the broad binding and neutralization activity of BG10-19 against a panel of SARS-CoV-2 RBD substitutions (Figures 7A and 7C), we utilized a rVSV/SARS-CoV-2 chimeric virus to determine spike variants that escape neutralization by BG10-19 (Weisblum et al., 2020) (STAR Methods). Initial attempts at selection experiments for BG10-19 showed no viral escape variants, consistent with observations for potently neutralizing convalescent plasma and some mAbs (Weisblum et al., 2020). However, after several passages, plaque-purified viruses

harboring the G339R and L441P mutations showed partial escape from BG10-19 (Figure 7J). We note that neither of these two mutations have so far been sequenced and deposited on the GISAID database (Elbe and Buckland-Merrett, 2017). Thus, we conclude that BG10-19's SARS-CoV-2/SARS-CoV cross neutralization and ability to tolerate single RBD mutations within its epitope makes it an attractive therapeutic candidate.

DISCUSSION

Abs play an indispensable role in antiviral responses both through their ability to neutralize (Corti and Lanzavecchia, 2013) and by engaging other components of the immune system through interactions with their Fc regions (Bournazos et al., 2020). Different viruses perturb Ab responses through characteristic mechanisms. HIV-1, for example, constrains efficient Ab responses through narrow structural pathways to broad neutralization (Scheid et al., 2011) and by causing B cell exhaustion (Moir et al., 2008).

In this study, we show from a comprehensive in-depth analysis of SARS-CoV-2 binding B cells from convalescent individuals that the repertoire of SARS-CoV-2 binding B cells includes MBCs and ABCs, as well as mature naive B cells. Interestingly, we found clonal cells to be present in TC0, which is enriched in IgM^+ B cells with inferred somatic mutations and low expression of CD27. Despite showing clonal expansion and somatic mutations, mAbs produced from this cluster were mostly low binding and non-neutralizing. We speculate that this cluster might contain cells from an early extrafollicular B cell response, as was observed in influenza infection (Lam and Baumgarth, 2019). On the other hand, high binding and potent neutralizing activity were mostly detected in mAbs isolated from ABCs and MBCs that shared transcriptional phenotypes across different individuals.

Immunologic correlates for protection from SARS-CoV-2 after vaccination or prior exposure are not defined, but studies of other respiratory viruses suggest that serum neutralization could play an important role in protective immunity against SARS-CoV-2 (Kulkarni et al., 2018; Verschoor et al., 2015). Consistent with other SARS-CoV-2 studies, we did not detect any intra-donor correlation between serum neutralization and the potency of mAbs (Robbiani et al., 2020), but we found a strong correlation between serum neutralization and the relative size of the ABC and MBC populations. This underscores the close relationship between high-affinity MBC responses and serum Ab activity in SARS-CoV-2. It will be important to investigate if a similar correlation exists in individuals who have been vaccinated against SARS-CoV-2 in an effort to delineate different responses to SARS-CoV-2 vaccines.

Our structural analysis revealed new insights into commonalities and differences among RBD-specific mAbs. For example, in common with potently neutralizing mAbs C144 (Barnes et al., 2020a) and S2M11 (Tortorici,et al 2020), BG10-19 bridges between adjacent RBDs to lock the S trimer into a closed conformation. However, in contrast to most previously described antibodies, BG10-19 recognizes a conserved epitope within the RBD core that is accessible in up/down RBD conformations on the spike trimer of both SARS-CoV-2 and SARS-CoV (unlike the conserved, cryptic CR3022 epitope only accessible on up
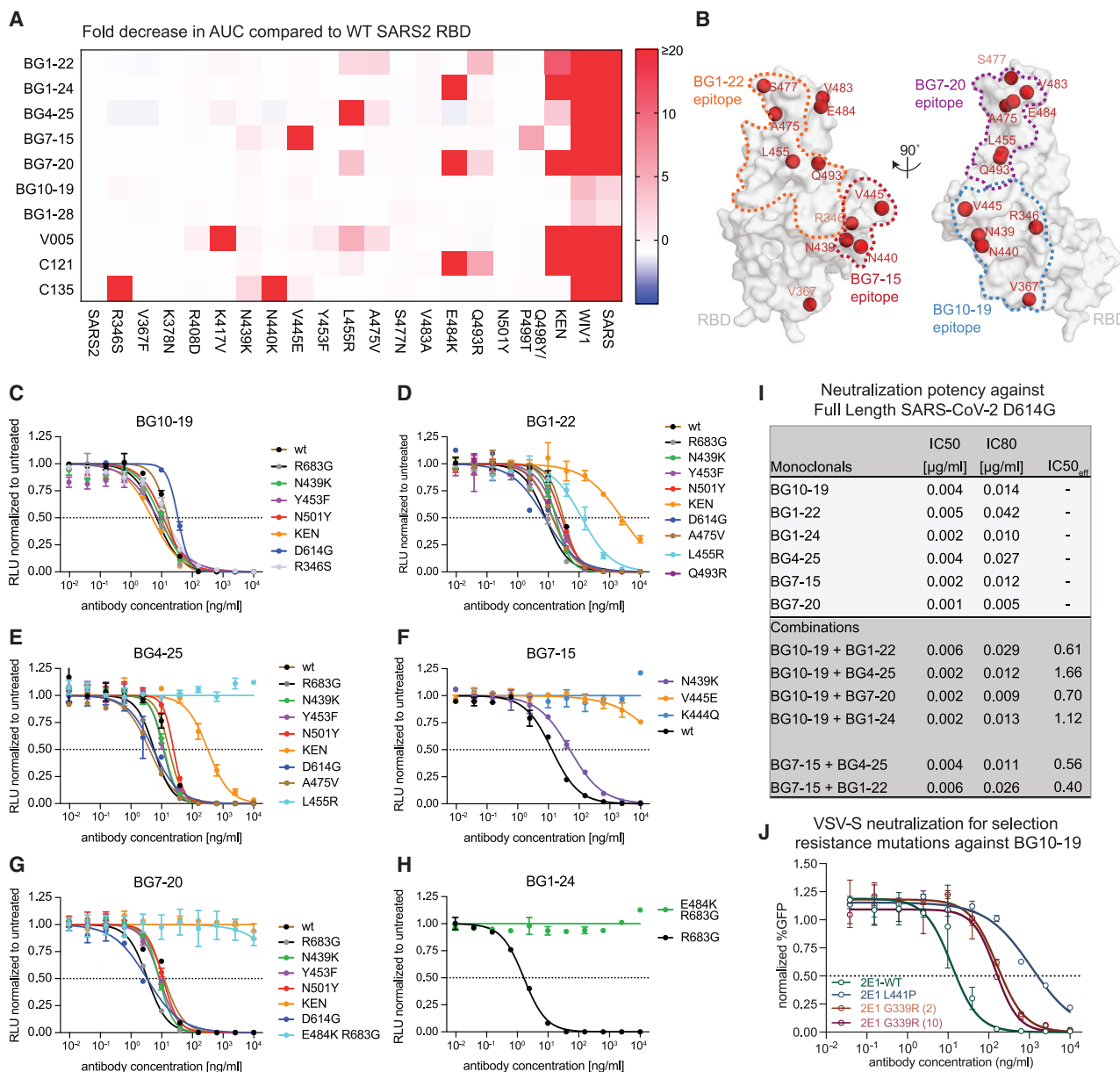
Figure 7. Effects of RBD substitutions on mAb binding and neutralization

(A) Heatmap showing the log fold change in ELISA AUC of Fabs binding to indicated SARS-CoV-2 RBD mutants relative to wild-type SARS-CoV-2 RBD binding. Mutations that lead to non-binding or decreases >20-fold relative to wild-type are shown as dark red.

(B) Surface representation of the SARS-CoV-2 RBD with mAb footprints (BG1-22, orange; BG7-15, red; BG1-24, magenta; and BG10-19, blue) shown as dashed lines and individual RBD substitutions shown as red spheres.

(C–H) Normalized relative luminescence values in cell lysates after infection with SARS-CoV-2 pseudoviruses harboring wild-type or RBD substitutions in the presence of the 6 indicated mAbs. KEN represents a SARS-CoV-2 pseudovirus encoding the K417N/E484K/N501Y RBD mutations. Data points represent the mean of two experiments, with error bars representing the SD.

(I) Summary table of IC_{50}, IC_{80}, and IC_{50eff} values measured for 6 different mAbs and mAb combinations against SARS-CoV-2 pseudoviruses. IC_{50eff} values were calculated based on synergistic models previously described (West et al., 2010).

(J) Infection of 293T/ACE2cl.22 cells by rVSV/SARS-CoV-2/GFP encoding the indicated spike mutations in the presence of increasing amounts of BG10-19. Infection was quantified by FACS after 16 h, with mean and SD from two technical replicates shown.

RBD conformations), which may allow design of immunogens that elicit cross-reactive protection against future emerging co-ronaviruses. BG10-19's unique binding/neutralization properties

and its resistance to all single RBD mutations identified in circulating isolates with a frequency >0.1% based on the GISAID database (Elbe and Buckland-Merrett, 2017), including those

found within the B.1.1.7 and B.1.351 lineages, make this a compelling therapeutic candidate in the arsenal against SARS-CoV-2.

Additionally, high-resolution structures of *VH3-53/VH3-66*-class mAbs provided further understanding of the rules that govern potent neutralization and viral escape from this recurring antibody class and showed that CDRH3 length may not be a limitation to VH gene segment-mediated interactions at the RBD interface. Collectively, these structures and insights into the cellular processes behind the induction of potent, cross-reactive nAbs will not only aid us in our battle to control the current COVID-19 pandemic through the use of safe and effective mAb treatments but will also provide additional criteria for the evaluation of humoral immune responses elicited from candidate vaccines against emerging zoonotic viruses with pandemic potential.

Limitations of study

Limitations of this study include that mAbs were selected for validation only based on membership in large, expanded clones (72 antibodies) and 20 singlets. Therefore, not all TCs were equally evaluated functionally. In addition, mAbs isolated from IgM⁺ B cells were only evaluated as IgG1 expressed monomers. The comparatively low affinity of these antibodies could potentially be improved *in vivo* if expressed as pentamers, similar to our observation of increased neutralization of some IgA mAbs when expressed as dimers.

STAR★METHODS

Detailed methods are provided in the online version of this paper and include the following:

- **KEY RESOURCES TABLE**
- **RESOURCE AVAILABILITY**
  - Lead contact
  - Materials availability
  - Data and code availability
- **EXPERIMENTAL MODEL AND SUBJECT DETAILS**
- **METHOD DETAILS**
  - Serum RBD Enzyme-linked immunosorbent assay (ELISA)
  - Serum ELISA analysis
  - SARS-CoV-2 and SARS-CoV pseudovirus neutralization assay
  - Blood sample processing
  - Cell staining and sorting
  - 5′ scRNA-seq library generation
  - scRNA-seq library sequencing
  - Ab production
  - IgA dimer purification through size exclusion chromatography
  - mAb ELISA testing
  - Neutralization activity of mAbs against authentic SARS-CoV-2
  - Protein expression and purification
  - Cryo-EM sample preparation
  - Cryo-EM data collection and processing
  - Cryo-EM Structure Modeling and Refinement

  - BG4-25-RBD X-ray crystallography experiments
  - Structural Analyses
  - Surface Plasmon Resonance (SPR) binding experiments
  - SARS-CoV-2 mutant RBD and sarbecovirus RBD ELISA binding assay
  - SARS-CoV-2 mutant pseudotyped reporter virus and mutant pseudotyped virus neutralization assay
  - mAb resistance selection experiments
- **QUANTIFICATION AND STATISTICAL ANALYSIS**
  - scRNA-seq analysis
  - Ab Repertoire Analysis
  - Mutational analysis of VH3-53/3-66 mAbs

AUTHOR CONTRIBUTIONS

J.F.S., C.O.B., B.E., D.G., P.J.B., J.D., A.R., D.H., and R.J.X. conceived the study and analyzed data. A.E.W., L.A.C., R.J.X., D.H., and J.D. established

and orchestrated the patient cohort. J.F.S. established and performed cell staining and sorting, B.E. performed computational analysis with guidance from A.R. and B.E. J.F.S. analyzed repertoire and transcriptome data with guidance from A.R. J.F.S. and A.H. performed mAb cloning, production, purification, and binding characterization. C.O.B. performed protein characterization and crystallographic and cryo-EM studies and analyzed structures. T.D., D.P., O.R.-R., and A.R. developed and performed scRNA-seq library preparation and coordinated single-cell RNA-seq. J.F.S., E.B., S.P., and B.T. performed patient sample processing. K.H.T. purified proteins. J.R.K. and A.A.C. performed and analyzed ELISAs. J.R.K. performed SPR binding and polyreactivity assays. M.A.D. and X.G. assisted with size exclusion chromatography. P.N.G., F.M., Y.W., T.H., F.G., S.Z., D.H., M.S.S., and P.D.B. developed and performed *in vitro* neutralization assays. A.P.W. analyzed mAb sequences. T.T. and N.R.L. conceived and designed ACE2-CH3 protein purification. J.F.S., C.O.B., B.E., J.D., A.R., P.J.B., and R.J.X. wrote the paper with contributions from other authors.

DECLARATION OF INTERESTS

REFERENCES

Adams, P.D., Afonine, P.V., Bunkóczi, G., Chen, V.B., Davis, I.W., Echols, N., Headd, J.J., Hung, L.W., Kapral, G.J., Grosse-Kunstleve, R.W., et al. (2010). PHENIX: a comprehensive Python-based system for macromolecular structure solution. Acta Crystallogr. D Biol. Crystallogr. 66, 213–221.

Barnes, C.O., Jette, C.A., Abernathy, M.E., Dam, K.A., Esswein, S.R., Gristick, H.B., Malyutin, A.G., Sharaf, N.G., Huey-Tubman, K.E., Lee, Y.E., et al. (2020a). SARS-CoV-2 neutralizing antibody structures inform therapeutic strategies. Nature 588, 682–687.

Barnes, C.O., West, A.P., Jr., Huey-Tubman, K.E., Hoffmann, M.A.G., Sharaf, N.G., Hoffman, P.R., Koranda, N., Gristick, H.B., Gaebler, C., Muecksch, F., et al. (2020b). Structures of Human Antibodies Bound to SARS-CoV-2 Spike Reveal Common Epitopes and Recurrent Features of Antibodies. Cell 182, 828–842.e16.

Bournazos, S., Gupta, A., and Ravetch, J.V. (2020). The role of IgG Fc receptors in antibody-dependent enhancement. Nat. Rev. Immunol. 20, 633–643.

Butler, A., Hoffman, P., Smibert, P., Papalexi, E., and Satija, R. (2018). Integrating single-cell transcriptomic data across different conditions, technologies, and species. Nat. Biotechnol. 36, 411–420.

Cao, Y., Su, B., Guo, X., Sun, W., Deng, Y., Bao, L., Zhu, Q., Zhang, X., Zheng, Y., Geng, C., et al. (2020). Potent neutralizing antibodies against SARS-CoV-2 identified by high-throughput single-cell sequencing of convalescent patients' B cells. Cell 182, 73–84.e16.

Chao, A., Gotelli, N.J., Hsieh, T.C., Sander, E.L., Ma, K.H., Colwell, R.K., and Ellison, A.M. (2014). Rarefaction and extrapolation with Hill numbers: a framework for sampling and estimation in species diversity studies. Ecol. Monogr. 84, 45–67.

Chao, A., Hsieh, T.C., Chazdon, R.L., Colwell, R.K., and Gotelli, N.J. (2015). Unveiling the species-rank abundance distribution by generalizing the Good-Turing sample coverage theory. Ecology 96, 1189–1201.

Chen, V.B., Arendall, W.B., 3rd, Headd, J.J., Keedy, D.A., Immormino, R.M., Kapral, G.J., Murray, L.W., Richardson, J.S., and Richardson, D.C. (2010). MolProbity: all-atom structure validation for macromolecular crystallography. Acta Crystallogr. D Biol. Crystallogr. 66, 12–21.

Chen, F., Tzarum, N., Wilson, I.A., and Law, M. (2019). V$_H$1-69 antiviral broadly neutralizing antibodies: genetics, structures, and relevance to rational vaccine design. Curr. Opin. Virol. 34, 149–159.

Cohen, A.A., Gnanapragasam, P.N.P., Lee, Y.E., Hoffman, P.R., Ou, S., Kakutani, L.M., Keeffe, J.R., Wu, H.-J., Howarth, M., West, A.P., et al. (2021). Mosaic nanoparticles elicit cross-reactive immune responses to zoonotic coronaviruses in mice. Science 371, 735–741.

Corti, D., and Lanzavecchia, A. (2013). Broadly neutralizing antiviral antibodies. Annu. Rev. Immunol. 31, 705–742.

Corti, D., Zhao, J., Pedotti, M., Simonelli, L., Agnihothram, S., Fett, C., Fernandez-Rodriguez, B., Foglierini, M., Agatic, G., Vanzetta, F., et al. (2015). Prophylactic and postexposure efficacy of a potent human monoclonal antibody against MERS coronavirus. Proc. Natl. Acad. Sci. USA 112, 10473–10478.

Crawford, K.H.D., Dingens, A.S., Eguia, R., Wolf, C.R., Wilcox, N., Logue, J.K., Shuey, K., Casto, A.M., Fiala, B., Wrenn, S., et al. (2020a). Dynamics of neutralizing antibody titers in the months after SARS-CoV-2 infection. J. Infect. Dis. Published online September 30, 2020. https://doi.org/10.1093/infdis/jiaa618.

Crawford, K.H.D., Eguia, R., Dingens, A.S., Loes, A.N., Malone, K.D., Wolf, C.R., Chu, H.Y., Tortorici, M.A., Veesler, D., Murphy, M., et al. (2020b). Protocol and Reagents for Pseudotyping Lentiviral Particles with SARS-CoV-2 Spike Protein for Neutralization Assays. Viruses 12, 513.

Davies, N.G., Abbott, S., Barnard, R.C., Jarvis, C.I., Kucharski, A.J., Munday, J., Pearson, C.A.B., Russell, T.W., Tully, D.C., Washburne, A.D., et al. (2021). Estimated transmissibility and severity of novel SARS-CoV-2 Variant of Concern 202012/01 in England. medRxiv. https://doi.org/10.1101/2020.12.24.20248822.

de Wit, E., van Doremalen, N., Falzarano, D., and Munster, V.J. (2016). SARS and MERS: recent insights into emerging coronaviruses. Nat. Rev. Microbiol. 14, 523–534.

Diskin, R., Klein, F., Horwitz, J.A., Halper-Stromberg, A., Sather, D.N., Marcovecchio, P.M., Lee, T., West, A.P., Jr., Gao, H., Seaman, M.S., et al. (2013). Restricting HIV-1 pathways for escape using rationally designed anti-HIV-1 antibodies. J. Exp. Med. 210, 1235–1249.

Dunbar, J., Krawczyk, K., Leem, J., Baker, T., Fuchs, A., Georges, G., Shi, J., and Deane, C.M. (2014). SAbDab: the structural antibody database. Nucleic Acids Res. 42, D1140–D1146.

Elbe, S., and Buckland-Merrett, G. (2017). Data, disease and diplomacy: GISAID's innovative contribution to global health. Glob. Chall. 1, 33–46.

Ellebedy, A.H., Jackson, K.J., Kissick, H.T., Nakaya, H.I., Davis, C.W., Roskin, K.M., McElroy, A.K., Oshansky, C.M., Elbein, R., Thomas, S., et al. (2016). Defining antigen-specific plasmablast and memory B cell subsets in human blood after viral infection or vaccination. Nat. Immunol. 17, 1226–1234.

Emsley, P., Lohkamp, B., Scott, W.G., and Cowtan, K. (2010). Features and development of Coot. Acta Crystallogr. D Biol. Crystallogr. 66, 486–501.

Goddard, T.D., Huang, C.C., Meng, E.C., Pettersen, E.F., Couch, G.S., Morris, J.H., and Ferrin, T.E. (2018). UCSF ChimeraX: Meeting modern challenges in visualization and analysis. Protein Sci. 27, 14–25.

Greaney, A.J., Starr, T.N., Gilchuk, P., Zost, S.J., Binshtein, E., Loes, A.N., Hilton, S.K., Huddleston, J., Eguia, R., Crawford, K.H.D., et al. (2021). Complete Mapping of Mutations to the SARS-CoV-2 Spike Receptor-Binding Domain that Escape Antibody Recognition. Cell Host Microbe. 29, 44–57.

Gristick, H.B., von Boehmer, L., West, A.P., Jr., Schamber, M., Gazumyan, A., Golijanin, J., Seaman, M.S., Fätkenheuer, G., Klein, F., Nussenzweig, M.C., and Bjorkman, P.J. (2016). Natively glycosylated HIV-1 Env structure reveals

new mode for antibody recognition of the CD4-binding site. Nat. Struct. Mol. Biol. 23, 906–915.

Gupta, N.T., Vander Heiden, J.A., Uduman, M., Gadala-Maria, D., Yaari, G., and Kleinstein, S.H. (2015). Change-O: a toolkit for analyzing large-scale B cell immunoglobulin repertoire sequencing data. Bioinformatics 31, 3356–3358.

Guthmiller, J.J., Lan, L.Y., Fernández-Quintero, M.L., Han, J., Utset, H.A., Bitar, D.J., Hamel, N.J., Stovicek, O., Li, L., Tepora, M., et al. (2020). Polyreactive Broadly Neutralizing B cells Are Selected to Provide Defense against Pandemic Threat Influenza Viruses. Immunity 53, 1230–1244.e5.

Hansen, J., Baum, A., Pascal, K.E., Russo, V., Giordano, S., Wloga, E., Fulton, B.O., Yan, Y., Koon, K., Patel, K., et al. (2020). Studies in humanized mice and convalescent humans yield a SARS-CoV-2 antibody cocktail. Science 369, 1010–1014.

Hill, M.O. (1973). Diversity and Evenness: A Unifying Notation and Its Consequences. Ecology 54, 427–432.

Horns, F., Dekker, C.L., and Quake, S.R. (2020). Memory B Cell Activation, Broad Anti-influenza Antibodies, and Bystander Activation Revealed by Single-Cell Transcriptomics. Cell Rep. 30, 905–913.e6.

Horwitz, J.A., Halper-Stromberg, A., Mouquet, H., Gitlin, A.D., Tretiakova, A., Eisenreich, T.R., Malbec, M., Gravemann, S., Billerbeck, E., Dorner, M., et al. (2013). HIV-1 suppression and durable control by combining single broadly neutralizing antibodies and antiretroviral drugs in humanized mice. Proc. Natl. Acad. Sci. USA 110, 16538–16543.

Hötzel, I., Theil, F.P., Bernstein, L.J., Prabhu, S., Deng, R., Quintana, L., Lutman, J., Sibia, R., Chan, P., Bumbaca, D., et al. (2012). A strategy for risk mitigation of antibodies with fast clearance. MAbs 4, 753–760.

Hsieh, C.L., Goldsmith, J.A., Schaub, J.M., DiVenere, A.M., Kuo, H.C., Javanmardi, K., Le, K.C., Wrapp, D., Lee, A.G., Liu, Y., et al. (2020). Structure-based design of prefusion-stabilized SARS-CoV-2 spikes. Science 369, 1501–1505.

Hurlburt, N.K., Seydoux, E., Wan, Y.H., Edara, V.V., Stuart, A.B., Feng, J., Suthar, M.S., McGuire, A.T., Stamatatos, L., and Pancera, M. (2020). Structural basis for potent neutralization of SARS-CoV-2 and role of antibody affinity maturation. Nat. Commun. 11, 5413.

Izawa, K., Martin, E., Soudais, C., Bruneau, J., Boutboul, D., Rodriguez, R., Lenoir, C., Hislop, A.D., Besson, C., Touzot, F., et al. (2017). Inherited CD70 deficiency in humans reveals a critical role for the CD70-CD27 pathway in immunity to Epstein-Barr virus infection. J. Exp. Med. 214, 73–89.

Johnson, W.E., Li, C., and Rabinovic, A. (2007). Adjusting batch effects in microarray expression data using empirical Bayes methods. Biostatistics 8, 118–127.

Kabsch, W. (2010). XDS. Acta Crystallogr. D Biol. Crystallogr. 66, 125–132.

Katoh, K., Rozewicki, J., and Yamada, K.D. (2019). MAFFT online service: multiple sequence alignment, interactive sequence choice and visualization. Brief. Bioinform. 20, 1160–1166.

Klein, J.S., and Bjorkman, P.J. (2010). Few and far between: how HIV may be evading antibody avidity. PLoS Pathog. 6, e1000908.

Kremmidiotis, G., and Zola, H. (1995). Changes in CD44 expression during B cell differentiation in the human tonsil. Cell. Immunol. 161, 147–157.

Krissinel, E., and Henrick, K. (2007). Inference of macromolecular assemblies from crystalline state. J. Mol. Biol. 372, 774–797.

Kulkarni, P.S., Hurwitz, J.L., Simões, E.A.F., and Piedra, P.A. (2018). Establishing Correlates of Protection for Vaccine Development: Considerations for the Respiratory Syncytial Virus Vaccine Field. Viral Immunol. 31, 195–203.

Kyte, J., and Doolittle, R.F. (1982). A simple method for displaying the hydropathic character of a protein. J. Mol. Biol. 157, 105–132.

Lam, J.H., and Baumgarth, N. (2019). The Multifaceted B Cell Response to Influenza Virus. J. Immunol. 202, 351–359.

Lefranc, M.P., Giudicelli, V., Duroux, P., Jabado-Michaloud, J., Folch, G., Aouinti, S., Carillon, E., Duvergey, H., Houles, A., Paysan-Lafosse, T., et al. (2015). IMGT®, the international ImMunoGeneTics information system® 25 years on. Nucleic Acids Res. 43, D413–D422.

Leyendeckers, H., Odendahl, M., Löhndorf, A., Irsch, J., Spangfort, M., Miltenyi, S., Hunzelmann, N., Assenmacher, M., Radbruch, A., and Schmitz, J. (1999). Correlation analysis between frequencies of circulating antigen-specific IgG-bearing memory B cells and serum titers of antigen-specific IgG. Eur. J. Immunol. 29, 1406–1417.

Li, W., Moore, M.J., Vasilieva, N., Sui, J., Wong, S.K., Berne, M.A., Somasundaran, M., Sullivan, J.L., Luzuriaga, K., Greenough, T.C., et al. (2003). Angiotensin-converting enzyme 2 is a functional receptor for the SARS coronavirus. Nature 426, 450–454.

Li, B., Gould, J., Yang, Y., Sarkizova, S., Tabaka, M., Ashenberg, O., Rosen, Y., Slyper, M., Kowalczyk, M.S., Villani, A.C., et al. (2020). Cumulus provides cloud-based data analysis for large-scale single-cell and single-nucleus RNA-seq. Nat. Methods 17, 793–798.

Liu, Y., Liu, J., Xia, H., Zhang, X., Fontes-Garfias, C.R., Swanson, K.A., Cai, H., Sarkar, R., Chen, W., Cutler, M., et al. (2021). Neutralizing Activity of BNT162b2-Elicited Serum - Preliminary Report. N. Engl. J. Med. Published online February 17, 2021. https://doi.org/10.1056/NEJMc2102017.

Lv, Z., Deng, Y.Q., Ye, Q., Cao, L., Sun, C.Y., Fan, C., Huang, W., Sun, S., Sun, Y., Zhu, L., et al. (2020). Structural basis for neutralization of SARS-CoV-2 and SARS-CoV by a potent therapeutic antibody. Science 369, 1505–1509.

Mastronarde, D.N. (2005). Automated electron microscope tomography using robust prediction of specimen movements. J. Struct. Biol. 152, 36–51.

Mathew, N.R., Jayanthan, J.K., Smirnov, I., Robinson, J.L., Axelsson, H., Nakka, S.S., Emmanouilidi, A., Czarnewski, P., Yewdell, W.T., Lebrero-Fernández, C., et al. (2020). Single cell BCR and transcriptome analysis after respiratory virus infection reveals spatiotemporal dynamics of antigen-specific B cell responses. bioRxiv. https://doi.org/10.1101/2020.08.24.264069.

McCoy, A.J., Grosse-Kunstleve, R.W., Adams, P.D., Winn, M.D., Storoni, L.C., and Read, R.J. (2007). Phaser crystallographic software. J. Appl. Cryst. 40, 658–674.

Moir, S., Ho, J., Malaspina, A., Wang, W., DiPoto, A.C., O'Shea, M.A., Roby, G., Kottilil, S., Arthos, J., Proschan, M.A., et al. (2008). Evidence for HIV-associated B cell exhaustion in a dysfunctional memory B cell compartment in HIV-infected viremic individuals. J. Exp. Med. 205, 1797–1805.

Moore, D.S. (1985). Amino acid and peptide net charges: A simple calculational procedure. Biochem. Educ. 13, 10–11.

Moroney, J.B., Vasudev, A., Pertsemlidis, A., Zan, H., and Casali, P. (2020). Integrative transcriptome and chromatin landscape analysis reveals distinct epigenetic regulations in human memory B cells. Nat. Commun. 11, 5435.

Mouquet, H., Scheid, J.F., Zoller, M.J., Krogsgaard, M., Ott, R.G., Shukair, S., Artyomov, M.N., Pietzsch, J., Connors, M., Pereyra, F., et al. (2010). Polyreactivity increases the apparent affinity of anti-HIV antibodies by heteroligation. Nature 467, 591–595.

Muecksch, F., Weisblum, Y., Barnes, C.O., Schmidt, F., Schaefer-Babajew, D., Lorenzi, J.C.C., Flyak, A.I., DeLaitsch, A.T., Huey-Tubman, K.E., Hou, S., et al. (2021). Development of potency, breadth and resilience to viral escape mutations in SARS-CoV-2 neutralizing antibodies. bioRxiv. https://doi.org/10.1101/2021.03.07.434227.

Muehlinghaus, G., Cigliano, L., Huehn, S., Peddinghaus, A., Leyendeckers, H., Hauser, A.E., Hiepe, F., Radbruch, A., Arce, S., and Manz, R.A. (2005). Regulation of CXCR3 and CXCR4 expression during terminal differentiation of memory B cells into plasma cells. Blood 105, 3965–3971.

Nagasawa, T., Nakajima, T., Tachibana, K., Iizasa, H., Bleul, C.C., Yoshie, O., Matsushima, K., Yoshida, N., Springer, T.A., and Kishimoto, T. (1996). Molecular cloning and characterization of a murine pre-B-cell growth-stimulating factor/stromal cell-derived factor 1 receptor, a murine homolog of the human immunodeficiency virus 1 entry coreceptor fusin. Proc. Natl. Acad. Sci. USA 93, 14726–14729.

Neu, K.E., Guthmiller, J.J., Huang, M., La, J., Vieira, M.C., Kim, K., Zheng, N.Y., Cortese, M., Tepora, M.E., Hamel, N.J., et al. (2019). Spec-seq unveils transcriptional subpopulations of antibody-secreting cells following influenza vaccination. J. Clin. Invest. 129, 93–105.

Nie, Y., Waite, J., Brewer, F., Sunshine, M.J., Littman, D.R., and Zou, Y.R. (2004). The role of CXCR4 in maintaining peripheral B cell compartments and humoral immunity. J. Exp. Med. *200*, 1145–1156.

Nouri, N., and Kleinstein, S.H. (2018). A spectral clustering-based method for identifying clones from high-throughput B cell repertoire sequencing data. Bioinformatics *34*, i341–i349.

Pear, W.S., Nolan, G.P., Scott, M.L., and Baltimore, D. (1993). Production of high-titer helper-free retroviruses by transient transfection. Proc. Natl. Acad. Sci. U. S. A. *90*, 8392–8396.

Piccoli, L., Park, Y.-J., Tortorici, M.A., Czudnochowski, N., Walls, A.C., Beltramello, M., Silacci-Fregni, C., Pinto, D., Rosen, L.E., Bowen, J.E., et al. (2020). Mapping neutralizing and immunodominant sites on the SARS-CoV-2 spike receptor-binding domain by structure-guided high-resolution serology. Cell *183*, 1024–1042.e21.

Pinto, D., Park, Y.-J., Beltramello, M., Walls, A.C., Tortorici, M.A., Bianchi, S., Jaconi, S., Culap, K., Zatta, F., De Marco, A., et al. (2020). Cross-neutralization of SARS-CoV-2 by a human monoclonal SARS-CoV antibody. Nature *583*, 290–295.

Prabakaran, P., Gan, J., Feng, Y., Zhu, Z., Choudhry, V., Xiao, X., Ji, X., and Dimitrov, D.S. (2006). Structure of severe acute respiratory syndrome coronavirus receptor-binding domain complexed with neutralizing antibody. J. Biol. Chem. *281*, 15829–15836.

Prigent, J., Jarossay, A., Planchais, C., Eden, C., Dufloo, J., Kök, A., Lorin, V., Vratskikh, O., Couderc, T., Bruel, T., et al. (2018). Conformational Plasticity in Broadly Neutralizing HIV-1 Antibodies Triggers Polyreactivity. Cell Rep. *23*, 2568–2581.

Punjani, A., Rubinstein, J.L., Fleet, D.J., and Brubaker, M.A. (2017). cryoSPARC: algorithms for rapid unsupervised cryo-EM structure determination. Nat. Methods *14*, 290–296.

Robbiani, D.F., Gaebler, C., Muecksch, F., Lorenzi, J.C.C., Wang, Z., Cho, A., Agudelo, M., Barnes, C.O., Gazumyan, A., Finkin, S., et al. (2020). Convergent antibody responses to SARS-CoV-2 in convalescent individuals. Nature *584*, 437–442.

Rockx, B., Corti, D., Donaldson, E., Sheahan, T., Stadler, K., Lanzavecchia, A., and Baric, R. (2008). Structural basis for potent cross-neutralizing human monoclonal antibody protection against lethal human and zoonotic severe acute respiratory syndrome coronavirus challenge. J. Virol. *82*, 3220–3235.

Roy, V., Fischinger, S., Atyeo, C., Slein, M., Loos, C., Balazs, A., Luedemann, C., Astudillo, M.G., Yang, D., Wesemann, D.R., et al. (2020). SARS-CoV-2-specific ELISA development. J. Immunol. Methods *484-485*, 112832.

Rubelt, F., Sievert, V., Knaust, F., Diener, C., Lim, T.S., Skriner, K., Klipp, E., Reinhardt, R., Lehrach, H., and Konthur, Z. (2012). Onset of immune senescence defined by unbiased pyrosequencing of human immunoglobulin mRNA repertoires. PLoS ONE *7*, e49774.

Scheid, J.F., Mouquet, H., Feldhahn, N., Seaman, M.S., Velinzon, K., Pietzsch, J., Ott, R.G., Anthony, R.M., Zebroski, H., Hurley, A., et al. (2009). Broad diversity of neutralizing antibodies isolated from memory B cells in HIV-infected individuals. Nature *458*, 636–640.

Scheid, J.F., Mouquet, H., Ueberheide, B., Diskin, R., Klein, F., Oliveira, T.Y., Pietzsch, J., Fenyo, D., Abadir, A., Velinzon, K., et al. (2011). Sequence and structural convergence of broad and potent HIV antibodies that mimic CD4 binding. Science *333*, 1633–1637.

Schmidt, F., Weisblum, Y., Muecksch, F., Hoffmann, H.H., Michailidis, E., Lorenzi, J.C.C., Mendoza, P., Rutkowska, M., Bednarski, E., Gaebler, C., et al. (2020). Measuring SARS-CoV-2 neutralizing antibody activity using pseudotyped and chimeric viruses. J. Exp. Med. *217*, e20201181.

Shingai, M., Donau, O.K., Plishka, R.J., Buckler-White, A., Mascola, J.R., Nabel, G.J., Nason, M.C., Montefiori, D., Moldt, B., Poignard, P., et al. (2014). Passive transfer of modest titers of potent and broadly neutralizing anti-HIV monoclonal antibodies block SHIV infection in macaques. J. Exp. Med. *211*, 2061–2074.

Sievers, F., Wilm, A., Dineen, D., Gibson, T.J., Karplus, K., Li, W., Lopez, R., McWilliam, H., Remmert, M., Söding, J., et al. (2011). Fast, scalable generation of high-quality protein multiple sequence alignments using Clustal Omega. Mol. Syst. Biol. *7*, 539.

Sokal, A., Chappert, P., Barba-Spaeth, G., Roeser, A., Fourati, S., Azzaoui, I., Vandenberghe, A., Fernandez, I., Meola, A., Bouvier-Alias, M., et al. (2021). **Maturation and persistence of the anti-SARS-CoV-2 memory B cell response**. Cell *184*, 1201–1213.e14.

Stuart, T., Butler, A., Hoffman, P., Hafemeister, C., Papalexi, E., Mauck, W.M., 3rd, Hao, Y., Stoeckius, M., Smibert, P., and Satija, R. (2019). Comprehensive Integration of Single-Cell Data. Cell *177*, 1888–1902.

Sui, J., Li, W., Murakami, A., Tamin, A., Matthews, L.J., Wong, S.K., Moore, M.J., Tallarico, A.S., Olurinde, M., Choe, H., et al. (2004). Potent neutralization of severe acute respiratory syndrome (SARS) coronavirus by a human mAb to S1 protein that blocks receptor association. Proc. Natl. Acad. Sci. USA *101*, 2536–2541.

Tada, T., Fan, C., Chen, J.S., Kaur, R., Stapleford, K.A., Gristick, H., Dcosta, B.M., Wilen, C.B., Nimigean, C.M., and Landau, N.R. (2020). An ACE2 Microbody Containing a Single Immunoglobulin Fc Domain Is a Potent Inhibitor of SARS-CoV-2. Cell Rep. *33*, 108528.

Tada, T., Dcosta, B.M., Zhou, H., Vaill, A., Kazmierski, W., and Landau, N.R. (2021). Decreased neutralization of SARS-CoV-2 global variants by therapeutic anti-spike protein monoclonal antibodies. bioRxiv. https://doi.org/10.1101/2021.02.18.431897.

Tan, T.J.C., Yuan, M., Kuzelka, K., Padron, G.C., Beal, J.R., Chen, X., Wang, Y., Rivera-Cardona, J., Zhu, X., Stadtmueller, B.M., et al. (2021). Sequence signatures of two IGHV3-53/3-66 public clonotypes to SARS-CoV-2 receptor binding domain. bioRxiv. https://doi.org/10.1101/2021.01.26.428356.

Tang, X.C., Agnihothram, S.S., Jiao, Y., Stanhope, J., Graham, R.L., Peterson, E.C., Avnir, Y., Tallarico, A.S., Sheehan, J., Zhu, Q., et al. (2014). Identification of human neutralizing antibodies against MERS-CoV and their role in virus adaptive evolution. Proc. Natl. Acad. Sci. USA *111*, E2018–E2026.

Tegally, H., Wilkinson, E., Giovanetti, M., Iranzadeh, A., Fonseca, V., Giandhari, J., Doolabh, D., Pillay, S., San, E.J., Msomi, N., et al. (2020). Emergence and rapid spread of a new severe acute respiratory syndrome-related coronavirus 2 (SARS-CoV-2) lineage with multiple spike mutations in South Africa. medRxiv. https://doi.org/10.1101/2020.12.21.20248640.

Terwilliger, T.C., Adams, P.D., Afonine, P.V., and Sobolev, O.V. (2018). A fully automatic method yielding initial models from high-resolution cryo-electron microscopy maps. Nat. Methods *15*, 905–908.

Tian, X., Li, C., Huang, A., Xia, S., Lu, S., Shi, Z., Lu, L., Jiang, S., Yang, Z., Wu, Y., and Ying, T. (2020). Potent binding of 2019 novel coronavirus spike protein by a SARS coronavirus-specific human monoclonal antibody. Emerg. Microbes Infect. *9*, 382–385.

Tiller, T., Tsuiji, M., Yurasov, S., Velinzon, K., Nussenzweig, M.C., and Wardemann, H. (2007). Autoreactivity in human IgG+ memory B cells. Immunity *26*, 205–213.

Tiller, T., Meffre, E., Yurasov, S., Tsuiji, M., Nussenzweig, M.C., and Wardemann, H. (2008). Efficient generation of monoclonal antibodies from single human B cells by single cell RT-PCR and expression vector cloning. J. Immunol. Methods *329*, 112–124.

Tirosh, I., Izar, B., Prakadan, S.M., Wadsworth, M.H., 2nd, Treacy, D., Trombetta, J.J., Rotem, A., Rodman, C., Lian, C., Murphy, G., et al. (2016). Dissecting the multicellular ecosystem of metastatic melanoma by single-cell RNA-seq. Science *352*, 189–196.

Tortorici, M.A., Beltramello, M., Lempp, F.A., Pinto, D., Dang, H.V., Rosen, L.E., McCallum, M., Bowen, J., Minola, A., Jaconi, S., et al. (2020). Ultrapotent human antibodies protect against SARS-CoV-2 challenge via multiple mechanisms. Science *370*, 950–957.

Traag, V.A., Waltman, L., and van Eck, N.J. (2019). From Louvain to Leiden: guaranteeing well-connected communities. Sci. Rep. *9*, 5233.

Traggiai, E., Becker, S., Subbarao, K., Kolesnikova, L., Uematsu, Y., Gismondo, M.R., Murphy, B.R., Rappuoli, R., and Lanzavecchia, A. (2004). An efficient method to make human monoclonal antibodies from memory B cells: potent neutralization of SARS coronavirus. Nat. Med. *10*, 871–875.

van Gisbergen, K.P., Klarenbeek, P.L., Kragten, N.A., Unger, P.P., Nieuwenhuis, M.B., Wensveen, F.M., ten Brinke, A., Tak, P.P., Eldering, E., Nolte, M.A., and van Lier, R.A. (2011). The costimulatory molecule CD27 maintains clonally diverse CD8(+) T cell responses of low antigen affinity to protect against viral variants. Immunity *35*, 97–108.

Verschoor, C.P., Singh, P., Russell, M.L., Bowdish, D.M., Brewer, A., Cyr, L., Ward, B.J., and Loeb, M. (2015). Microneutralization assay titres correlate with protection against seasonal influenza H1N1 and H3N2 in children. PLoS ONE *10*, e0131531.

Victora, G.D., and Nussenzweig, M.C. (2012). Germinal centers. Annu. Rev. Immunol. *30*, 429–457.

Waickman, A.T., Gromowski, G.D., Rutvisuttinunt, W., Li, T., Siegfried, H., Victor, K., Kuklis, C., Gomootsukavadee, M., McCracken, M.K., Gabriel, B., et al. (2020). Transcriptional and clonal characterization of B cell plasmablast diversity following primary and secondary natural DENV infection. EBioMedicine *54*, 102733.

Wang, Z., Lorenzi, J.C.C., Muecksch, F., Finkin, S., Viant, C., Gaebler, C., Cipolla, M., Hoffman, H.H., Oliveira, T.Y., Oren, D.A., et al. (2020). Enhanced SARS-CoV-2 Neutralization by Secretory IgA in vitro. bioRxiv. https://doi.org/10.1101/2020.09.09.288555.

Wang, Z., Schmidt, F., Weisblum, Y., Muecksch, F., Barnes, C.O., Finkin, S., Schaefer-Babajew, D., Cipolla, M., Gaebler, C., Lieberman, J.A., et al. (2021). mRNA vaccine-elicited antibodies to SARS-CoV-2 and circulating variants. Nature *592*, 616–622.

Wardemann, H., Yurasov, S., Schaefer, A., Young, J.W., Meffre, E., and Nussenzweig, M.C. (2003). Predominant autoantibody production by early human B cell precursors. Science *301*, 1374–1377.

Weisblum, Y., Schmidt, F., Zhang, F., DaSilva, J., Poston, D., Lorenzi, J.C., Muecksch, F., Rutkowska, M., Hoffmann, H.H., Michailidis, E., et al. (2020). Escape from neutralizing antibodies by SARS-CoV-2 spike protein variants. eLife *9*, e61312.

West, A.P., Jr., Galimidi, R.P., Foglesong, C.P., Gnanapragasam, P.N., Klein, J.S., and Bjorkman, P.J. (2010). Evaluation of CD4-CD4i antibody architectures yields potent, broadly cross-reactive anti-human immunodeficiency virus reagents. J. Virol. *84*, 261–269.

West, A.P., Jr., Scharf, L., Horwitz, J., Klein, F., Nussenzweig, M.C., and Bjorkman, P.J. (2013). Computational analysis of anti-HIV-1 antibody neutralization panel data to identify potential functional epitope residues. Proc. Natl. Acad. Sci. USA *110*, 10598–10603.

Wibmer, C.K., Ayres, F., Hermanus, T., Madzivhandila, M., Kgagudi, P., Lambson, B.E., Vermeulen, M., van den Berg, K., Rossouw, T., Boswell, M., et al. (2021). SARS-CoV-2 501Y.V2 escapes neutralization by South African COVID-19 donor plasma. bioRxiv. https://doi.org/10.1101/2021.01.18.427166.

Winn, M.D., Ballard, C.C., Cowtan, K.D., Dodson, E.J., Emsley, P., Evans, P.R., Keegan, R.M., Krissinel, E.B., Leslie, A.G., McCoy, A., et al. (2011). Overview of the CCP4 suite and current developments. Acta Crystallogr. D Biol. Crystallogr. *67*, 235–242.

Wrapp, D., Wang, N., Corbett, K.S., Goldsmith, J.A., Hsieh, C.L., Abiona, O., Graham, B.S., and McLellan, J.S. (2020). Cryo-EM structure of the 2019-nCoV spike in the prefusion conformation. Science *367*, 1260–1263.

Wu, N.C., Yuan, M., Liu, H., Lee, C.D., Zhu, X., Bangaru, S., Torres, J.L., Caniels, T.G., Brouwer, P.J.M., van Gils, M.J., et al. (2020a). An Alternative Binding Mode of IGHV3-53 Antibodies to the SARS-CoV-2 Receptor Binding Domain. Cell Rep. *33*, 108274.

Wu, Y., Wang, F., Shen, C., Peng, W., Li, D., Zhao, C., Li, Z., Li, S., Bi, Y., Yang, Y., et al. (2020b). A noncompeting pair of human neutralizing antibodies block COVID-19 virus binding to its receptor ACE2. Science *368*, 1274–1278.

Wu, K., Werner, A.P., Koch, M., Choi, A., Narayanan, E., Stewart-Jones, G.B.E., Colpitts, T., Bennett, H., Boyoglu-Barnum, S., Shi, W., et al. (2021). Serum Neutralizing Activity Elicited by mRNA-1273 Vaccine - Preliminary Report. N. Engl. J. Med. Published online February 17, 2021. https://doi.org/10.1056/NEJMc2102179.

Yaari, G., Uduman, M., and Kleinstein, S.H. (2012). Quantifying selection in high-throughput Immunoglobulin sequencing data sets. Nucleic Acids Res. *40*, e134.

Yan, R., Zhang, Y., Li, Y., Xia, L., Guo, Y., and Zhou, Q. (2020). Structural basis for the recognition of SARS-CoV-2 by full-length human ACE2. Science *367*, 1444–1448.

Yuan, M., Liu, H., Wu, N.C., Lee, C.D., Zhu, X., Zhao, F., Huang, D., Yu, W., Hua, Y., Tien, H., et al. (2020). Structural basis of a shared antibody response to SARS-CoV-2. Science *369*, 1119–1123.

Zuccarino-Catania, G.V., Sadanand, S., Weisel, F.J., Tomayko, M.M., Meng, H., Kleinstein, S.H., Good-Jacobson, K.L., and Shlomchik, M.J. (2014). CD80 and PD-L2 define functionally distinct memory B cell subsets that are independent of antibody isotype. Nat. Immunol. *15*, 631–637.

STAR★METHODS

KEY RESOURCES TABLE

REAGENT or RESOURCE	SOURCE	IDENTIFIER
Antibodies		
HRP Conjugated anti-Human IgG	Bethyl Laboratory	Cat#A80-104P; RRID: AB_67064
HRP Conjugated anti-Human IgM	Bethyl Laboratory	Cat#A80-100P; RRID: AB_67082
CR3022 IgG1	Absolute Antibody	Cat#Ab01680-10.0
CR3022 IgM	Absolute Antibody	Cat#Ab01680-15.0
TotalSeq-C0251 anti-Human Hashtag 1 Antibody	Biolegend	Cat#394661; RRID: AB_2801031
TotalSeq-C0252 anti-Human Hashtag 2 Antibody	Biolegend	Cat#394663; RRID: AB_2801032
TotalSeq-C0253 anti-Human Hashtag 3 Antibody	Biolegend	Cat#394665; RRID: AB_2801033
TotalSeq-C0254 anti-Human Hashtag 4 Antibody	Biolegend	Cat#394667; RRID: AB_2801034
TotalSeq-C0256 anti-Human Hashtag 6 Antibody	Biolegend	Cat#394671; RRID: AB_2820042
TotalSeq-C0257 anti-Human Hashtag 7 Antibody	Biolegend	Cat#394673; RRID: AB_2820043
TotalSeq-C0258 anti-Human Hashtag 8 Antibody	Biolegend	Cat#394675; RRID: AB_2820044
TotalSeq-C0260 anti-Human Hashtag 10 Antibody	Biolegend	Cat#394679; RRID: AB_2820046
FITC Mouse anti-Human CD19 Antibody	BD	Cat#340964; RRID: AB_400446
mGO53	Wardemann et al., 2003	https://doi.org/10.1126/science.1086907
JB40	Wardemann et al., 2003	https://doi.org/10.1126/science.1086907
ED38	Wardemann et al., 2003	https://doi.org/10.1126/science.1086907
HRP Conjugated Goat anti-Human Kappa Light Chain Antibody	Bio-Rad	Cat#STAR127P; RRID: AB_1102710
HRP Conjugated Goat anti-Human Lambda Light Chain Antibody	Bio-Rad	Cat#STAR129P; RRID: AB_1102721
Anti-MERS-CoV Spike Protein (3B12)	Absolute Antibody	Cat#Ab01673-10.0
Anti-SARS-CoV S Glycoprotein (S227)	Absolute Antibody	Cat#Ab00263-10.0
SARS-CoV/SARS-CoV-2 Nucleocapsid Antibody, Mouse mAb	SinoBiological	Cat#40143-MM08; RRID: AB_2827978
Alexa Fluor 488 AffiniPure Goat Anti-Mouse IgG (H+L)	JacksonImmuno	Cat#115-545-003 RRID: AB_2338840
Goat Anti-Human IgG(H+L)-HRP	SouthernBiotech	Cat#2015-05; RRID: AB_2795588
Goat Anti-Human IgG-HRP	SouthernBiotech	Cat#2040-05; RRID: AB_2795644
Goat Anti-Human IgG(H+L)-HRP	Genscript	Cat#A00166
Bacterial and virus strains		
SARS-CoV-2 isolate from USA-WA1/2020	BEI Resources	N/A
SARS-CoV-2 pseudotyped reporter virus	Robbiani et al., 2020	http://www.nature.com/articles/s41586-020-2456-9
SARS-CoV pseudotyped reporter virus	Robbiani et al., 2020	http://www.nature.com/articles/s41586-020-2456-9
WIV1-CoV pseudotyped reporter virus	Cohen et al., 2021	https://www.sciencemag.org/lookup/doi/10.1126/science.abf6840

(Continued on next page)

Continued

REAGENT or RESOURCE	SOURCE	IDENTIFIER
SCH014-CoV pseudotyped reporter virus	Cohen et al., 2021	https://www.sciencemag.org/lookup/doi/10.1126/science.abf6840
SARS-CoV-2 B.1.1.7 pseudotyped reporter virus	Bjorkman lab (this paper)	N/A
SARS-CoV-2 B.1.351 pseudotyped reporter virus	Bjorkman lab (this paper)	N/A
E. coli DH5 Alpha	Zymo Research	Cat#T3009
rVSV/SARS-CoV-2/GFP$_{1D7}$	Schmidt et al., 2020	https://rupress.org/jem/article/doi/10.1084/jem.20201181/151961/Measuring-SARSCoV2-neutralizing-antibody-activity
rVSV/SARS-CoV-2/GFP$_{2E1}$	Schmidt et al., 2020	https://rupress.org/jem/article/doi/10.1084/jem.20201181/151961/Measuring-SARSCoV2-neutralizing-antibody-activity
2E1 L441P	This paper	N/A
2E1 G339R (2)	This paper	N/A
2E1 G339R (10)	This paper	N/A
Chemicals, peptides, and recombinant proteins		
BupH Carbonate-bicarbonate Buffer Packs	Thermo Fisher	Cat#28382
Tween 20	Sigma	Cat#P9416
Pierce TMB Substrate Kit	Thermo Fisher	Cat#34021
Ficoll-Paque PLUS	Cytiva	Cat#17144003
UltraPure 0.5M EDTA, pH 8.0	Thermo Fisher	Cat#15575020
Cell Staining Buffer	Biolegend	Cat#420201
Human TruStain FcX Fc	Biolegend	Cat#422302
APC Streptavidin	Biolegend	Cat#405207
Invitrogen PureLink HiPure Plasmid Maxiprep Kit	Thermo Fisher	Cat#K210007
GIBCO Expi293 Expression Medium	Thermo Fisher	Cat#A1435101
GIBCO ExpiFectamine 293 Tranfection Kit	Thermo Fisher	Cat#A1452
GIBCO Opti-Plex Complexation Buffer	Thermo Fisher	Cat#A4096801
Peptide M Coupled Agarose Beads	Invivogen	Cat#gel-pdm-5
Protein G Sepharose 4 Fast Flow	Sigma	Cat#GE17-0618-02
Native Sample Buffer for Protein Gels	Bio-Rad	Cat#1610738
Precision Plus Protein Kaleidoscope Prestained Protein Standard	Bio-Rad	Cat#1610375
UltraPure Salmon Sperm DNA Solution	Thermo Fisher	Cat#15632011
Human Recombinant Insulin	Sigma	Cat#91077C
Lipopolysaccharides (LPS) from *E. coli* (O55:B5)	Sigma	Cat#L2637
HRP Substrate Kit	Bio-Rad	Cat#172-1064
Dulbecco's Modified Eagle Medium (DMEM)	GIBCO	Cat# 11960-044
Fetal bovine serum (FBS)	Sigma-Aldrich	Cat# F4135
Gentamicin solution	Sigma-Aldrich	Cat# G1397, CAS:1405-41-0
Blasticidin S HCl	GIBCO	Cat# A1113902, CAS:3513-03-9
LB Broth (Miller)	Sigma-Aldrich	Cat# L3522
Papain	Sigma-Aldrich	Cat# P3125; CAS:9001-73-4
BirA biotin-protein ligase standard reaction kit	Avidity	Cat# BirA500
Goat Serum, New Zealand origin	GIBCO	Cat# 16210-064
1-Step Ultra TMB-ELISA Substrate Solution	Thermo Scientific	Cat# 34029

(Continued on next page)

Continued

REAGENT or RESOURCE	SOURCE	IDENTIFIER
ACE2 microbody	Nathaniel Landau; Tada et al., 2020	https://linkinghub.elsevier.com/retrieve/pii/S2211124720315175
Baculovirus (BV) particles	Protein Expression Center, Caltech; Hötzel et al., 2012	http://www.tandfonline.com/doi/abs/10.4161/mabs.22189
FCS	Sigma	Cat#F0926
Gentamicin solution	Sigma-Aldrich	Cat#G1397. CAS:1405-41-0
Blasticidin S HCl	GIBCO	Cat#A1113902; CAS: 3513-03-9
KOD Xtreme Hot Start DNA Polymerase	Sigma	Cat#71975
SuperScript VILO Master Mix	Invitrogen	Cat#11755050
NucleoSpin 96 Virus Core Kit	Macherey-Nagel	Cat#740452
Critical commercial assays		
Luciferase Cell Culture Lysis 5X Reagent	Promega	Cat#E1531
Britelite plus Reporter Gene Assay System	PerkinElmer	Cat#6066769
Nano-Glo Luciferase Assay System	Promega	Cat#N1110
Supersignal ELISA Femto Substrate	ThermoFisher	Cat#37074
Deposited data		
Source codes for scRNA-seq and Ab repertoire analyses	This paper	https://github.com/EraslanBas/Sars_Cov2_Antibodies
Antibody sequences and scRNA-seq count matrices	This paper	Single Cell Portal of the Broad Institute (SARS-CoV-2 Antibodies, Accession #SCP1317; https://singlecell.broadinstitute.org/single_cell/study/SCP1317/sars-cov-2-antibodies)
Raw scRNA-seq files	This paper	DUOS (https://duos.broadinstitute.org/dataset_catalog) with the DUOS ID: DUOS-000125
Structure of the SARS-CoV-2 RBD in complex with neutralizing antibodies BG4-25 and CR3022	This paper	Protein Data Bank (PDB) Code: PDB 7M6D
Structure of the SARS-CoV-2 S 6P trimer in complex with the neutralizing antibody Fab fragment, BG10-19	This paper	PDB Code: PDB 7M6E Electron Microscopy Data Bank (EMD) Code: EMD 23693
Structure of the SARS-CoV-2 S 6P trimer in complex with the human neutralizing antibody Fab fragment, BG1-22	This paper	PDB Code: PDB 7M6F EMD Code: EMD 23694
Structure of the SARS-CoV-2 S 6P trimer in complex with the human neutralizing antibody Fab fragment, BG7-15	This paper	PDB Code: PDB 7M6G EMD Code: EMD 23695
Structure of the SARS-CoV-2 S 6P trimer in complex with the human neutralizing antibody Fab fragment, BG7-20	This paper	PDB Code: PDB 7M6H EMD Code: EMD 23696
Structure of the SARS-CoV-2 S 6P trimer in complex with the human neutralizing antibody Fab fragment, BG1-24	This paper	PDB Code: PDB 7M6I EMD Code: EMD 23697
Experimental models: Cell lines		
293/ACE2	Dr. Michael Farzan (Scripps Research Institute)	N/A
TZM.bl/ACE2	Dr. Michael Farzan (Scripps Research Institute)	N/A
293T/17	ATCC	CRL-11268
293T cells	Pear et al., 1993	Cat#CCLV-RIE 1018; RRID: CVCL_0063
Vero-TMPRSS2	Laboratory of Nir Hacohen	N/A

(*Continued on next page*)

Continued

REAGENT or RESOURCE	SOURCE	IDENTIFIER
HEK293T$_{Ace2}$	Robbiani et al., 2020	http://www.nature.com/articles/s41586-020-2456-9
HEK293-ACE2	Dr. Jesse Bloom (Fred Hutchinson Cancer Research Center)	N/A
GIBCO Expi293F Cells	Thermo Fisher	Cat# A14527; RRID: CVCL_D615
293TAce2 cells cl.22	Schmidt et al., 2020	https://rupress.org/jem/article/doi/10.1084/jem.20201181/151961/Measuring-SARSCoV2-neutralizing-antibody-activity
HT1080Ace2 cells cl.14	Schmidt et al., 2020	https://rupress.org/jem/article/doi/10.1084/jem.20201181/151961/Measuring-SARSCoV2-neutralizing-antibody-activity
Experimental models: Organisms/strains		
One Shot Mach1 Chemically Competent *E. coli*	Thermo Fisher	Cat#C862003
Oligonucleotides		
Primers for cloning heavy chain VDJ regions into IgA expression plasmids	Wang et al., 2020	http://biorxiv.org/lookup/doi/10.1101/2020.09.09.288555
Primers for cloning heavy chain VDJ regions into IgG expression plasmids	Wardemann et al., 2003	https://www.sciencemag.org/lookup/doi/10.1126/science.1086907
Recombinant DNA		
IgG, IgK and IgL expression plasmids	Dr. Michel Nussenzweig, Rockefeller University	N/A
IgA1 expression plasmid	Invivogen	pFUSEss-CHIg-hA1
IgA2 expression plasmid	Invivogen	pFUSEss-CHIg-hA2(m1)
HIV-1 SG3ΔEnv	NIH AIDS Reagent Program	ARP-11051
pCMV R8.2	Dr. Barney Graham (NIH Vaccine Research Center)	N/A
pHR' CMV-Luc	Dr. Barney Graham (NIH Vaccine Research Center)	N/A
p-SARS-CoV-2 Spike ΔCT	Dr. Dan Barouch (BIDMC)	N/A
p-SARS-CoV-2 Spike G614D	Dr. Barney Graham (NIH Vaccine Research Center)	N/A
SCIB-ACE2 (H374N &H378N)	Robbiani et al., 2020	http://www.nature.com/articles/s41586-020-2456-9
pNL4-3DEnv-nanoluc	Robbiani et al., 2020	http://www.nature.com/articles/s41586-020-2456-9
pSARS-CoV2-S$_{trunc}$	Robbiani et al., 2020	http://www.nature.com/articles/s41586-020-2456-9
pSARS-CoV-S$_{trunc}$ (pCR3.1_GA_S2_Wuhan)	Robbiani et al., 2020	http://www.nature.com/articles/s41586-020-2456-9
pHAGE-CMV-Luc-2-IRES-ZsGreen-W-1270	Dr. Jesse Bloom (Fred Hutchinson Cancer Research Center)	N/A
HDM_Hgpm2	Dr. Jesse Bloom (Fred Hutchinson Cancer Research Center)	N/A
pRC_CMV_Rev1b	Dr. Jesse Bloom (Fred Hutchinson Cancer Research Center)	N/A
HDM_tat1b	Dr. Jesse Bloom (Fred Hutchinson Cancer Research Center)	N/A
pSARS-CoV2 D614G (HDM_Spike_del21_D614G)	Dr. Jesse Bloom (Fred Hutchinson Cancer Research Center)	N/A
pSARS-CoV1	Dr. Paul Bieniasz (The Rockefeller University)	N/A

(Continued on next page)

Continued

REAGENT or RESOURCE	SOURCE	IDENTIFIER
pTwist-CMV BetaGlobin-SARS-CoV-2 S (residues 16-1206)	Barnes et al., 2020b	https://doi.org/10.1016/j.cell.2020.06.025
pTwist-CMV BetaGlobin-SARS-CoV S (residues 12-1193)	Barnes et al., 2020b	https://doi.org/10.1016/j.cell.2020.06.025
pTwist-CMV BetaGlobin-MERS-CoV S (residues 19-1294)	Barnes et al., 2020b	https://doi.org/10.1016/j.cell.2020.06.025
pTwist-CMV BetaGlobin-SARS-CoV-2 S RBD (residues 331-524)	Barnes et al., 2020b	https://doi.org/10.1016/j.cell.2020.06.025
pTwist-CMV BetaGlobin-SARS-CoV S RBD (residues 318-510)	Barnes et al., 2020b	https://doi.org/10.1016/j.cell.2020.06.025
pTwist-CMV BetaGlobin-MERS-CoV S RBD (residues 367-588)	Barnes et al., 2020b	https://doi.org/10.1016/j.cell.2020.06.025
pCAGGS-SARS-CoV-2 RBD 6xHisTag (residues 319-541)	Barnes et al., 2020b	https://doi.org/10.1016/j.cell.2020.06.025
pPPI4-SARS-CoV-2 hexapro S trimer 6xHisTag	Hsieh et al., 2020	https://doi.org/10.1126/science.abd0826
pCR3.1_GA_S2_R346S	Weisblum et al., 2020	https://elifesciences.org/articles/61312
pCR3.1_GA_S2_N439K	Weisblum et al., 2020	https://elifesciences.org/articles/61312
pCR3.1_GA_S2_K444Q	Weisblum et al., 2020	https://elifesciences.org/articles/61312
pCR3.1_GA_S2_V445E	Weisblum et al., 2020	https://elifesciences.org/articles/61312
pCR3.1_GA_S2_ Y453F	Muecksch et al., 2021	http://biorxiv.org/lookup/doi/10.1101/2021.03.07.434227
pCR3.1_GA_S2_L455R	Weisblum et al., 2020	https://elifesciences.org/articles/61312
pCR3.1_GA_S2_A475V	Weisblum et al., 2020	https://elifesciences.org/articles/61312
pCR3.1_GA_S2_Q493R	Weisblum et al., 2020	https://elifesciences.org/articles/61312
pCR3.1_GA_S2_E484K_R683G	Wang et al., 2021	http://www.nature.com/articles/s41586-021-03324-6
pCR3.1_GA_S2_N501Y	Weisblum et al., 2020	https://elifesciences.org/articles/61312
pCR3.1_GA_S2_ D614G	Wang et al., 2021	https://doi.org/10.1038/s41586-021-03324-6
pCR3.1_GA_S2_R683G	Wang et al., 2021	http://www.nature.com/articles/s41586-021-03324-6
pCR3.1_GA_S2_K417N_E484K_N501Y_R683G	Wang et al., 2021	http://www.nature.com/articles/s41586-021-03324-6
Software and algorithms		
IgBLAST Change-O R Package	Change-O	https://pypi.org/project/changeo/0.3.12/
Shazam R Package	Yaari et al., 2012	https://cran.r-project.org/web/packages/shazam/index.html
Alakazam R Package	Gupta et al., 2015; Kyte and Doolittle, 1982; Hill, 1973; Chao et al., 2015	https://cran.r-project.org/web/packages/alakazam/index.html
GISAID	Elbe and Buckland-Merrett, 2017	https://www.gisaid.org RRID:SCR_018251
Clustal Omega	Sievers et al., 2011	https://www.ebi.ac.uk/Tools/msa/clustalo/RRID: SCR_001591
Gen5	BioTek	https://www.biotek.com/products/software-robotics-software/gen5-microplate-reader-and-imager-software/RRID: SCR_017317
Prism 8 and 9	GraphPad	https://www.graphpad.com/scientific-software/prism/RRID: SCR_002798
SerialEM 3.7	Mastronarde, 2005	https://bio3d.colorado.edu/SerialEM/RRID: SCR_017293
cryoSPARC 2.14 and 2.15	Punjani et al., 2017	**Error! Hyperlink reference not valid.** RRID: SCR_016501

(Continued on next page)

Continued

REAGENT or RESOURCE	SOURCE	IDENTIFIER
UCSF Chimera	Goddard et al., 2018	http://plato.cgl.ucsf.edu/chimera/ RRID: SCR_004097
XDS	Kabsch, 2010	https://xds.mr.mpg.de/RRID: SCR_015652
CCP4 suite	Winn et al., 2011	https://www.ccp4.ac.uk RRID: SCR_007255
PHASER	McCoy et al., 2007	https://www.phenix-online.org/documentation/reference/phaser.html RRID: SCR_014219
Phenix	Terwilliger et al., 2018	https://www.phenix-online.org/ RRID: SCR_014224
Coot	Emsley et al., 2010	https://www2.mrc-lmb.cam.ac.uk/personal/pemsley/coot/RRID: SCR_014222
AIMLESS	Winn et al., 2011	https://www.ccp4.ac.uk/html/aimless.html RRID: SCR_015747
MolProbityCoot	Chen et al., 2010	http://molprobity.biochem.duke.edu RRID: SCR_014226 https://www2.mrc-lmb.cam.ac.uk/personal/pemsley/coot/RRID: SCR_014222
MAFFT	Katoh et al., 2019	https://mafft.cbrc.jp/alignment/server/ RRID:SCR_011811
SAbDab	Dunbar et al., 2014	http://opig.stats.ox.ac.uk/webapps/newsabdab/sabdab/
Terra cellranger_workflow v17	Li et al., 2020	https://app.terra.bio/
Immcantation framework R packages	Gupta et al., 2015	https://immcantation.readthedocs.io/en/stable/
Seurat R toolkit for single cell genomics v 3.0	Stuart et al., 2019	https://satijalab.org/seurat/
Other		
BioTek 406 El406 Microplate Washer/Dispenser	BioTek	N/A
BioTek Synergy HT	BioTek	N/A
MaxiSorp 384-well Microplate	Sigma	Cat#P6366
LS Columns	Miltenyi Biotec	Cat#130-042-401
CD20 MicroBeads, Human	Miltenyi Biotec	Cat#130-091-104
Infors Minitron25 mm w/Humidity Incubator/Shaker	Infors HT	Cat#S-000127238
Pyrex Delong Shaker Erlenmeyer Flasks with Baffles	VWR	Cat#4444-500
Poly-Prep Chromatography Columns	Bio-Rad	Cat#731-1550
Zeba Spin Desalting Columns, 40K MWCO, 5mL	Thermo Fisher	Cat#87771
ÄKTA Pure FPLC System	Cytiva	Cat#29-0182-24
HiLoad 16/600 Superdex 200pg 120 mL Column	Cytiva	Cat#28-9893-35
Criterion TGX Precast Gels	Bio-Rad	Cat#5671095
NanoDrop 2000c Spectrophotometer	Thermo Fisher	Cat#ND-2000C
Corning Costar Brand 96-Well EIA/RIA Plates	Fisher Scientific	Cat#07-200-721
Synergy H4 Plate Reader	BioTek	N/A
Chromium Controller	10x Genomics	Cat#PN-1000202
Chromium NextGEM Chip G Single Cell kit, 48rxns	10x Genomics	Cat#PN-1000120
Chromium NextGEM Single Cell 5′ Library & Gel Bead kit v1.1, 16rxns	10x Genomics	Cat#PN-1000165

(Continued on next page)

Continued

REAGENT or RESOURCE	SOURCE	IDENTIFIER
Chromium Single Cell 5′ Feature Barcode Library kit, 16rxns	10x Genomics	Cat#PN-1000080
Chromium Single Cell 5′ Library Construction kit, 16rxns	10x Genomics	Cat#PN-1000020
Chromium Single Cell V(D)J Enrichment kit, Human B Cell, 96rxns	10x Genomics	Cat#PN-1000016
Single Index Kit N Set A, 96rxns	10x Genomics	Cat#PN-1000212
Single Index Kit T Set A, 96rxns	10x Genomics	Cat#PN-1000213
NextSeq 500/550 High Output Kit v2.5 (150 Cycles)	Illumina	Cat#20024907
HiSeq X Ten Reagent Kit v2.5 - 10 pack	Illumina	Cat#FC-501-2521
Pierce Streptavidin Coated Plates, Clear, 96-Well	Thermo Scientific	Cat#15125
Nunc Maxisorb 384-well plates	Millipore Sigma	Cat#P6491
HisTrap FF	GE Healthcare Life Sciences	Cat#17-5255-01
HisTrap HP	GE Healthcare Life Sciences	Cat#17-5248-02
HiLoad 16/600 Superdex 200 pg	GE Healthcare Life Sciences	Cat#28-9893-35
Superose 6 Increase 10/300 GL	GE Healthcare Life Sciences	Cat#29-0915-96
HiTrap MabSelect SuRe column, 5 mL	GE Healthcare Life Sciences	Cat#11-0034-95
HiTrap MabSelect SuRe column, 1 mL	GE Healthcare Life Sciences	Cat#11-0034-93
Superdex 200 Increase 10/300 GL	GE Healthcare Life Sciences	Cat#28-9909-44
Amicon Ultra-15 Centrifugal Filter Devices	Millipore	Cat#UFC903096
PD-10 Desalting Columns	GE Healthcare Life Sciences	Cat#17-0851-01
HiTrap NHS-Activated HP, 5 mL	GE Healthcare Life Sciences	Cat#17-0716-01
300 Mesh Pure C carbon-coated copper grids	EM Sciences	
300 Mesh UltrAuFoil® Holey Gold Films, R 1.2/1.3	Electron Microscopy Sciences	Cat#Q350AR13A
Sensor Chip CM5	Cytiva	Cat#29104988

RESOURCE AVAILABILITY

Lead contact
Further information and requests may be directed to, and will be fulfilled by the lead author, Ramnik J. Xavier (xavier@molbio.mgh.harvard.edu)

Materials availability
All reagents generated in this study are available upon request from the Lead Contact.

Data and code availability
Antibody sequences and scRNA-seq count matrices were deposited in the Single Cell Portal of the Broad Institute (SARS-CoV-2 Antibodies, Accession # SCP1317, https://singlecell.broadinstitute.org/single_cell/study/SCP1317/sars-cov-2-antibodies). Raw scRNA-seq files were deposited on the platform DUOS (https://duos.broadinstitute.org/dataset_catalog) with the DUOS ID: DUOS-000125. Please note that this repository also contains a metadata file matching raw sequences to the subjects used in this study. Source codes of the scRNA-seq and Ab repertoire analyses are deposited on GitHub (https://github.com/EraslanBas/Sars_Cov2_Antibodies).

The coordinates generated from X-ray crystallographic studies of the BG4-25 – CR3022 – RBD complex have been deposited at the Protein Data Bank (https://www.rcsb.org) under accession code PDB: 7M6D. The atomic models and cryo-EM maps generated from cryo-EM studies of the BG10-19 – S 6P, BG7-15 – S 6P, BG1-22 – S 6P, BG7-20 – S 6P, and BG1-24 – S 6P complexes have been deposited at the PDB and Electron Microscopy Data Bank (EMDB: https://www.ebi.ac.uk/pdbe/emdb/) under the following accession numbers: PDB: 7M6E, 7M6F, 7M6G, 7M6H, and 7M6I; EMD: EMD-23694, EMD-23695, EMD-23696, EMD-23697, and EMD-23698, respectively.

EXPERIMENTAL MODEL AND SUBJECT DETAILS

All work with human samples was performed in accordance with approved Institutional Review Board protocols (IRB) which were reviewed by the IRB at Brigham and Women's Hospital, Boston. Subjects who had recovered from COVID-19 (Table S1) were recruited through a patient cohort that has been created in collaboration between The Broad Institute of MIT and Harvard, Cambridge (MA, USA) and Brigham and Women's Hospital, Boston (MA, USA) under IRB protocol 2020P000849, "Biorepository for Samples from those at increased risk for or infected with SARS-CoV-2." Blood draws were performed at Brigham and Women's Hospital.

METHOD DETAILS

Serum RBD Enzyme-linked immunosorbent assay (ELISA)

Serum ELISAs against SARS-CoV-2 RBD were performed in a protocol modified from Roy et al. (2020). MaxiSorp 384-well microplates (Sigma) were coated with 50 μl/well of 2,500 ng/ml of SARS-CoV-2 RBD in coating buffer (1 packet BupH carbonate-bicarbonate (ThermoFisher) in 500 mL of Milli-Q H20) overnight at 4°C. Plates were then washed 3 times with 100 μl/well of wash buffer (0.05% Tween-20, 400 mM NaCl, and 50 mM Tris-HCl [pH 8.0] in Milli-Q H20) using a BioTek 406 plate washer. Plates were blocked by adding 100 μl/well of blocking buffer (1% BSA, 140 mM NaCl, and 50 mM Tris-HCl (pH 8.0)) for 30 min at room temperature. Plates were then washed as described above. 50 μL of 1:100 diluted serum samples in dilution buffer (1% BSA, 0.05% Tween-20, 140 mM NaCl, and 50 mM Tris-HCl (pH 8.0)) were added to the wells and incubated for 30 min at 37°C. Plates were then washed 7 times as described above. 50 μl/well of 1:25,000 diluted detection Ab solution (HRP-anti human IgG and IgM, Bethyl Laboratory #A80-104P, A80-100P) was added to the wells and incubated for 30 min at room temperature. Plates were then washed 7 times as described above. 40 μl/well of Pierce TMB peroxidase substrate (ThermoFisher) was then added to the wells and incubated at room temperature for 3 min (IgG) or 5 min (IgM). The reaction was then stopped by adding 40 μl/well of stop solution (0.5M H2S04 in Milli-Q H20) to each well. The OD was read after 15 min at 450 nm and 570 nm on a BioTek Synergy HT using Gen5 software. For control mABs CR3022 (Tian et al., 2020) IgG1 and IgM (Absolute Antibody #Ab01680-10.0, Ab01680-15.0) dilution curves, the mAbs were diluted to a concentration of 1 μg/ml in dilution buffer and duplicate 12 two-fold serial dilution curves were generated. One known positive and two known negative samples were included on each plate as controls.

Serum ELISA analysis

A standard curve based on absorbances from the mAb CR3022 (Tian et al., 2020) dilution series included with each plate was used to estimate Ab abundance in test samples and allow for comparison of results across batches. Estimated Ab abundance in test samples was compared to the background signal from a cohort of pre-pandemic serum samples that served as negative controls. Serum samples with Ab abundance greater than 3 standard deviations (SD) above the mean of the pre-pandemic serum samples were considered to be positive and samples with Ab abundance less than 3 SD above the mean of the pre-pandemic serum samples were considered negative.

SARS-CoV-2 and SARS-CoV pseudovirus neutralization assay

Neutralizing activity against SARS-CoV-2 pseudovirus was measured using a single-round infection assay in human ACE2-expressing target cells. Convalescent patient serum samples were tested against pseudotyped virus particles produced in 293T/17 cells (American Type Culture Collection) by co-transfection of plasmids encoding codon-optimized S (containing D at position 614) with a partially deleted cytoplasmic tail (provided by Dr. Dan Barouch, Beth Israel Deaconess Medical Center), and the HIV-1 backbone vector SG3 Δ Env (NIH AIDS Reagent Program). This pseudovirus strain was used for infecting TZM.bl/ACE2 target cells which encode an integrated luciferase reporter gene under control of an HIV-1 LTR. Subsequently, a second pseudovirus assay platform was implemented and used for testing neutralizing activity of purified mAbs. This assay platform utilized pseudovirus produced in 293T/17 cells by co-transfection of plasmids encoding codon-optimized SARS-CoV-2 full-length S (containing G at position 614), packaging plasmid pCMV ΔR8.2 expressing HIV-1 gag and pol, and luciferase reporter plasmid pHR' CMV-Luc. Plasmids were kindly provided by Dr. Barney Graham (NIH, Vaccine Research Center). This pseudovirus strain was used for infecting 293/ACE2 target cells. The 293T and TZM.bl cell lines stably overexpressing the human ACE2 cell surface receptor protein were kindly provided by Drs. Michael Farzan and Huihui Ma (The Scripps Research Institute). For neutralization assays, serial dilutions of patient serum samples (primary 1:20 with 3-fold dilution series) or mAbs (up to 50 μg/ml with 5-fold dilution series) were performed in duplicate followed by addition of pseudovirus. Plates were incubated for 1 hour at 37°C followed by addition of 293T/ACE2 or TZM.bl/ACE2 target cells (1x10^4/well). Wells containing cells + pseudovirus (without sample) or cells alone acted as positive and negative infection controls, respectively. Assays were harvested on either day 2 (TZM.bl/ACE2 target cells) or day 3 (293/ACE2 target cells) using Promega Bright-Glo luciferase reagent and luminescence detected with a Perkin-Elmer Victor luminometer. Titers were determined as the serum dilution or mAb concentration that inhibited 50% or 80% virus infection (serum ID_{50}/ID_{80} or mAb IC_{50}/IC_{80} titers, respectively).

Similarly, neutralizing activity of mAbs against SARS-CoV pseudovirus as well as SARS-CoV-2 variants B.1.1.7 and B.1.351 was determined using HIV-based lentiviral particles pseudotyped with either SARS-CoV S lacking the C-terminal 21 amino acids of the cytoplasmic tail or SARS-CoV-2 S (containing G at position 614) carrying the reported spike mutations in B.1.1.7 and B.1.351 (Tegally et al., 2020; Davies et al., 2021). Pseudotyped particles were generated and neutralization assays were performed as previously

described (Crawford et al., 2020a, 2020b). Briefly, the genes encoding the respective spike proteins were co-transfected with Env-deficient HIV backbone to create pseudotyped lentiviral particles. For neutralization assays, 4- or 5-fold serially diluted purified IgG was incubated with SARS-CoV pseudotyped virus for 1 hour at 37°C. The virus/Ab mixture was added to 293TACE2 target cells and incubated for 48 hours at 37°C, then cells were lysed and luciferase activity was measured using Britelite Plus (Perkin Elmer). Relative luminescence units (RLUs) were normalized to values derived from cells infected with pseudotyped virus in the absence of Ab. Data were fit to a 5- parameter nonlinear regression in AntibodyDatabase (West et al., 2013).

Blood sample processing

60-80 mL of blood from each donor were processed using Ficoll Paque Plus (GE Healthcare) in order to isolate peripheral blood mononuclear cells (PBMCs) according to the manufacturer's instructions. After PBMC isolation we immediately proceeded with isolation of CD20$^+$ B cells using magnetic cell separation (MACS). In brief, cells were resuspended in MACS buffer (phosphate buffered saline (PBS) pH 7.2, 0.5% bovine serum albumin (BSA) and 2 mM EDTA) and stained with mouse anti-human CD20 IgG1 Ab coupled to magnetic beads (Miltenyi Biotec, #130-091-104). After washing and resuspending in MACS buffer cells were added to LS columns (Miltenyi Biotec) placed on a magnetic stand and the columns washed 3 times with 3 mL MACS buffer before removing the columns from the magnet and elution of cells according to the manufacturer's instructions. Cells were then washed and resuspended in Cell Staining Buffer (Biolegend, #420201).

Cell staining and sorting

CD20 enriched cells were stained with DNA-barcoded Totalseq C Abs (Biolegend) according to the manufacturer's instructions. In brief, cells underwent Fc receptor blocking with Human TruStain FcX Fc (Biolegend) for 10 minutes at 4°C, after which cells were washed and resuspended in Cell Staining Buffer (Biolegend, #420201). Cells from different subjects were then stained with different Totalseq C Abs (Biolegend): 1 (TotalSeq-C0251 anti-human Hashtag 1 Antibody), 2 (TotalSeq-C0252 anti-human Hashtag 2 Antibody), 3 (TotalSeq-C0253 anti-human Hashtag 3 Antibody), 4 (TotalSeq-C0254 anti-human Hashtag 4 Antibody), 6 (TotalSeq-C0256 anti-human Hashtag 6 Antibody), 7 (TotalSeq-C0257 anti-human Hashtag 7 Antibody), 8 (TotalSeq-C0258 anti-human Hashtag 8 Antibody), 10 (TotalSeq-C0260 anti-human Hashtag 10 Antibody). After staining with hashing Abs, cells were washed 3 times in Cell Staining Buffer (Biolegend, #420201) and then up to 7 separate samples were combined for staining of antigen binding B cells. For this, the combined samples were stained with either 1 μg/ml biotinylated SARS-CoV-2 spike trimer or 1 μg/ml biotinylated SARS-CoV-2 RBD (See below for protein expression; biotinylation was performed using avitag technology (Avidity) following the manufacturer's instructions). Cells were simultaneously stained with FITC mouse anti-human CD19 Ab (BD, 340864) and incubated for 20 minutes at 4°C before they were washed and resuspended in PBS with 5% fetal bovine serum (FBS). Cells were then stained with streptavidin-coupled APC (Biolegend #405207) for 5 minutes at 4°C and washed and resuspended in PBS with 5% FBS. Antigen binding B cells were then sorted using a Sony MA900 cell sorter by gating on live cells in the forward scatter and side scatter (Figures 1A and 1B) and on CD19-FITC and SARS-CoV-2 S-APC or RBD-APC double-positive cells. After sorting, cells were washed and counted using a hemocytometer and microscopy, before resuspending up to 10,000 cells in a volume of 32 μL for 5′ single cell RNA-Seq (see below).

5′ scRNA-seq library generation

Cells were separated into droplet emulsions using the Chromium Next GEM Single-cell 5′ Solution (v1.1) and the 10x Chromium Controller. 5,000-10,000 cells were loaded per channel of the Chromium Next GEM single-cell 5′ (v1.1) Chip G. Following lysis of cells, barcoded mRNA reverse transcription, and cDNA amplification, a 0.6X SPRI cleanup was performed, and the supernatant was set aside for Feature Barcoding library construction as instructed by the Chromium NextGEM single-cell V(D)J v1.1 protocol. A final elution of 45 μL was saved for further construction of libraries. Using the saved supernatant of the 0.6X cDNA cleanup, Feature Barcoding libraries were completed according to the 5′ Next GEM (v1.1) Feature Barcoding library construction methods provided by 10x Genomics. Gene expression and V(D)J libraries were created according to manufacturer's instruction (10x Genomics), which includes enzymatic fragmentation, adaptor ligation, and sample index barcoding steps. The V(D)J libraries were created from the original following the Chromium NextGEM single-cell V(D)J v1.1 protocol.

scRNA-seq library sequencing

Gene expression, feature barcoding libraries, and BCR enriched V(D)J libraries were sequenced on a Nextseq500 (Illumina) using a high output 150 cycle flowcell, with the read configuration Read 1: 28 cycles, Read 2: 96 cycles, Index read 1: 8 cycles or sequenced on a HiSeq X (Illumina), using a 150 cycle flowcell with the read configuration: Read 1: 28 cycles, Read 2: 96 cycles, Index read 1: 8 cycles. Feature Barcoding libraries were spiked into the gene expression libraries (at 10%–20% of the sample pool) prior to sequencing. All BCR enriched V(D)J libraries were pooled together and sequenced on a NextSeq500 (Illumina) using the same parameters as previously mentioned.

Ab production

Ab VDJ heavy chain and VJ light chain sequences of selected mAbs were produced as minigenes and cloned into IgG1 heavy chain, IgA1 heavy chain, IgA2 heavy chain, kappa light chain or lambda light chain expression vectors as previously described (Wardemann

et al., 2003; Wang et al., 2020). After cloning into expression vectors, matching mAb heavy chain and light chain plasmids were co-transfected into Expi293F cells following the manufacturer's instructions. In brief, heavy chain plasmid DNA and light chain plasmid DNA were diluted in 1.5ml Opti-Plex Complexation Buffer (Invitrogen) before mixing with 80 μl ExpiFectamine 293 Reagent (Invitrogen) diluted in 1.4 mL Opti-Plex Complexation Buffer (Invitrogen). For dimeric IgA production equal amounts of heavy chain plasmid DNA, light chain plasmid DNA and J chain plasmid DNA were used in the transfection. Mixture was incubated for 15 minutes at room temperature before adding to 25 mL of Expi293F cells at a density of 3.0×10^6 viable cells/ml and incubation in a shaker incubator according to the manufacturer's instructions. ExpiFectamine 293 Transfection Enhancer 1 and 2 (150 μl and 1.5 ml, respectively) were added 18 hours post-transfection. mAb containing supernatants were harvested after 7 days by centrifugation of cells at 3,000 g for 20 minutes and transfer of supernatants into 50 mL Falcon tubes (Fisher Scientific). Prior to size exclusion chromatography (see below) IgA dimers were purified from transfection supernatants using peptide M coupled agarose beads (Invivogen) according to the manufacturer's instructions.

IgA dimer purification through size exclusion chromatography

IgA dimers were purified using a 120mL HiLoad™ 16/600 Superdex™ 200pg (Cytiva, #28-9893-35) column on an ÄKTA Pure FPLC system operating at 4°C. After equilibration of the column with PBS each IgA preparation was loaded via a 10mL superloop at a flow rate of 1.25mL/min and 1.5mL fraction were collected. Isolated peaks consistent with IgA multimers, IgA dimers and IgA monomers were detected at 0.3-0.4, 0.4-0.5 and 0.5-0.6 column volumes respectively (Figure S2H). Fractions spanning all three peaks were collected and evaluated individually by running Criterion™ TGX™ precast gels (Biorad 5671095) under non-reducing conditions with a Precision Plus Protein Kaleidoscope Prestained Protein Standard (Biorad #1610375) (Figure S2I).

mAb ELISA testing

mAb concentrations were determined measuring absorbance at 280nm using Nanodrop 2000c (Thermo Scientific) or IgG specific ELISA as previously described (Tiller et al., 2008). mAb reactivities to SARS-CoV-2 S, SARS-CoV-2 RBD, SARS-CoV S, SARS-CoV RBD, MERS-CoV S and MERS-CoV RBD were determined using the same protocol with the following modifications: Antigens were coated on Corning Costar Brand 96-Well EIA/RIA plates at a concentration of 5 μg/ml. mAb binding was then assessed at starting concentrations of 1 μg/ml, 1.1 μg/ml and 1.2 μg/ml for IgG, monomeric IgA and dimeric IgA respectively in order to achieve equal Fab molar concentrations. 3 consecutive 1/4 dilutions were performed. Positive control mAbs used in these assays included BG10-19 for SARS-CoV-2 S and SARS-CoV-2 RBD (see above), 3B12 (Absolute Antibody #Ab01673-10.0) for MERS-CoV S and MERS-CoV RBD (Tang et al., 2014) and S227.14 (Absolute Antibody #Ab00263-10.0) for SARS-CoV S and SARS-CoV RBD (Rockx et al., 2008). Antigen specific ELISA results are expressed as AUC using Graphpad PRISM software. Polyreactivity ELISAs were performed as previously described (Tiller et al., 2008) with the following modification: In addition to the antigens ssDNA, dsDNA, LPS and insulin (Tiller et al., 2008), streptavidin-coupled APC (Biolegend #405207) was used as a fifth antigen in order to assess potential off target binding against this reagent used for cell sorting (see above). As described previously (Tiller et al., 2008), polyreactivity is defined as reactivity to 2 or more antigens among the antigens single stranded DNA, double stranded DNA, lipopolysaccharide (LPS) or insulin. As previously described, mAbs ED38, JB40 and mGO53 (Wardemann et al., 2003) were used as strongly polyreactive, intermediately polyreactive and non-polyreactive control mAbs respectively. In ELISA assays including IgG, IgA monomers and IgA dimers, HRP-conjugated goat anti-human kappa and lambda chain Abs (Biorad #STAR127P and #STAR129P) were used as secondary Abs at a 1/5000 dilution.

Off-target mAb binding to baculovirus (BV) particles generated in Sf9 insect cells was tested as previously described (Hötzel et al., 2012). A solution of 1% baculovirus in 100mM sodium bicarbonate buffer pH 9.6 was adsorbed to a 384-well ELISA plate (Nunc Maxisorp) using a Tecan Freedom Evo2 liquid handling robot and the plate was incubated overnight at 4°C. Following blocking with 0.5% BSA in PBS, 1 μg/ml of IgG was added to the blocked assay. Plates were incubated for 3 hours at room temperature. mAb binding was detected using an HRP-conjugated anti-Human IgG (H&L) secondary Ab (Genscript). ELISA was developed using SuperSignal ELISA Femto Maximum Sensitivity Substrate (Thermo Scientific). Anti-HIV mAbs NIH45-46 (Scheid et al., 2011) and 45-46m2 (Diskin et al., 2013) were used as positive controls and mAb 3BNC117 (Scheid et al., 2011) was used as negative control. Measurements were performed in quadruplicate and OD values within 1.5-fold the negative control were considered to be negative.

Neutralization activity of mAbs against authentic SARS-CoV-2

Vero E6-TMPRSS2 were seeded at 10,000 cells per well the day prior to infection in CellCarrier-384 ultra microplate (Perkin Elmer). mAb samples were tested in 4-fold 9-point dilution spots starting at a highest concentration of 100 μg/mL. Serial diluted mAbs were mixed separately with diluted SARS-CoV-2 virus and incubated at 37°C with 5% CO_2 for 1 hour. mAb-virus complexes were added to the cells in triplicate. Plates were incubated at 37°C with 5% CO_2 for 48 hours. After that, plates were fixed and inactivated using 4% paraformaldehyde in PBS for 2 hours at room temperature. Plates were then washed and incubated with diluted anti-SARS-CoV/SARS-CoV-2 nucleoprotein mouse Ab (Sino) for 1.5 hours at room temperature. Plates were subsequently incubated with Alexa488-conjugated goat anti-mouse (JacksonImmuno) for 45 mins at room temperature, followed by nuclear staining with Hoechst 33342 (ThermoFisher). The fluorescence images were recorded and analyzed using Opera Phenix High Content Screening System. The half-maximal inhibitory concentrations (IC_{50}) were determined using four parameters logistic regression (GraphPad Prism 8.0).

Protein expression and purification

Expression and purification of SARS-CoV-2 6P stabilized S trimers (Hsieh et al., 2020) and constructs encoding the sarbecovirus RBDs were conducted as previously described (). Briefly, constructs were purified from supernatants of transiently transfected Expi293F cells (GIBCO) by Ni^{2+}-NTA affinity and size exclusion chromatography (SEC). Peak fractions were identified by SDS-PAGE, pooled, and stored at 4°C. IgGs were expressed, purified, and stored as described (Barnes et al., 2020b). Fabs were generated by papain digestion using crystallized papain (Sigma-Aldrich) in 50 mM sodium phosphate, 2 mM EDTA, 10 mM L-cysteine, pH 7.4 for 30-60 min at 37°C at a 1:100 enzyme:IgG ratio. To remove undigested IgGs and Fc fragments, digested products were applied to a 1-mL HiTrap MabSelect SuRe column (GE Healthcare Life Sciences) and the flow-through containing cleaved Fabs was collected. Fabs were further purified by SEC using a Superdex 200 Increase 10/300 column (GE Healthcare Life Sciences) in TBS before concentrating and storage at 4°C.

Cryo-EM sample preparation

Purified Fab and S 6P trimer were incubated at a 1.1:1 molar ratio per protomer on ice for 30 minutes prior to deposition on a freshly glow-discharged 300 mesh, 1.2/1.3 UltrAuFoil grid. Immediately before 3 μl of complex was applied to the grid, fluorinated octyl-maltoside was added to the Fab-S complex to a final detergent concentration of 0.02% w/v, resulting in a final complex concentration of 3 mg/ml. Samples were vitrified in 100% liquid ethane using a Mark IV Vitrobot after blotting for 3 s with Whatman No. 1 filter paper at 22°C and 100% humidity.

Cryo-EM data collection and processing

Data collection and processing followed a similar workflow to what has been previously described in detail (Barnes et al., 2020a). Briefly, micrographs were collected on a Talos Arctica transmission electron microscope (Thermo Fisher) operating at 200 kV for all Fab-S complexes. Data were collected using SerialEM automated data collection software (Mastronarde, 2005) and movies were recorded with K3 camera (Gatan). Data collections parameters are summarized in Table S5. For all datasets, cryo-EM movies were patch motion corrected for beam-induced motion including dose-weighting within cryoSPARC v2.15 (Punjani et al., 2017) after binning super resolution movies. The non-dose-weighted images were used to estimate CTF parameters using cryoSPARC implementation of the Patch CTF job. Processing for all datasets was carried out in a similar fashion. Briefly, an initial set of particles was picked based on templates from 2D classification of blob picked particles on a small sub-set of images. This set was pared down through several rounds of 3D classification. An *ab initio* job on a small good subset of these particles revealed distinct states and junk particles. Full set of particles was heterogeneously refined against distinct states, as well as a junk class acting as a trap for bad particles. Particles from each were separately refined using non-uniform refinement in C1 symmetry. Particles from distinct states were re-extracted without binning and were further refined separately in several rounds of 3D classification. Particles were subdivided into groups based on beam-tilt, refined separately for CTF parameters and aberration correction. For all states, a soft mask (3-pixel extension, 6-pixel soft edge) was generated to exclude Fab constant domains for local non-uniform refinements. To improve the density for the BG1-22 – RBD, BG7-20 – RBD, and BG1-24 – RBD interfaces, a soft mask was generated around the RBD and Fab variable domain and particles were subjected to non-uniform local refinement in cryoSPARC. The resolution at the Fab-RBD interface was modestly improved and used to model coordinates in the overall Fab – S trimer complex structures. Overall reported resolutions are based on gold standard FSC calculations.

Cryo-EM Structure Modeling and Refinement

Coordinates for initial complexes were generated by docking individual chains from reference structures into cryo-EM density using UCSF Chimera (Goddard et al., 2018) (see Table S5 for PDB coordinates). Models were then refined into cryo-EM maps rigid body and real space refinement with morphing in Phenix (Terwilliger et al., 2018). Sequence-updated models were built manually in Coot (Emsley et al., 2010) and then refined using iterative rounds of real-space refinement in Phenix and Coot. Glycans were modeled at potential *N*-linked glycosylation sites (PNGSs) in Coot using 'blurred' maps processed with a variety of B-factors generated in cryoSPARC v2.15. Validation of model coordinates was performed using MolProbity (Chen et al., 2010) (Table S5).

BG4-25-RBD X-ray crystallography experiments

Crystallization trials for a stoichiometric complex of BG4-25 – SARS-CoV2 RBD – CR3022 were carried out at room temperature using the sitting drop vapor diffusion method by mixing equal volumes of the Fab-RBD complex and reservoir using a TTP LabTech Mosquito robot and commercially-available screens (Hampton Research). Crystals were obtained in 0.05 M citric acid, 0.05 M BIS-TRIS propane pH 5.0 and 16% polyethylene glycol 3350 and quickly cryo-protected in a solution matching the reservoir + 20% glycerol. X-ray diffraction data were collected for Fab-RBD complex at the Stanford Synchrotron Radiation Lightsource (SSRL) beamline 12-2 on a Pilatus 6M pixel detector (Dectris). Data from a single crystal were indexed and integrated in XDS (Kabsch, 2010) and merged using AIMLESS in *CCP4* (Winn et al., 2011) (Table S6). The Fab-RBD complex structure was determined by molecular replacement in PHASER (McCoy et al., 2007) using Fab and RBD coordinates from individual components of PDB 6XC3 (CC12.1 Fab – CR3022 Fab – SARS-CoV2 RBD) as search models after trimming heavy chain and light chain CDR loops for CC12.1 Fab. Coordinates were refined using rigid body and B-group refinement in Phenix (Adams et al., 2010) followed by cycles of manual building in Coot (Emsley et al., 2010) (Table S6).

Structural Analyses

CDR lengths and Kabot numbering were calculated based on IMGT definitions (Lefranc et al., 2015). Structure figures were made with UCSF ChimeraX. Local resolution maps were calculated using cryoSPARC v 2.15. Buried surface areas were calculated using PDBePISA (Krissinel and Henrick, 2007) and a 1.4 Å probe. Potential hydrogen bonds were assigned as interactions that were < 4.0Å and with A-D-H angle > 90°. Potential van der Waals interactions between atoms were assigned as interactions that were < 4.0Å. Hydrogen bond and van der Waals interaction assignments are tentative due to resolution limitations.

Surface Plasmon Resonance (SPR) binding experiments

SPR experiments were performed using a Biacore T200 instrument (GE Healthcare). ACE2 microbody (Tada et al., 2020) was immobilized on a CM5 chip by primary amine chemistry at pH 4.5 to a final response level of ~1000 resonance units (RUs). Fabs were complexed with 100 nM SARS2 S 6P or SARS2 RBD at a 10:1 molar ratio and incubated for a minimum of 1 hour. Antigen or Fab-antigen complex was injected over immobilized ACE2 microbody surface at a flow rate of 30 μl/min for a contact time of 300 s. Sensorgrams were buffer corrected using an injection of 0.01 M HEPES pH 7.4, 0.15 M NaCl, 3 mM EDTA, 0.005% v/v surfactant P20 buffer.

SARS-CoV-2 mutant RBD and sarbecovirus RBD ELISA binding assay

Binding of Fabs to SARS-CoV-2 RBDs containing single mutations or to sarbecovirus RBDs was evaluated by ELISA. RBD antigens (mutant or wild-type) were adsorbed to 384-well Nunc MaxiSorp plates (Sigma) at a concentration of 2 μg/mL overnight. Plates were blocked with 3% BSA in TBS-T (TBS with 0.05% Tween20) for 1 h at room temperature, then 5-fold serial dilutions starting at 10 μg/mL of Fab were added. Plates were washed with TBS-T and bound Fab was detected using an HRP-conjugated secondary Ab (Genscript) and SuperSignal ELISA Femto Substrate (Thermo Scientific). AUC for each Fab-antigen pair was calculated using Graphpad PRISM software. Fold decrease in AUC was calculated relative to SARS-CoV2 RBD AUC for the same Fab. Data shown are representative of two independent experiments.

SARS-CoV-2 mutant pseudotyped reporter virus and mutant pseudotyped virus neutralization assay

SARS-CoV-2 pseudotyped particles were generated as previously described (Robbiani et al., 2020; Schmidt et al., 2020). Briefly, 293T cells were transfected with pNL4-3ΔEnv-nanoluc and pSARS-CoV-2-$S_{\Delta19}$. For generation of RBD mutant pseudoviruses, pSARS-CoV-2-$S_{\Delta19}$ carrying indicated spike mutations was used instead (Muecksch et al., 2021; Wang et al., 2021; Weisblum et al., 2020). Particles were harvested 48 h post-transfection, filtered and stored at −80°C.

Four-fold serially diluted mAbs were incubated with SARS-CoV-2 pseudotyped virus for 1 h at 37°C. The mixture was subsequently incubated with HT1080$_{Ace2}$ cl14 cells (Schmidt et al., 2020) for 48 h after which cells were washed with PBS and lysed with Luciferase Cell Culture Lysis 5 × reagent (Promega). Nanoluc Luciferase activity in lysates was measured using the Nano-Glo Luciferase Assay System (Promega) with the Glomax Navigator (Promega). The obtained relative luminescence units were normalized to those derived from cells infected with SARS-CoV-2 pseudotyped virus in the absence of mAbs. The half-maximal and 90% inhibitory concentrations (IC_{50} and IC_{90}) were determined using four-parameter nonlinear regression (least-squares regression method without weighting; constraints: top = 1, bottom = 0) (GraphPad Prism).

mAb resistance selection experiments

293T/ACE2.cl22 (Schmidt et al., 2020) were cultured in Dulbecco's Modified Eagle Medium (DMEM) supplemented with 10% fetal bovine serum (FBS) at 37°C and 5% CO_2. Cells have been tested negative for contamination with mycoplasma. rVSV/SARS-CoV-2/GFP chimeric virus stocks were generated by infecting 293T/ACE2.cl22 cells. Supernatant was harvested 1 day post infection (dpi), cleared from cellular debris, aliquoted and stored at −80°C. Two plaque purified variants designated rVSV/SARS-CoV-2/GFP$_{1D7}$ and rVSV/SARS-CoV-2/GFP$_{2E1}$ that encode F157S/R685M (1D7) and D215G/R683G (2E1) substitutions were used in these studies (Schmidt et al., 2020). For BG10-19 selection experiments, the virus was passaged multiple times in the presence of 1 μg/ml or 5 μg/ml of mAb. At passage 4, virus was allowed to replicate in the presence of mAb until all the cells were infected then harvested. The virus was then passaged in the presence of mAb for a fifth and final time before supernatant was harvested for further analysis. To isolate individual mutants, the supernatants of passage 5 were serially diluted and individual viral foci were isolated by limiting dilution in 96-well plates.

For the identification of putative mAb resistance mutations, RNA was isolated from aliquots of supernatant containing selected viral populations and isolates using NucleoSpin 96 Virus Core Kit (Macherey-Nagel). The purified RNA was subjected to reverse transcription using SuperScript VILO cDNA Synthesis Kit (Thermo Fisher Scientific). The cDNA was amplified using KOD Xtreme Hot Start DNA Polymerase (Millipore Sigma) and primers flanking the entire S-encoding sequence. The PCR products were purified and sequenced using Sanger-sequencing.

To measure neutralizing activity, 40 μg/ml mAb was five-fold serially diluted in 96-well plates over 7 dilutions. Thereafter, approximately 5 × 10^4 infectious units of rVSV/SARS-CoV-2/GFP WT or mutant isolates were mixed with BG10-19 at a 1:1 ratio and incubated for 1 hr at 37°C in a 96-well plate. The mixture was then added to 293T/ACE2.cl22 target cells plated at 1 × 104 cells/well in 100 μl medium in 96-well plates the previous day. Thus, the final starting dilution was10 μg/ml. Cells were then cultured for 16 h, then harvested for flow cytometry.

QUANTIFICATION AND STATISTICAL ANALYSIS

scRNA-seq analysis

mRNA and VDJ sequence reads were mapped to the reference human genome GRCh38-3.0.0 with the cloud-based Cumulus workflows (Li et al., 2020), using the CellRanger 3.0.2 software pipeline. Cells with both high-quality VDJ sequence and transcriptome information were kept for the downstream analysis by filtering out the cells which had less than 300 detected genes or which had poor quality VDJ contig information defined by i) being non-productive by 10x standards, ii) having more than four productive VDJ contigs, iii) having less than three filtered UMIs. For the transcriptome analysis, batch effects were removed with the ComBat algorithm (Johnson et al., 2007) implemented in SVA R Package version 3.38.0.. For the transcriptome mRNA count normalization, dimensionality reduction, clustering, cell cycle scoring, cluster marker genes detection and differential gene expression analysis steps Seurat R package (Butler et al., 2018; Stuart et al., 2019) was employed. For the normalization step gene expression counts for each cell were divided by the total counts for that cell and multiplied by 1e6, which was then log-transformed using log1p. Dimensionality reduction was done by PCA with selecting 50 first principal components.

For clustering of the cells into transcriptome clusters, first the k-nearest neighbor (kNN) graph of the cells was constructed. Second, this kNN graph was used to generate the shared nearest neighbor (sNN) graph by calculating Jaccard index between every cell and its k nearest neighbors. Third, the leiden algorithm (Traag et al., 2019) was used to find the clusters of the cells based on the generated sNN graph.

Cell cycle scoring was done by calculating the module scores of the cell cycle genes defined in Tirosh et al. (2016). Positive cluster marker genes and differentially expressed genes were detected with a log-fold change threshold of 0.25, where only the genes that were detected in a minimum fraction of 20% in either of the six transcriptome populations were considered. Expression levels of Ig genes were discarded during the clustering and differential gene expression analysis steps. Source codes for scRNA-seq analyses were deposited in Github (https://github.com/EraslanBas/Sars_Cov2_Antibodies).

Ab Repertoire Analysis

10x V(D)J contig assembly algorithm takes many forms of noise specific to scRNA-seq data into account while generating the assembled V(D)J sequences (https://support.10xgenomics.com/single-cell-vdj/software/pipelines/latest/algorithms/assembly). Nevertheless, only the cells with high-quality V(D)J contig sequences were selected and V(D)J gene annotations were assigned by using IGBLAST (version 1.14.0) software with the Change-O R package (Gupta et al., 2015). Donor specific B cell clones were identified by the Change-O R package (Gupta et al., 2015), where the appropriate threshold for trimming the hierarchical clustering into B cell clones was found by inspecting the bimodal distribution of the distance between each sequence in the data and its nearest-neighbor.

Mutation inference based on the scRNA-seq VDJ sequences of the donor and the control cells (Rubelt et al., 2012) was performed by the Shazam R Package (Yaari et al., 2012) where the region definition parameter was set to be "IMGT_V_BY_SEGMENTS" which provides no subdivisons and treats the entire V segment as a single region.

CDRH3 length was defined based on IMGT definition (Lefranc et al., 2015) with the addition of two conserved amino acid residues that were added to assist in clonal analysis (Nouri and Kleinstein, 2018). This addition was corrected for all analyses involving specific CDRH3 length, such as selection of *VH3-53/3-66* mAbs with CDRH3 shorter than 14 amino acid length.

CDRH3 amino acid charges were calculated by the Alakazam R package (Gupta et al., 2015) using the method of Moore (Moore, 1985) excluding the N terminus and C terminus charges, and normalizing by the number of informative positions. Hydrophobicity scores were calculated with the Alakazam R package using the method of Kyte and Doolittle (Kyte and Doolittle, 1982).

Shannon entropy values were calculated using Alakazam R package. For each donor the transcriptome cluster specific Hill diversity index, proposed in (Hill, 1973), improved by (Chao et al., 2014, 2015) was calculated by setting the diversity order equal to 1 with Alakazam R package. For each run the number of bootstrap realizations is set to be 400, and the minimum number of observations to sample is set to be 10. Source codes for Ab repertoire analyses were deposited in Github (https://github.com/EraslanBas/Sars_Cov2_Antibodies).

Mutational analysis of VH3-53/3-66 mAbs

Inferred somatic mutations in the V gene segment of *VH3-53/VH3-66* mAbs were counted for the IgG$^+$ mAbs with CDRH3 lengths less than 14 amino acids from SARS-CoV-2 binding B cells across 14 subjects, listing only those sites where the frequency was > 10% in either the IgG$^+$ set or in the repertoire comparison. The repertoire comparison set of human *VH3-53/VH3-66* sequences was taken from the sequence read archive of Rubelt et al. (2012) and alignments were performed using MAFFT software (Katoh et al., 2019).
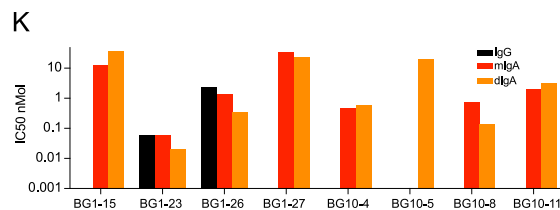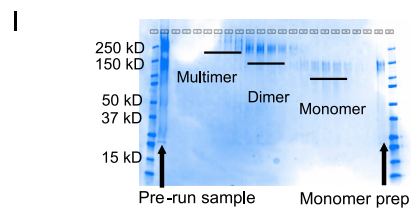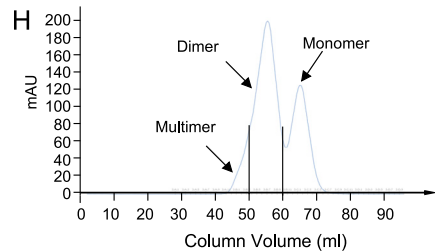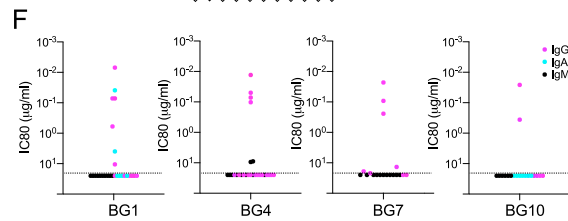
Supplemental figures

(legend on next page)
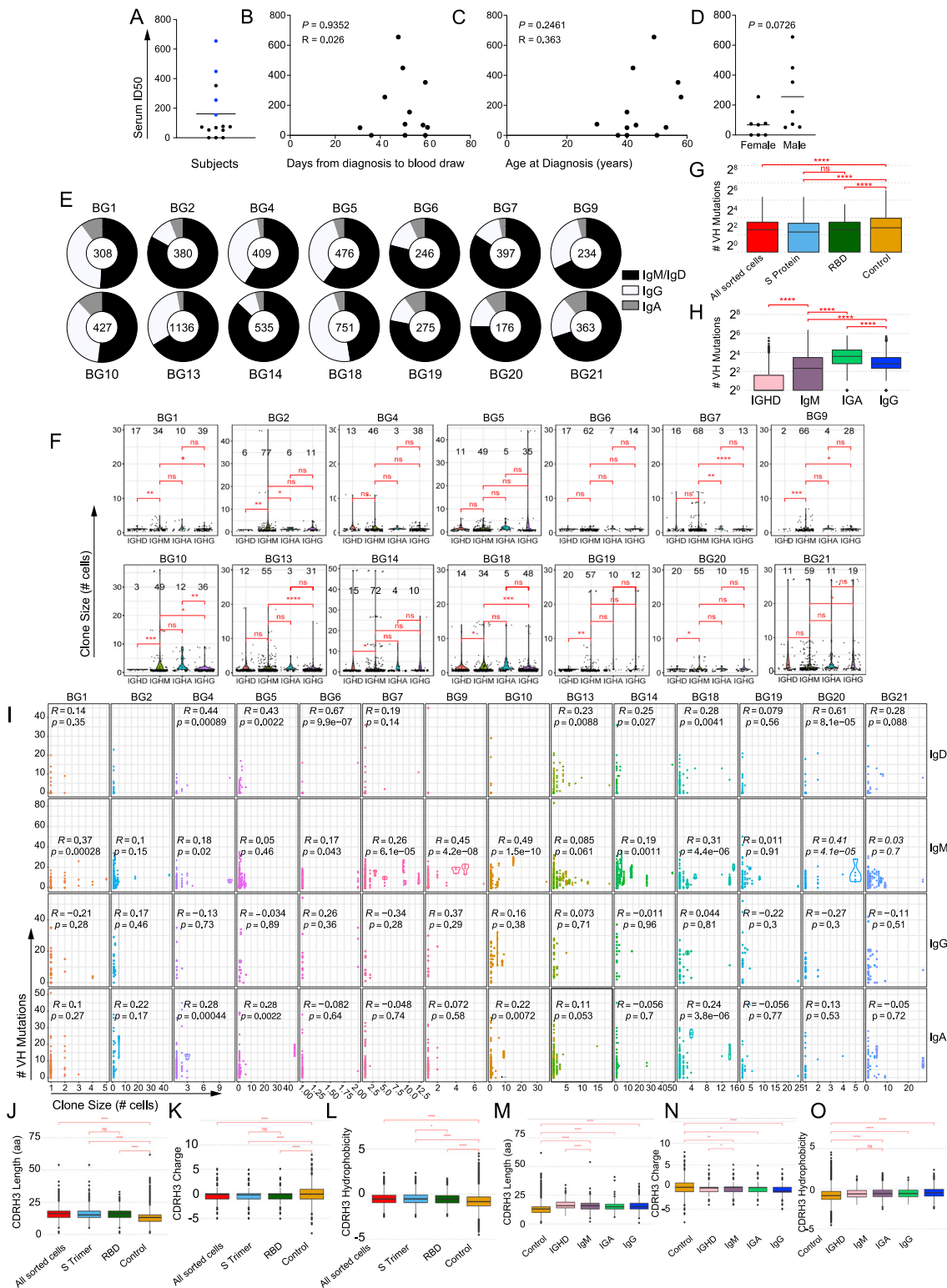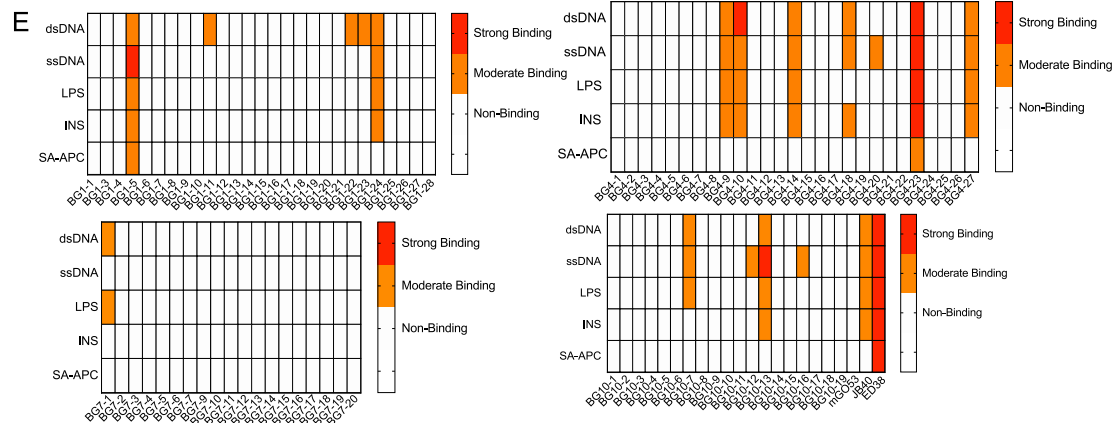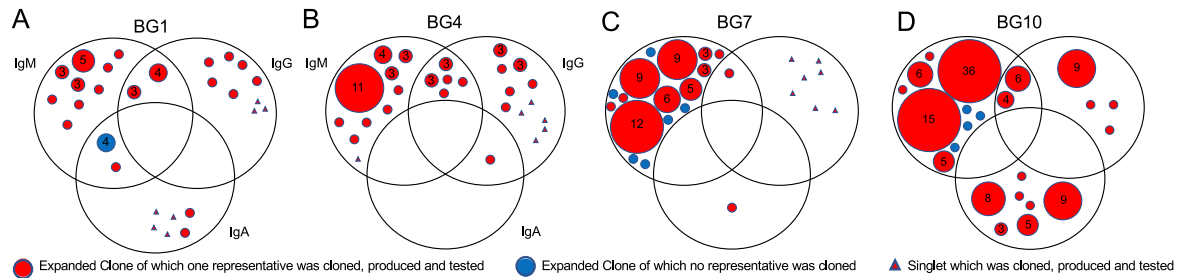
Figure S1. Serum neutralization against SARS-CoV-2 pseudovirus and B cell repertoire characteristics, related to Figure 1

(A) Serum ID_{50} titers of all 14 study subjects against SARS-CoV-2 pseudovirus. The blue dots represent subjects that were selected for mAb isolation. (B) Correlation between ID_{50} titers of all 14 study subjects against SARS-CoV-2 pseudovirus and days between COVID-19 diagnosis and blood draw. P value was calculated based on the Pearson correlation coefficient (R). (C) Correlation between ID_{50} titers of all 14 study subjects against SARS-CoV-2 pseudovirus and age of the subjects in years. P value was calculated based on the Pearson correlation coefficient (R). (D) Serum ID_{50} titers of all 14 study subjects against SARS-CoV-2 pseudovirus grouped based on subject gender. P value was calculated using an unpaired two-tailed t test. (E) Pie charts show the total number of B cells sorted from each subject in the center of each pie and differentially expanded pie slices represent the fraction of IgM/IgD$^+$ (black), IgG$^+$ (white) and IgA$^+$ (gray) cells among all sorted cells. (F) Distribution of clone sizes for each donor stratified by the clone isotype. Clones that contain cells from multiple isotypes are included as a data point in each of the respective groups. Numbers at the top of the violin plots display the percentage of cells from each isotype. Red brackets indicate statistical significance of the difference between isotypes with *p $\leq$ 0.05, **p $\leq$ 0.01, ***p $\leq$ 0.001, ****p $\leq$ 0.0001 and n/s indicating no statistical significance. P values were calculated using a two-tailed t test. (G) Boxplots showing absolute numbers of inferred nucleotide mutations per heavy chain V segment for all sorted cells (red bar), S-binding B cells (blue bar), RBD-binding B cells (green bar) and historic control MBCs (brown bar) (Rubelt et al., 2012). The box limits are at the lower and upper quartiles and the center line indicates the median. (H) Boxplots showing absolute numbers of inferred nucleotide mutations per heavy chain V segment for all sorted cells grouped by Ig isotypes IgD (pink), IgM (purple), IgA (green) and IgG (blue). The box limits are at the lower and upper quartiles, the center line indicates the median, the whiskers indicate 1.5x interquartile range and the dots represent outliers. P values were calculated using two tailed t test and red brackets indicate statistical significance of the difference between samples with stars indicating P values as in (F). (I) Scatterplot displaying the relationship between clone size (number of cells, x axis) and number of inferred mutations in the heavy chain V segment (y axis). Each dot represents a cell or a group of cells within a clone with the same heavy chain isotype and number of inferred heavy chain mutations. Clonally related cells with different number of inferred heavy chain mutations are shown with the same color and grouped with violin plots. Pearson correlation coefficients and the P values of each sub-plot are shown on separately. (J) Boxplots showing the CDRH3 length in amino acids for all sorted cells (red), S-binding B cells (blue), RBD-binding B cells (green), historic control MBCs (brown) (Rubelt et al., 2012). (K) Boxplots showing the CDRH3 amino acid charges for all sorted cells (red), S-binding B cells (blue), RBD-binding B cells (green), historic control MBCs (brown) (Rubelt et al., 2012). (L) Boxplots showing the CDRH3 amino acid hydrophobicity scores for all sorted cells (red), S-binding B cells (blue), RBD-binding B cells (green), historic control MBCs (brown) (Rubelt et al., 2012). (M) Boxplots showing the CDRH3 length in amino acids for historic control MBCs (brown) (Rubelt et al., 2012), IgD$^+$ SARS-CoV2-binding B cells (pink), IgM$^+$ SARS-CoV-2-binding B cells (purple), IgA$^+$ SARS-CoV-2-binding B cells (green), IgG$^+$ SARS-CoV-2-binding B cells (blue). (N) Boxplots showing the CDRH3 amino acid charges for historic control MBCs (brown) (Rubelt et al., 2012), IgD$^+$ SARS-CoV-2-binding B cells (pink), IgM$^+$ SARS-CoV-2-binding B cells (purple), IgA$^+$ SARS-CoV-2-binding B cells (green), IgG$^+$ SARS-CoV-2-binding B cells (blue). CDRH3 amino acid charges were calculated as in (K). (O) Boxplots showing the CDRH3 amino acid hydrophobicity scores for historic control MBCs (brown) (Rubelt et al., 2012), IgD$^+$ SARS-CoV-2-binding B cells (pink), IgM$^+$ SARS-CoV-2-binding B cells (purple), IgA$^+$ SARS-CoV-2-binding B cells (green), IgG$^+$ SARS-CoV-2-binding B cells (blue). Hydrophobicity scores were calculated as in (L). For all boxplots the box limits are at the lower and upper quartiles, the center line indicates the median, the whiskers indicate 1.5x interquartile range and the dots represent outliers. P values were calculated using two tailed t test and red brackets indicate statistical significance of the difference between samples with stars indicating P values as in (F).

● Expanded Clone of which one representative was cloned, produced and tested   ● Expanded Clone of which no representative was cloned   ▲ Singlet which was cloned, produced and tested
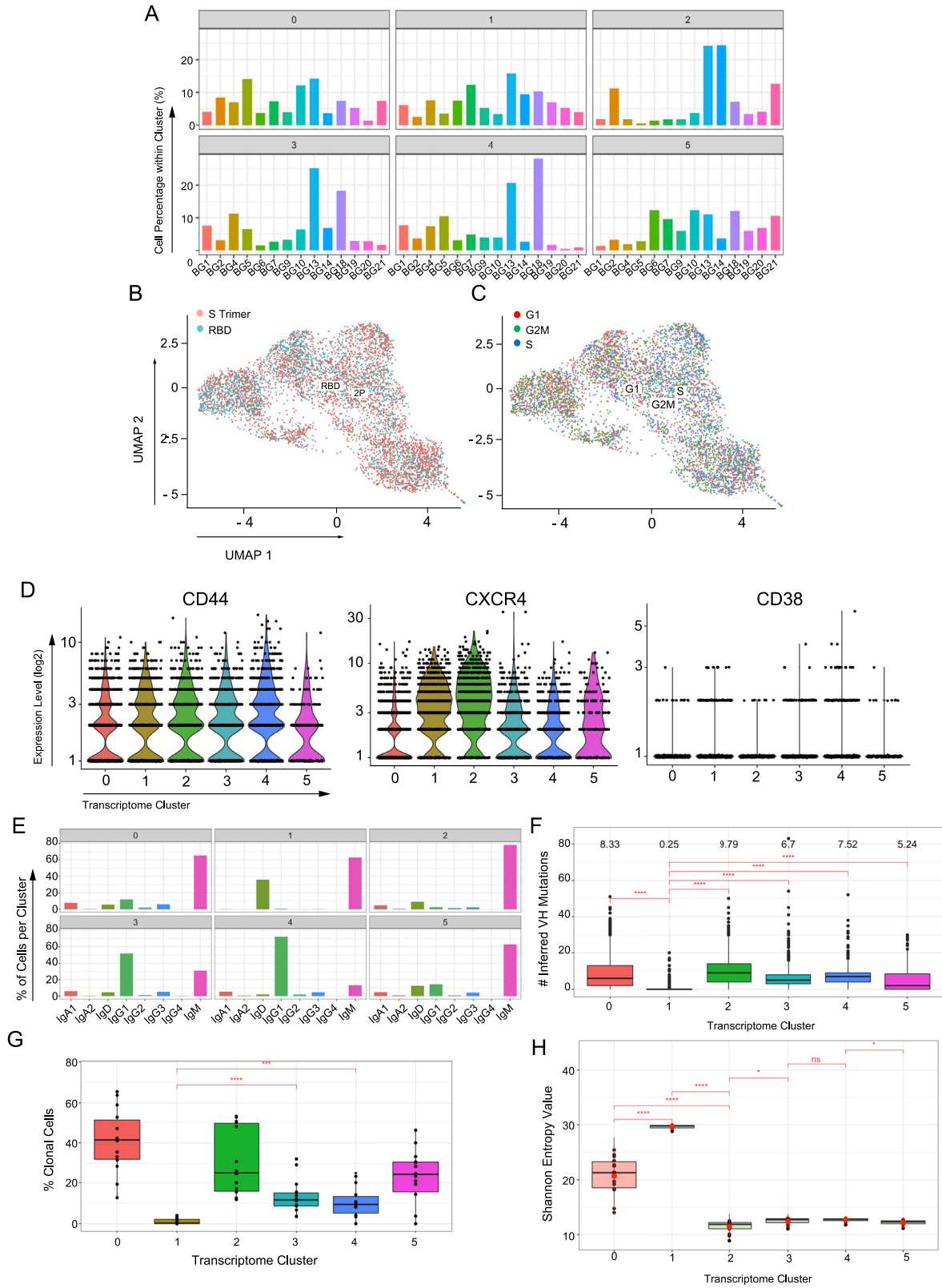
(legend on next page)

Figure S2. Selection and testing of representative mAbs, related to Figure 2

Venn diagrams summarizing all expanded clones, their Ig isotypes and selection of representative mAbs for donors BG1 (A), BG4 (B), BG7 (C) and BG10 (D). Colored circles show expanded B cell clones with the diameter of the circle corresponding to the size of the clone except for the largest clone in BG10 with 36 members. The numbers in the circles indicate the number of clonal members for all clones with more than 2 members respectively. Red circles show expanded clones of which one representative mAb was produced and tested and blue circles show all expanded clones of which no representative mAbs were tested. Red triangles represent singlets that were produced and tested. (E) Heatmap summarizing the polyreactivity ELISA results for all mAbs produced as IgG1 isolated from BG1, BG4, BG7 and BG10 against double strand DNA (dsDNA), single strand DNA (ssDNA), lipopolysaccharide (LPS), insulin (Ins) and streptavidin-APC (SA-APC) (STAR Methods). OD^{415} values less than 0.5 at a mAb concentration of 1μg/ml are considered non-reactive and are indicated in white, OD^{415} values between 0.5 and 1.9 are considered moderately reactive and are indicated in orange, and OD^{415} values of 2 and above are considered strongly reactive and are indicated in red (Tiller et al., 2007). Results for highly-, moderately- and non-polyreactive control mAbs ED38, JB40 and mGO53 are included as indicated (Wardemann et al., 2003). (F) Dot plots summarizing IC_{80} values from SARS-CoV-2 pseudovirus neutralization assay in μg/ml (y axis) for all mAbs isolated from subjects BG1, BG4, BG7 and BG10 and produced as IgG1 (Table S2). Pink dots represent mAbs isolated from IgG^+ B cells, bright blue dots represent mAbs isolated from IgA^+ B cells and black dots show mAbs isolated from IgM^+ B cells. Data points beneath the dotted lines represent antibodies that did not reach an IC_{80} at concentrations up to 25 μg/ml (Table S2). (G) Table summarizing neutralizing activity of mAbs BG10-19, BG1-22, BG4-25 and BG7-15 against SARS-CoV-2 D614G, B.1.1.7 and B.1.351. Shown are IC_{50} and IC_{80} values in μg/ml as indicated. (H) Representative image from size exclusion chromatography for purification of IgA dimers for mAb BG1-20 (Table S2). y axis displays absorption at 280 nm (mAU) and x axis displays elution volume (in ml). (I) Representative $Criterion^{TM}$ TGX^{TM} precast gel under non-reducing conditions after Coomassie Blue staining. Ladders with bands at indicated molecular weights are shown on the left and right end of the gel and adjacent to these are the pre-SEC sample and a monomeric IgA as indicated. The 22 lanes in the middle show consecutive elution fractions from SEC covering the multimer, dimer and monomer peaks as indicated and seen in (H). (J) Summary table for IgA neutralization of SARS-CoV-2 pseudovirus. Shown are the IC_{50} and IC_{80} values in μg/ml (left two columns) followed by IC_{50} and IC_{80} values in nmol and IC_{50} and IC_{80} values in nmol corrected for the number of binding sites (Corr) and the molar neutralization ratios (MNR) as defined by the IC_{50} or IC_{80} of monomeric IgA divided by the IC_{50} or IC_{80} for the dimeric version respectively (Klein and Bjorkman, 2010). G = IgG1, mA = monomeric IgA, dA = dimeric IgA. (K) Bar graph summarizing the data from (J). Shown are all IgA mAbs which showed some level of neutralization in SARS-CoV-2 pseudovirus neutralization assay in monomeric or dimeric form. y axis depicts IC_{50} (in nmol) corrected for the number of binding sites, x axis indicates the different mAbs as indicated. Black bars show neutralization in IgG1 form (IgG), red bars in monomeric IgA (mIgA) and orange bars in dimeric IgA (dIgA) form.
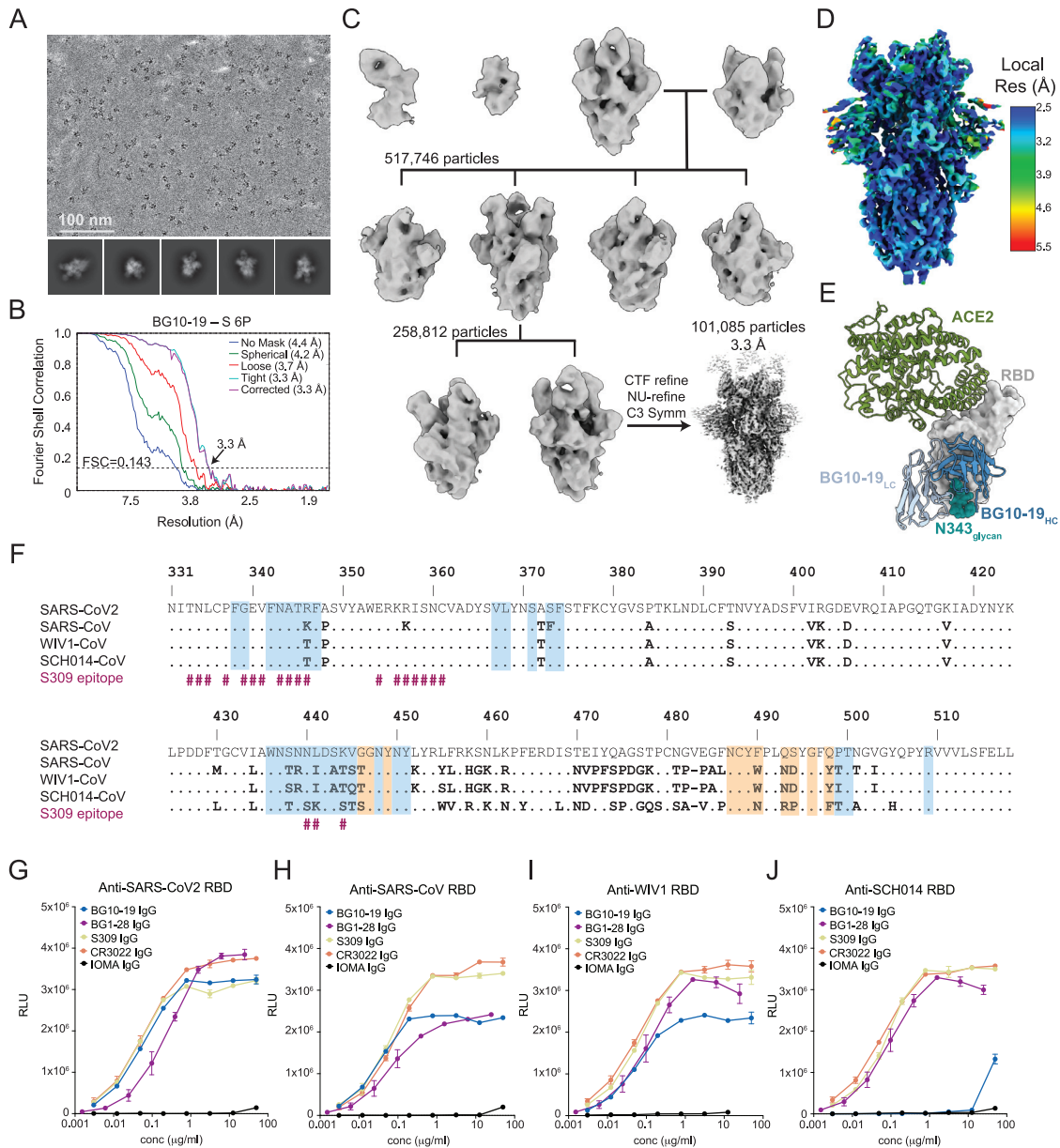
Figure S3. BG10-19 cryo-EM validation, epitope mapping, and cross-reactive ELISA binding data, related to Figure 3

(A) Representative micrograph and 2D class averages for BG10-19 – S cryo-EM data collection. (B) Gold-standard FSC plot showing an overall resolution of 3.3 Å at FSC = 0.143. (C) Initial *ab initio* model generation (k = 4) and subsequent 3D classification for BG10-19 – S 6P cryo-EM data. Despite the ability of S 6P trimers to adopt 'up' RBD conformations, 3D classification steps revealed no populations of 'up' RBD conformations. (D) Local resolution estimation for the final cryo-EM reconstruction. (E) Overlay of BG10-19 (blue) and hACE2 (green, PDB 6M0J) on the RBD (gray surface). (F) Sequence alignment of SARS-CoV-2, SARS-CoV, WIV1-CoV, and SCH014-COV using CustalOmega (Sievers et al., 2011). RBD residues on the primary BG10-19 epitope are shaded blue. Residues contacted on the adjacent RBD are shaded orange. S309 epitope residues are also shown. (G-J) ELISA binding data for BG10-19, BG1-28, S309 (Pinto et al., 2020), CR3022 (Tian et al., 2020), and the HIV-1 mAb IOMA (Gristick et al., 2016) against several sarbecoviruses.

Figure S4. Transcriptional characteristics, related to Figure 4

(A) Bar diagram showing the percentage of cells from individual donors contributing to all cells within each cluster as indicated. (B) Uniform Manifold Approximation and Projection (UMAP) plot displaying the cells defined by their single-cell transcriptome measurements. The cells are colored based on whether they were isolated with SARS-CoV-2 S trimer (red) or RBD (turquoise) during cell sorting. (C) Same UMAP as in (B), but cells are colored based on their cell cycle phase G1 (red), G2M (green) or S (blue) as predicted by the Seurat cell cycle scoring function (Butler et al., 2018; Stuart et al., 2019). (D) Violin plots displaying the distribution of the expression levels of CD44, CXCR4 and CD38 (log2) within each single-cell transcriptome cluster. (E) Bar plot displaying the percentage of each Ig isotype within each transcriptome cluster. (F) Boxplots displaying the distribution of the number of inferred mutations in the Ig heavy chains within each of the 6 transcriptome clusters. Mean values are displayed above each box. Significance of the difference between the mean values of each cluster with the mean of cluster 1 was calculated using one-tailed t test. (G) Boxplots displaying the distribution of the percentage of donor clonal cells within each transcriptome cluster (i.e., fraction of cells that are part of a B cell clone with 2 or more members across the entire donor). Significance of the difference between the mean values of clusters 3 and 4 with the mean of cluster 1 was calculated with one-tailed t test. (H) Shannon entropy values calculated based on the general form of the diversity index proposed by Hill (1973), improved by resampling strategies in Chao et al. (2014, 2015) and implemented in the Alakazam R package (Gupta et al., 2015). Each dot represents the Shannon entropy value of a specific donor among the 14 donors in the specified cluster. Shannon entropy values are reversely related with the clonal expansion within the clusters. Thus, according to the displayed comparisons TC1 contains the smallest clonal expansion. Significance values of pairwise comparisons are computed with two-tailed t test. For (F), (G) and (H) red brackets indicate statistical significance of the difference between samples. *p $\leq$ 0.05, ***p $\leq$ 0.001, ****p $\leq$ 0.0001 and n/s indicates no statistical significance.
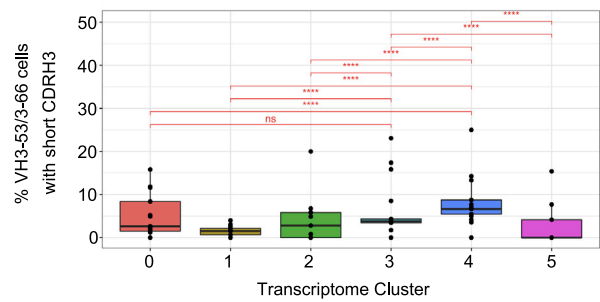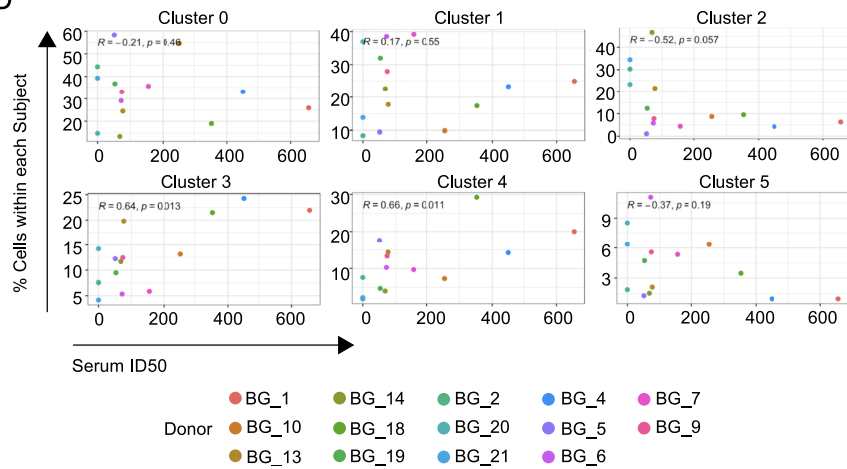
A
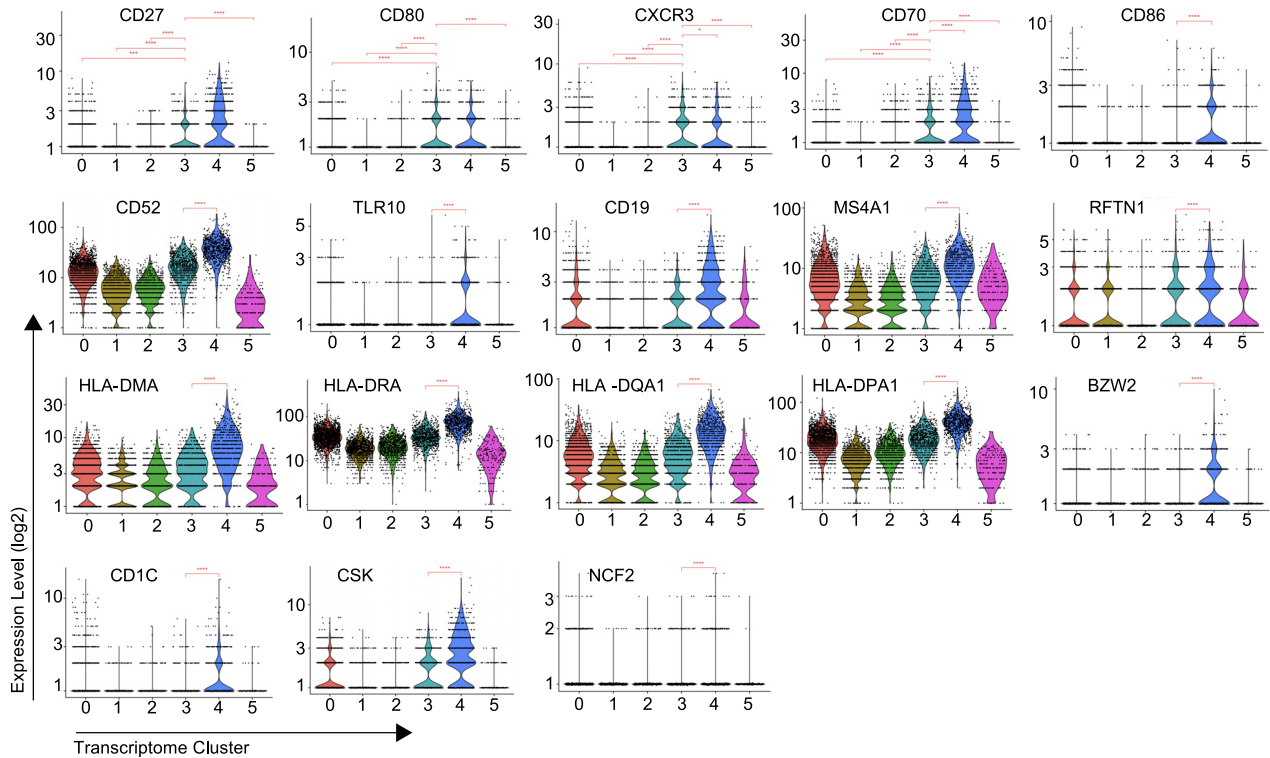
B
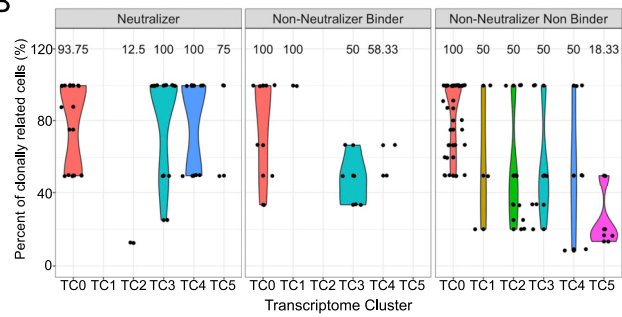
C

D

Figure S5. TC3 and TC4 characterization, related to Figure 4

(A) Violin plots displaying the distribution of the expression levels of various genes across single-cell transcriptome clusters. The significance of the mean value comparisons between different clusters was calculated using a two-tailed t test. (B) Distribution of the percent of B cell clones across 6 transcriptome clusters, stratified by neutralizing activity of the tested mAb. Each dot displays the percentage of cells from a specific clone (y axis) that belongs to the specified transcriptome cluster (x axis). Numbers on top of each violin plot show the median value of the distribution. (C) Boxplots displaying the percentage of *VH3-53* or *VH3-66* cells (with CDRH3 length shorter than 14 aa by IMGT definition) (Lefranc et al., 2015) of the 14 donors within each transcriptome cluster. Mean values of cluster 3 and 4 were compared with the mean values of other clusters using a two-tailed t test. For (A) and (C) red brackets indicate statistical significance of the difference between samples. *p $\leq$ 0.05, ***p $\leq$ 0.001, ****p $\leq$ 0.0001, and n/s indicates no statistical significance. (D) Scatterplots displaying the relationship between the percent of cells within each donor coming from TC0-5 with the serum neutralization titers for each donor. Spearman correlation values with corresponding *P* values are shown on each subplot. Dots are colored based on the donor ID, as indicated.
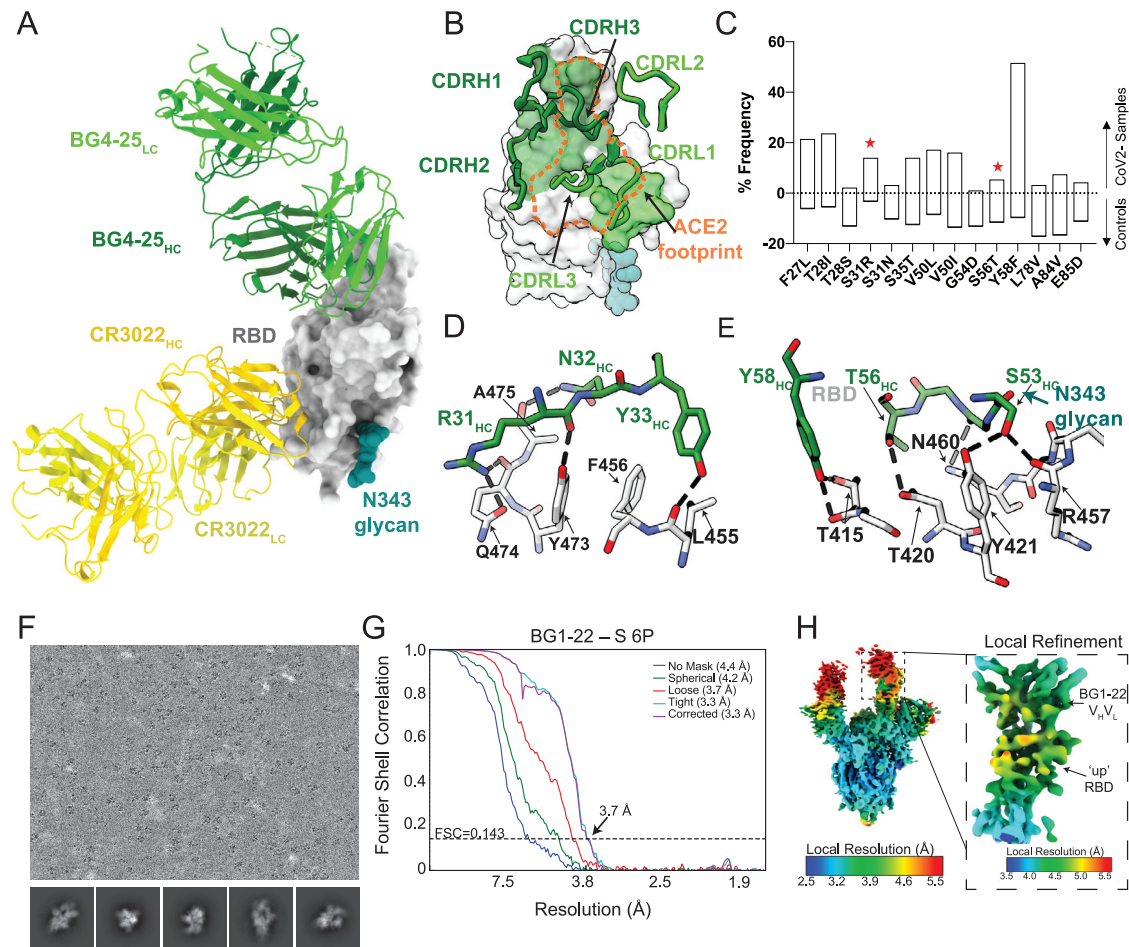
Figure S6. BG4-25 RBD structure and BG1-22 S trimer cryo-EM validation, related to Figure 5

(A) X-ray structure overview of BG4-25 (green) in complex with the SARS-CoV-2 RBD (gray surface) and mAb CR3022 (yellow) (Tian et al., 2020). (B) BG4-25 CDR loops mapped on the surface of the RBD. Epitope residues are colored green and the ACE2 footprint shown (orange dotted line). (C) Bar diagram showing the mutation frequency of all inferred mutations that occurred in 10% or more of 93 isolated IgG+ *VH3-53/VH3-66* mAbs with CDRH3 less than 14 amino acids (IMGT definition) (Lefranc et al., 2015) from our collection of 6,113 SARS-CoV-2 binding B cells and a reference group of 13,900 VH3-53/VH3-66 sequences from a human Ig gene repertoire set (STAR Methods) (Rubelt et al., 2012). The frequencies of mutations in the mAbs from the SARS-CoV-2 binding B cells are shown above the dotted line and the frequencies of mutations in the reference group are shown below the dotted line. (D, E) Residue level contacts between BG4-25 (green) and RBD (light gray). Potential H-bonds are shown as dashed lines. (F) Representative micrograph and 2D class averages for BG1-22 – S cryo-EM data collection. (G) Gold-standard FSC plot showing an overall resolution of 3.7 Å at FSC = 0.143. (H) Local resolution estimation for the final cryo-EM reconstruction (left) and cryo-EM density generated after local refinement at the BG1-22 – RBD interface (right; box).
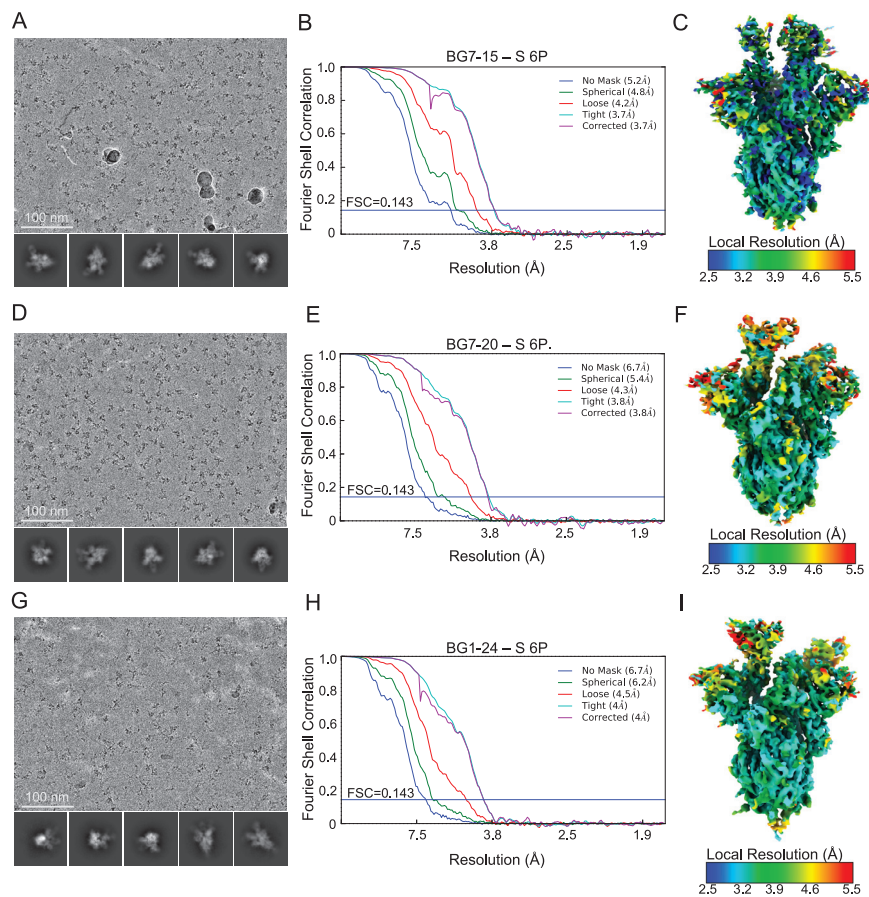
Figure S7. Cryo-EM validation of BG7-15, BG7-20, and BG1-24 S trimer complexes, related to Figure 6

Representative micrograph (scale bar = 100 nm) selected from total dataset, 2D class averages, gold-standard FSC plots, and local resolution estimations for (A-C) BG7-15 – S complex, (D-F) BG7-20 – S complex, and (G-I) BG1-24 – S complex.